

Development of CeO₂ based High Performance MEMS Oxygen Gas Sensor

Thesis

Submitted in partial fulfillment of the requirements for the degree of
DOCTOR OF PHILOSOPHY

by

Ramshanker N.

Under the Guidance of

Dr. S. Mohan

Professor Emeritus

Centre for Nano Science and Engineering

IISc, Bengaluru- 560012

Dr. M. S. Bhat

Professor

Dept. of E&C Engineering

NITK Surathkal-575025

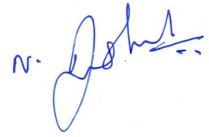


DEPARTMENT OF ELECTRONICS AND COMMUNICATION ENGINEERING,
NATIONAL INSTITUTE OF TECHNOLOGY KARNATAKA,
SURATHKAL, MANGALORE - 575025

November, 2020

DECLARATION

I hereby *declare* that the Research Thesis entitled **Development of CeO₂ based High Performance MEMS Oxygen Gas Sensor** which is being submitted to the *National Institute of Technology Karnataka, Surathkal* in partial fulfillment of the requirement for the award of the Degree of *Doctor of Philosophy* in **Department of Electronics and Communication Engineering** is a *bonafide report of the research work carried out by me*. The material contained in this Research Thesis has not been submitted to any University or Institution for the award of any degree.



RAMSHANKER N.

Reg. No. 135049EC13P01

Department of Electronics and Communication Engineering.

Place: NITK, Surathkal.

Date: 12-3-2021

CERTIFICATE

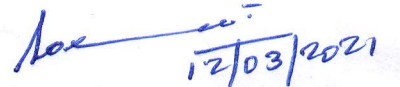
This is to certify that the Research Thesis entitled **Development of CeO₂ based High Performance MEMS Oxygen Gas Sensor** submitted by **Ramshanker N** (Register Number: 135049EC13P01) as the record of the research work carried out by him, is accepted as the *Research Thesis submission* in partial fulfillment of the requirements for the award of degree of **Doctor of Philosophy**.



Dr. M.S. Bhat
Research Supervisor
Professor
Dept. of Electronics and Communication Engineering.
NITK, Surathkal



Dr. S. Mohan
Professor Emeritus
Centre for Nano Science and Engineering
IISc, Bengaluru - 560012



Chairman-DRPC

(Signature with Date and Seal)

प्राध्यापक एवं विभागाध्यक्ष / PROF & HEAD
ई एवं सी विभाग / E & C Department
एन आई टी के, सुरतकल/NITK, Surathkal
मंगलूर / MANGALORE - 575 025

All our dreams can come true, if we have the courage to pursue them

*Dedicated to my
Teachers, Family and Friends*

Acknowledgements

I take this opportunity to express my sincere words of gratitude to National Institute of Technology Karnataka (NITK), Surathkal for providing me an opportunity to carry out my research work at this premier research institution.

I would like to express the deepest appreciation to my mentors and supervisors, **Dr. S. Mohan**, Emeritus Professor, CeNSE, IISc, Bangalore and **Dr. M. S. Bhat**, Professor, Department Electronics and Communication (E&C) Engineering, NITK. With their enthusiasm, inspiration, patience, and great ability to explain things clearly and simply, they transformed the researcher and the person in me. Throughout my research, they provided encouragement, sound advice, good teaching, good company, and lots of good ideas. They continually and convincingly conveyed a spirit of adventure in regard to this work, and an excitement in regard to teaching. I too have learnt a lot from their qualities like excellent management skills, presentation etc. I feel very fortunate enough and privileged to have gotten trained by these legends.

I deliver my sincere thanks to **Dr. Rudra Pratap**, Former Chairperson and Professor, Centre for Nano Science and Engineering (CeNSE), Indian Institute of Science (IISc), Bangalore and **Dr. Navakanta Bhat**, Professor and Chairperson, CeNSE, IISc for permitting and providing me with necessary facilities to carry out this work.

I owe a deep sense of gratitude to **Dr. Kolla Lakshmi Ganapathi**, DST INSPIRE Faculty, Department of Physics, Indian Institute of Technology-Madras (IIT-M) who showered the light to my research work. His immense knowledge, insightful comments and constant encouragement has led to widen my research perspectives and also to complete this work. Without his direction and persistent help this thesis would have not been possible. It has been a great honour to work under his supervision.

I sincerely thank **Dr. G. Umesh**, Professor, Department of Physics and Dean (Research and Consultancy), NITK, without his help, I would not have come to NITK.

I extend my thanks to all the teaching and non-teaching members for their support throughout the course work of my Research.

Besides my advisors, I would like to thank the rest of my RPAC committee: **Dr. T. Laxminidhi**, Professor and Head, Department of E&C Engineering, NITK. Both **Dr. S M Kulkarni**, Professor, Department of Mechanical Engg, NITK and **Dr. Muralidhar Kulkarni**, Professor and Former Head, Department of E&C Engineering, NITK, Surathkal for their valuable and timely advice, motivation and moral support during this research.

I had a wonderful time with my batch mates in NITK and thank them sincerely. It is difficult to put names of all people in acknowledgement because this list is very big but I am thankful to everybody sincerely for their support and love.

I now make a futile attempt to thank my mother, father and friends for their encouragement and support. They have been the very essence of my existence.

Finally, my sincere thanks to Kavitha, my wife and Mukundaa, my son, who are the whole source for my inspiration and they have sacrificed a lot for my convenience and supported me all time. They never tried to become hurdle in my studies, rather inspired me to lead final goal with their love and encouragement. I can only thank them by giving an honorary doctorate from my side.

Last but not the least, I thank my goddess of wisdom for always being there in my beliefs.

Abstract

A gas sensor is a device that is used to measure the concentration of gas in its vicinity. It can also be used as a leak detector to detect a gas leak or other emissions. Extensive research is being carried out on gas sensor in designing miniaturized and cost effective sensors that possess the required characteristics of high sensitivity, selectivity and stability with respect to a specific application. Fast and unambiguous analysis of human surroundings will be in the near future inseparable part of public health, security and life quality control. Semiconductor metal oxide gas sensors stand out among the other types of sensors because of their simplicity and low cost.

In the present work, we developed scalable, high sensitivity, fast response and low operating temperature CeO₂ thin film based oxygen sensors. A systematic investigation has been carried out to develop the high performance oxygen sensor which includes the optimization and integration of sensor film and micro-heaters.

CeO₂ thin films of different thicknesses ranging from 90 nm to 340 nm have been deposited at 400°C using RF magnetron sputtering on Al₂O₃ substrates. Characterization techniques such as Ellipsometry, XRD, XPS and AFM have been used to characterize the CeO₂ films for their thickness, structural, compositional/chemical and surface morphological properties. From XRD and XPS data, it has been observed that all the films are polycrystalline and with thickness more than 195 nm are stoichiometric. It has also been observed that the resistivity of the films depends on the texture coefficient of (200) plane of CeO₂. It has been found that 260 nm thick film has high textured coefficient of (200) plane which shows minimum electrical resistivity and maximum sensitivity towards the oxygen gas. The CeO₂ film with an optimum thickness of 260 nm has shown very high sensitivity (12.6), fast response time (≤ 10 s) and recovery time (15 s) at a low operating temperature of 400°C, which are the best values reported till date in case of undoped CeO₂ thin film based sensors. The response time of CeO₂ based sensor may be reduced further by increasing the conductivity of the CeO₂ films with appropriate dopants.

A novel technique was used for the synthesis of CeO₂-HfO₂ mixed oxide thin films using RF sputtering. The mixed oxide films showed better sensing performance in comparison with pure CeO₂ films. The Hf atomic concentration was controlled varying the size and number of HfO₂ pellets to achieve the best sensing performance. The CeO₂-HfO₂ mixed oxide sensor with 10-11% of Hf concentration showed best sensitivity (~ 15), response time (8 s) and recovery time (10 s) at a low operating temperature of $<400^\circ\text{C}$ reported till date. From XRD and XPS data, it was understood and concluded that the best sensing characteristics of CeO₂-HfO₂ mixed oxide film with 10-11% atomic concentration of Hf can be attributed to the existence of a highly reactive plane (200) with the highest surface energy and a strongly reduced surface with oxygen vacancy formation due to the presence of Ce³⁺ ions and HfO_x, $x < 2$ on the surface of the mixed oxide film. The sensor performance is reproducible without any drift in the base line resistance.

Microheaters play a crucial in MEMS gas sensor technology. Several microheater designs have been studied, however new heater patterns and designs are required to achieve excellent temperature uniformity and low power consumption. Here in this work, the area of the heater is optimized in order to increase the resistance by adopting novel designs / geometries. The single meander shape was taken as a reference design. After several modifications, iterations and optimizations, two different geometrical structures namely Perforated Type 1 and Type 2 Platinum microheaters of dimension $500\mu\text{m} \times 500\mu\text{m}$ were designed and analyzed using FEM based software COMSOL. The simulated results show the temperature being distributed uniformly across the entire structure in both the designs. The designed microheaters were fabricated and characterized thermally and electrically and showed excellent temperature uniformity and the power consumed to obtain the temperature of 400°C is nearly between 1.14 to 1.44 W which is considerably lower than reported values in the literature. The fabricated heaters were integrated into a gas sensor and the device was tested for oxygen gas. The sensing results were found to be in good agreement with the results obtained using a conventional heater.

Readout circuits are circuits used to convert the sensed signal, such as

voltage, current, resistance etc. or changes in it into a more convenient form of the same or different type of signal for further processing. A highly efficient 3-stage op-amp based readout circuit is designed to measure the dynamic change of the sensing film resistance. The three stages are namely : constant current source, buffer amplifier and feedback amplifier. The 3 amplifier configuration with a constant current source is used to measure the change in resistance and voltage is measured across the resistance under test. The real-time simulation results show that the circuit is highly efficient and linear.

Keywords: Gas Sensors, Oxygen Sensors, Cerium oxide RF sputtering, Thickness Optimization, Thin Film, High Sensitivity, Fast Response Time, Mixed Oxides, Microheaters, Readout circuit.

Contents

Dedication	i
Acknowledgements	iii
Abstract	v
List of figures	xii
List of tables	xvi
Abbreviations	xvii
1 Introduction to Gas Sensors	1
1.1 Metal oxide based Gas Sensors	2
1.1.1 Sensing Mechanism	5
1.1.2 Basic Characteristics of Semiconductor Gas Sensors	7
1.2 Need for Oxygen Sensor	8
1.2.1 Hazards from Oxygen Deficiency	10
1.3 Materials for Gas Sensors	10
1.4 Research Objectives	14
1.5 Thesis Organization	14
2 Literature Survey	16
2.1 Introduction	16
2.2 CeO ₂ film processing	17
2.2.1 Screen Printing	17
2.2.2 Precipitation and Co-Precipitation	18
2.2.3 Sol-gel synthesis	18
2.2.4 Spray Pyrolysis	19
2.2.5 Spin coating	20
2.2.6 Metal Organic Chemical Vapor Deposition (MOCVD)	20
2.2.7 Physical Vapor Deposition Techniques (PVD)	21

2.3	Works reported on development of oxygen sensor using CeO ₂ as sensing material	21
3	Experimental Details	26
3.1	Introduction	26
3.2	Overview of Deposition Techniques	26
3.3	Physical Vapor Deposition	27
3.3.1	Evaporation	27
3.3.2	Sputtering	29
3.3.2.1	Reactive RF Sputtering Principle:	30
3.3.2.2	RF Magnetron Sputtering	31
3.3.2.3	In house Developed RF Sputtering System	32
3.4	Fabrication of Sensor Film	34
3.4.1	Sample Preparation	34
3.4.2	Deposition of CeO ₂ films by RF Sputtering Technique	34
3.4.3	Deposition of Mixed Oxides (CeO ₂ -HfO ₂) films by RF Sputtering Technique	35
3.5	Characterization Techniques	36
3.5.1	Thickness measurement techniques	37
3.5.1.1	Spectroscopic Ellipsometry	37
3.5.1.2	Scanning Electron Microscopy (SEM)	39
3.5.1.3	Atomic Force Microscopy (AFM)	39
3.5.1.4	X-ray Diffraction (XRD)	41
3.5.1.5	X-ray Photoelectron Spectroscopy (XPS)	42
3.5.1.6	Electron Probe Micro Analyzer (EPMA)	45
3.6	Fabrication of Electrodes or Contacts	46
3.7	Gas Sensing Measurements	47
3.7.1	Thermal Characterization of Microheaters	48
4	RF Sputtered CeO₂ Thin Films Based Oxygen Sensors	50
4.1	Introduction	50
4.2	Sensor Fabrication	51
4.3	Results and Discussion	52
4.3.1	Physical properties	53
4.3.2	Compositional properties	54

4.3.3	Surface topography	57
4.3.4	Structural properties	58
4.3.5	Gas Sensing Characteristics	60
4.4	Conclusion	64
5	Process Optimization and Characterization of CeO₂–HfO₂ films deposited by RF Sputtering Technique	66
5.1	Introduction	66
5.2	Results and discussion	67
5.2.1	Thickness measurement	68
5.2.2	Gas sensing characteristics	69
5.2.3	Compositional results	70
5.2.4	Structural analysis	74
5.2.5	Optimized CeO ₂ –HfO ₂ mixed oxide thin film sensor performance	76
5.3	Conclusions	78
6	Design and Development of Microheaters with High Temperature Uniformity for Gas Sensors	80
6.1	Introduction	80
6.2	Design and Electro Thermal Modeling of Microheaters	81
6.2.1	Meshing in COMSOL	85
6.2.2	Simulation Results	86
6.3	Fabrication of Microheaters	87
6.4	Microheater Characterization	88
6.4.1	Thermal Images of the Microheater Patterns	90
6.4.2	Electrical Characterization of Microheaters	91
6.5	Integrated Gas Sensor (Microheater + Sensing Element)	93
6.6	Conclusion	95
7	Design of Wide Range Readout Circuit	97
7.1	Gas Sensor Readout circuit Design	97
7.1.1	Interface circuit requirements and state of art	97
7.1.2	Interface circuit requirements	98
7.1.3	State of art of interface circuits	99
7.1.3.1	Potential divider circuit	100

7.1.3.2	The Wheatstone Bridge	101
7.2	Developed Readout Circuit structure	103
8	Conclusions and Future Scope	105
8.1	Conclusions	105
8.2	Future Scope	106
	Bibliography	127
	Publications based on the thesis	128

List of Figures

1.1	Types of Gas Sensors Nazemi <i>et al.</i> (2019)	3
1.2	Comparison of different metal oxides used as sensing materials Eranna <i>et al.</i> (2004)	3
1.3	Schematic of Integrated metal oxide gas sensor Bruins <i>et al.</i> (2013) . .	5
1.4	Different operational modes of gas sensor Dey (2018)	6
1.5	Response-curve of a chemiresistive gas sensor Hassan (2017)	7
1.6	Atmospheric air composition	9
1.7	Relative comparison of different oxides used for gas-sensing application Eranna <i>et al.</i> (2004)	11
1.8	Comparison of gaseous species studied by using various metal oxides Eranna <i>et al.</i> (2004)	12
1.9	Cerium dioxide cubic fluorite structure Bumajdad <i>et al.</i> (2009)	13
3.1	Broad classification of film deposition methods	27
3.2	Sputtering at the Molecular Level Oxford Vacuum Science Ltd (2000) .	31
3.3	Schematic of magnetron sputtering principle Julissa (1994)	32
3.4	Schematic of the RF Sputtering Chamber Bashar (1998)	33
3.5	(a) Photograph of in-house fabricated RF sputtering unit. (b) Schematic of the sputtering chamber	33
3.6	Arrangement of HfO ₂ chips on the 3” Cerium Oxide target	36
3.7	Spectroscopic Ellipsometry measurements	38
3.8	Schematic diagram and picture of Ellipsometry equipment Woollam Spectroscopic Ellipsometer (M-2000)	39
3.9	ULTRA 55 - Ultra high resolution scanning electron imaging coupled with material spectroscopy tools	40
3.10	Bruker AFM instrument	40
3.11	Rigaku SmartLab High Resolution X-ray Diffractometer system.	42

3.12 Multi-technique X-ray Photoelectron Spectroscopy with XPS-mapping capability	44
3.13 Schematic of EPMA and Picture of EPMA Tool (Model : JEOL JXA-8530F)	45
3.14 Schematic of oxygen sensor	46
3.15 Schematic block diagram of gas sensing setup used	47
3.16 Gas sensor setup used for O ₂ sensitivity measurement	48
3.17 a) Schematic response curve of gas sensor testing. The typical characteristic values extracted from the measurement are identified on the plots b) schematic of a typical response curve of gas sensor testing . . .	49
3.18 FLIR SC 5200 IR Camera Setup	49
4.1 Schematic and photographic image of the fabricated sensor	52
4.2 Variation of thickness with deposition time	53
4.3 Cross-sectional SEM images of the CeO ₂ film deposited for (a) 200 minutes and (b) 240 minutes	54
4.4 XPS wide spectra of CeO ₂ films of various thicknesses	55
4.5 High Resolution XPS spectra (Ce-3d level) of CeO ₂ films for different thickness	55
4.6 3D AFM micrographs of CeO ₂ films of various thicknesses	57
4.7 XRD patterns of CeO ₂ films of various thicknesses	58
4.8 Variation of response of the sensor (sensitivity) and resistance with the CeO ₂ film thickness at an operating temperature of 400°C	61
4.9 Reproducible sensor's response of the 260 nm CeO ₂ film at fixed O ₂ concentration of 100%	62
4.10 Dynamic response (sensitivity) of the 260 nm CeO ₂ thin film sensor at an operating temperature of 400°C	62
5.1 Cross-sectional SEM image of the CeO ₂ -HfO ₂ film deposited for 180 minutes	68
5.2 TEM-EDS mapping of Ce-Hf film	71
5.3 SEM-EDS of Ce-Hf Analysis	72

5.4	(a) XPS survey spectra of 220 nm CeO ₂ -HfO ₂ mixed thin film; (b) high resolution XPS spectra of Ce-3d of standalone 220 nm CeO ₂ film and mixed oxide film; (c) and (d) high resolution XPS spectra of Hf-4f and O-1s of 220 nm CeO ₂ -HfO ₂ mixed thin films respectively	72
5.5	XRD patterns of CeO ₂ -HfO ₂ mixed oxide films with varying Hf concentrations	74
5.6	EPMA analysis showing the uniform distribution of Hf	76
5.7	Response of the 220 nm film for fixed concentration (100%) at an operating temperature of 400°C	77
5.8	Dynamic response of the 220 nm film at an operating temperature of 400°C	78
6.1	Simulated results of commonly used heater structures for 500μm × 500μm Velmathi <i>et al.</i> (2010).	84
6.2	Perforated Type 1 and Type 2 microheater designs of 500μm × 500μm dimension.	85
6.3	Meshing of Perforated Type 1 and Type 2 microheater.	86
6.4	Temperature Profile of Perforated Type 1 microheater.	87
6.5	Temperature Profile of Perforated Type 2 microheater.	87
6.6	Microheater Fabrication :- (a): Deposition of 1 micron PECVD SiO ₂ on RCA cleaned Si Wafer, (b): Microheater patterning and lift-off (Ti/Pt - 10/100 nm thickness).	88
6.7	The .cif file consisting of array of heater patterns created by direct writing.	89
6.8	Visual inspection of fabricated microheaters using optical microscope.	89
6.9	SEM Images of fabricated microheater patterns.	90
6.10	FLIR Image of microheaters as focused in IR Camera.	91
6.11	FLIR thermal image of Perforated Type 1 microheater showing the uniform temperature distribution along the heater.	91
6.12	FLIR thermal image of Perforated Type 2 microheater showing the uniform temperature distribution along the heater.	92
6.13	Temperature-Power curve for comparison of two types of heaters.	92
6.14	Fabrication Steps of Integrated Oxygen Gas Sensor (c) Deposition of SiO ₂ , (d) Deposition of Electrodes (Ti/Pt) (e) Sensor Film Deposition.	93
6.15	Integrated gas sensor (a) Wafer level, (b) Die level, (a) Sensor mounted on TO5 header and (b) Sensor mounted on plastic header	94

6.16	Gas sensing results on Integrated Sensor.	95
7.1	Gas Sensing film integrated with the Readout Chip in (a) Hybrid Approach and (b) Monolithic Approach Li <i>et al.</i> (2007)	98
7.2	Potential divider circuit (Shurmer and Gardner (1992))	100
7.3	Wheatstone circuit (Shurmer and Gardner (1992))	101
7.4	Chemiresistance to digital conversion circuit scheme (Leung and Wilson (2005))	102
7.5	Schematic of the designed readout circuit	103
7.6	Schematic of Gas Sensor readout circuit	104

List of Tables

1.1	Gas Sensor Applications Capone <i>et al.</i> (2003)	2
1.2	Types of Gas Sensors and their Sensing Mechanism Nazemi <i>et al.</i> (2019)	4
2.1	Comparison of CeO ₂ Sensors Performance with Reported Literature . .	25
3.1	Classifications of Deposition methods	28
3.2	Specifications of in house fabricated RF Sputtering chamber	34
3.3	Sputtering parameters of Cerium Oxide	35
3.4	Sputtering parameters for deposition of mixed oxides (CeO ₂ + HfO ₂ films)	37
4.1	Sputtering parameters used for deposition of CeO ₂	52
4.2	Summary of calculated %Ce ⁺³ and %Ce ⁺⁴ components and fraction of Ce ⁺³ components	56
4.3	Summary of Crystallite Size (D) and Texture Coefficient (TC) of CeO ₂ Films of Various Thicknesses	60
4.4	Comparison of this sensor performance with reported literature	63
5.1	Sputtering parameters used for deposition of CeO ₂ -HfO ₂	67
5.2	Summary of the oxygen gas sensing characteristics of CeO ₂ -HfO ₂ mixed oxide films (t=220 nm) deposited by varying number and size of HfO ₂ pellets	70
5.3	Summary of varied atomic concentration (by varying the size and num- ber of HfO ₂ pellets) of Ce and Hf and their corresponding gas sensing characteristic.	71

ABBREVIATIONS

μm	micro meter
AFM	Atomic force microscopy
Ce	Cerium
CeO₂	Cerium Oxide
CMOS	Complementary Metal Oxide Semiconductor
EDS	Energy Dispersive X-Ray Spectroscopy
EPMA	Electron Probe Microanalysis
HfO₂	Hafnium Oxide
HRTEM	High Resolution Transmission electron microscopy
IPA	Isopropyl alcohol
IR	Infra red
JCPDS	Joint Committee on Powder Diffraction Standards
MBE	Molecular beam epitaxy
MEMS	Micro Electro Mechanical Systems
MOCVD	Metallo-organic chemical vapour deposition
nm	nano meter
O₂	Oxygen
Op-amp	Operational Amplifier
PECVD	Plasma-enhanced chemical vapor deposition
Pt	Platinum
RCA	Radio Corporation of America
RF	Radio Frequency
SEM	Scanning Electron Microscopy
SiO₂	Silicon Di Oxide
SMO	Semiconductor metal oxide
SnO₂	Tin Oxide
TC	Texture coefficient
Ti	Titanium
XPS	X-ray photoelectron spectroscopy
XRD	X-ray diffraction

Chapter 1

Introduction to Gas Sensors

A gas sensor is a device that is used to measure the concentration of gas in its vicinity. It can also be used as a leak detector to detect a gas leak or other emissions. These sensors are designed to perform the sensing of chemical analytes and accordingly give quantitative information on the concentration of analyte that is present in the given environment. These devices, when interfaced with necessary control systems, can automatically shut down the controlled processes depending on the level of hazards.

Gas sensors are also being used for detection of toxic gases, inflammable chemicals, combustible and oxygen depletion Anukunprasert *et al.* (2005), Yuan and Shi (2013), Lin *et al.* (2019a). Gas Sensors play a vital role in many areas such as the environment, industry, transportation, medicine and agriculture Varghese *et al.* (2015), Kaushik *et al.* (2015). However the sensor technology needs to be enhanced further for better and safer environment Nag *et al.* (2015a), Nag *et al.* (2015b).

Extensive research is being carried out on gas sensor in designing miniaturized and less expensive sensors that possess the required characteristics of high sensitivity, selectivity and stability with respect to a specific application. Fast and unambiguous analysis of human surroundings will be in the near future inseparable part of public health, security and life quality control. Some of the applications are given in Table 1.1 McGrath and Scanail (2013), Capone *et al.* (2003).

The gas detection principle is based on the changes of the resistance of the sensing metal oxide thin film upon adsorption of gas molecule that is to be detected Lin *et al.* (2019b), Ji *et al.* (2019). The gas sensors are mainly classified based on their analytes or their sensing mechanism i.e based on extracted electrical parameters in response to stimulus at the input of a sensor. Fig. 1.1 lists different types of gas sensors. Table

1.2 shows the different types of gas sensors, their sensing mechanism and the variable to be monitored while sensing. The sensitivity of a sensor is the variation in these variables.

Table 1.1: Gas Sensor Applications Capone *et al.* (2003)

Automotive	Controlling Ventilation for cars, Filter control, Detection of Gasoline Vapors, Alcohol breath test, Hydrogen detectors for fuel cell based vehicles
Safety	Detection of Fire, Leaks, Toxics, Explosive and harmful gases, Boiler control, Personal gas monitor
Indoor monitoring	Natural gas alarms for Air purification, monitoring and ventilation control, LP Gas alarms, CO alarms
Outdoor monitoring	Monitoring of weather and air pollution
Food quality	Controlling the quality of food, Processing control in Food industry, Odor leakage control in packages, Agro products grading (like coffee and spices)
Industry	Controlling of Fermentation control, Chemical processes
Biomedical	Breath Analyzers, Detection of diseases

1.1 Metal oxide based Gas Sensors

Due to their small dimensions, low cost, ease of operation, and high compatibility with microelectronic processing, devices based on semiconductor metal oxide (SMO) thin films are the most promising among solid-state gas sensors McGrath and Scanaill (2013), Comini *et al.* (2002). In early 1950s, Brattain and Bardeen (1953), Heiland (1954) and Bielański *et al.* (1957) observed the effect of ambient gas on the electrical conductivity of the materials which motivated them to initiate the research on gas sensors. Seiyama *et al.* (1962) was the first person to observe gas sensing effects of adsorption and desorption in metal oxides, intense research and developments have taken place towards designing of highly sensitive, selective and stable gas sensors. In Seiyama *et al.* (1962)'s work, ZnO was used as the semiconducting layer and a variety



Figure 1.1: Types of Gas Sensors Nazemi *et al.* (2019)

of gaseous species were checked for the sensing behavior. Subsequently, other metal oxide materials were also tried for sensing behaviour. Fig. 1.2 shows the comparison of different metal oxides used as sensing materials towards development of gas sensors. As seen in the Fig. 1.2, the commonly used materials are SnO₂, ZnO, TiO₂, WO₃ and In₂O₃. During sensing, the operating temperature will be in the range of 50-500°C

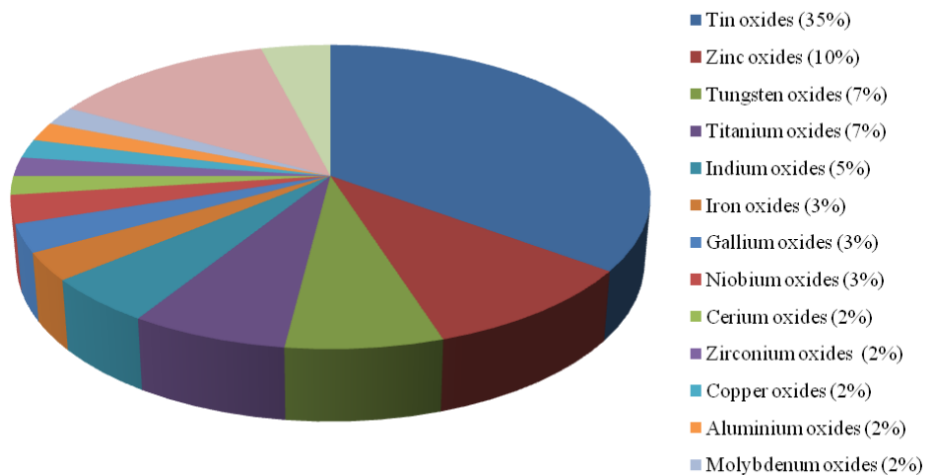


Figure 1.2: Comparison of different metal oxides used as sensing materials Eranna *et al.* (2004)

Table 1.2: Types of Gas Sensors and their Sensing Mechanism Nazemi *et al.* (2019)

Type of gas sensor	Sensing Mechanism	Variables to be monitored
Resistive	The resistance change of the sensing film on interaction of oxygen and the analyte gas will be proportional to the concentration of the analyte gas	$\Delta\rho, \Delta R$
Capacitive	It responds with the change in the property of dielectric material i.e. capacitance of the sensing film with the variation in gases of the surrounding atmosphere	$\Delta\epsilon, \Delta R$
Calorimetric	It measures the heat/temperature change due to interaction between sensing layer and the gases surrounding. The change in temperature is measured and converted into desired electrical output signal	$\Delta Q, \Delta T$
Colorimetric	A change in optical property of material (basically chemochromic) enabling a visual color change due to its interaction with the analytes	Color
Field-effect transistor (FET)	Any change in threshold voltage or drain-source current of the FET sensor (generally MOSFET), changes on interaction of the gate material when exposed to the analyte gases	$\Delta\sigma, \Delta V$ ΔI_{ds}
Mass sensitive	These sensors are either based on surface acoustic wave (SAW), quartz crystal monitor. The SAW based gas sensor works on a phenomenon of propagating mechanical waves along a solid surface which is in contact with the gases surrounding it. The shift in the resonance frequency of quartz crystal indicates the mass deposited over it. Whereas change in resonance frequency, surface stress or of deflection cantilever shows the presence of mass over them.	$\Delta m, \Delta f$
Fiber optics	Optical fibers are modified by replacing their cladding with chemically sensitive material. In the presence of selective gases, the optical property of the sensing material used as cladding changes which alters the optical parameters (phase, intensity, polarization and wavelength) of the light ray passing through the core. This change in cladding property affects the intensity or phase of the ray and the measure of it will give the presence of particular gas/chemical and their concentration.	$\Delta\epsilon, \Delta f$ polarization, $\Delta\lambda$

Commercially available semiconducting metal-oxides based sensors are manufactured by companies like AMS (2020), Figaro (2018), Bosch Sensortec GmbH (2020), Sensirion (2020), Nissha FIS, Inc. (2020) and Draeger (2020). SMO based sensors have become very popular due to the following features: portable, low-power consumption, ease of operation and less expensive when produced in mass. They can also be used as gas sensor arrays in complex systems to detect multiple gases. Also they have an excellent properties towards Sensitivity, response time, maintenance, cost, portability and posses good properties interms of accuracy, stability and durability when compared to their peers (catalytic, electrochemical, thermal conductive and IR).

In semiconductor gas sensors, the conductivity of the sensing element changes in presence of a particular gas. These devices work more efficiently at elevated temperatures, typically between 200-800 °C and hence, a heating system must be implemented in the sensor devices. The sensor is also dependent on the gas atmosphere and the properties of the sensor material used. A simple semiconductor based gas sensor (shown in Fig. 1.3) consists of a substrate typically non conducting substrates like glass, alumina, SiO₂, and so forth on which the sensor film is supported. This is followed by interdigitated electrodes which measures the conductivity changes, a measuring resistor - to control the sensor temperature. It also contains a heater to enhance sensing performance. As seen in the Fig. 1.3, fabrication of these devices is relatively easy and provides an additional advantage of direct measurement.

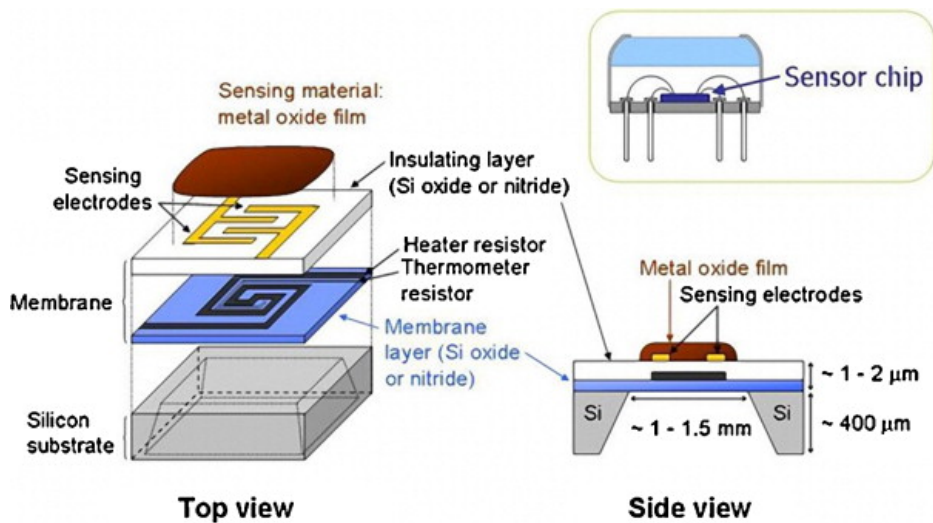


Figure 1.3: Schematic of Integrated metal oxide gas sensor Bruins *et al.* (2013)

1.1.1 Sensing Mechanism

The commonly accepted sensing mechanism of metal oxide resistive type sensors is based on changes of the resistance of a metal oxide thin film (semiconducting in nature) upon adsorption of the gas molecules to be detected. The gas-solid interactions influence the density of electronic species in the film and thereby the resistance of the film. This means reducing gases are oxidized on the sensor surface. They act as donors and therefore provide additional electrons, which increase the conductivity of n-type semiconductors. Oxidising gases on the other hand, increase the number

of oxygen ions on the sensor surface. They act as acceptors, i.e., they decrease the sensor conductivity Göpel (1991). The fundamental sensing mechanism for most metal oxide-based gas sensors relies on the change in electrical conductivity due to charge transfer between surface complexes, such as O^- , O^{2-} , H^+ , and OH^- , and interacting molecules. The main chemical reaction in the metal-oxide gas sensor is the ionization of oxygen adsorbed on the surface of the sensing metal oxide film.

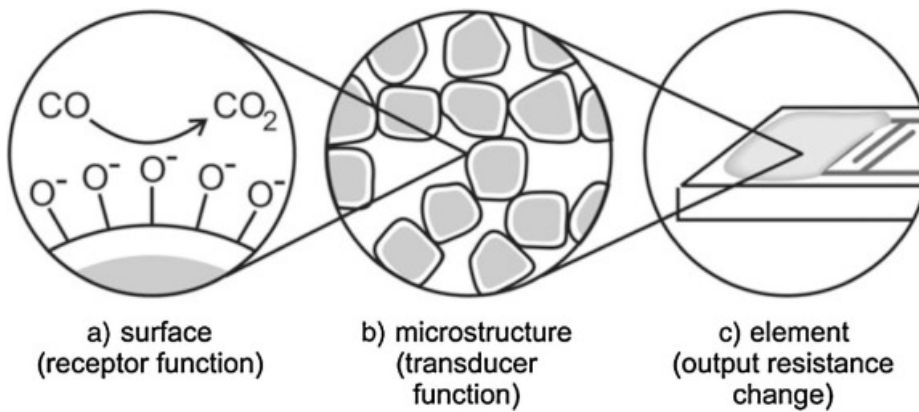


Figure 1.4: Different operational modes of gas sensor Dey (2018)

At elevated temperature ($>150^\circ\text{C}$), oxygen is available in different forms : O_2 , O_2^- , O^- , O^{2-} , etc. In general, O^- will react rapidly with reducing agents present on the surface, O_2^- will react slowly and O_2 will be essentially non-reactive. Under ambient conditions; when oxygen ions interact chemically with any semiconductor surface, this creates extrinsic surface acceptor states in the near-surface region. In that case, under the interaction of oxygen ions, each grain surface is depleted of electrons. This ultimately leads to change in the conductivity of the semiconductor. Depending on the type of semiconductor : n-type or p-type, the change in the conductivity either increases or decreases. For n-type semiconductor, the immobilization of electrons in the conduction band by the acceptor (oxidizing gas or oxygen ions) decreases the conductivity and hence, increases the resistance of the sensing film. On the other hand, for p-type semiconductors, the immobilization of electrons (i.e. minority charge carrier) by the acceptor increases the conductivity and hence, reduces the resistance of the sensing film.

1.1.2 Basic Characteristics of Semiconductor Gas Sensors

The electrical resistance sensor film changes when exposed to the molecules of analyzing gas. Change in resistance depends on the nature of sensor material (n-type or p-type) and the type of gas (reducing or oxidizing). A typical response curve showing the variation of resistance of sensor with time on exposure and withdrawal of analyzing gas, is shown in Fig. 1.5.

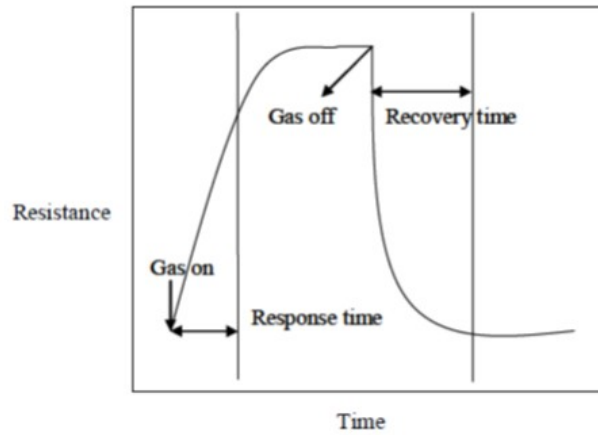


Figure 1.5: Response-curve of a chemiresistive gas sensor Hassan (2017)

Depending on the type of conductivity (n-type or p-type) of the films, the resistance of the film will increase or decrease accordingly. Thus the resistance changes for a semi-conducting film exposed to reducing/oxidizing gases can be summarized as follows. For n-type semiconductor materials, the resistance increases for oxidizing gas and decrease for reducing gases. It will be vice-versa for p-type.

The response curve (shown in Fig 1.5) of Semiconductor Gas Sensors is characterized by the following parameters:

- **Sensitivity (S):** It is the smallest volume concentration of the target gas that can be sensed in the time of detection. The sensitivity is highly dependent on film porosity, film thickness, operating temperature, presence of additives and crystallite size. For n-type semiconductor metal oxide sensors, the sensitivity for reducing gases is given in equation 1.1 and for oxidizing gases, it is defined in equation 1.2 :

$$S = \frac{R_a}{R_g} \quad (1.1)$$

$$S = \frac{R_g}{R_a} \quad (1.2)$$

where R_g is the resistance of the gas sensor in presence of target gas and R_a is the resistance of gas sensor in presence of reference gas.

The sensitivity of p-type semiconductors metal oxides sensors has the opposite definition.

- **Selectivity:** It is related to the discrimination capacity of a gas-sensing device for a mixture of gases. In other words, selectivity refers to the sensor's ability to detect a analyte gas in the presence of other analytes.
- **Stability:** It is a characteristic that takes into account the repeatability of device measurements for the given period of time. The success of the sensor will be limited if the sensor performance is not demonstrated as repeatable and stable over long-term testing.
- **Response time:** The time for a sensor to respond from zero concentration to a step change in concentration. It is usually specified as the time to rise to a definite ratio of the final value. Thus, if t_{90} represents the response time which is the time taken by the sensor to reach 90% of the full-scale output, a small value of response time would be indicative of a good sensor.
- **Recovery time:** This is the time interval over which the sensor resistance reduces to 10% of the saturation value when the sensor is exposed to full scale concentration of the gas and then placed in clean air. A good sensor should have a small recovery time so that sensor can be used over and over again in quick succession.
- **Reproducibility :** The ability of the sensor to give the same output when measuring a constant input measured on a number of occasions.

1.2 Need for Oxygen Sensor

An oxygen sensor is a device that measures the proportion of oxygen (O_2) in the gas or liquid being that is being analysed.

Oxygen is very much essential for life and without sufficient amount of oxygen we cannot live. By volume, dry air contains 78.09% nitrogen, 20.95% oxygen, 0.93% argon, 0.04% carbon dioxide, and small amounts of other gases (shown in Fig. 1.6). The composition of air constantly varies due to the presence of water vapor. Other substances which contribute to the variations are O_3 , CO, S and NO_x and several VOC's. When concentration of these substances increase, the oxygen concentration is greatly reduced locally leading to oxygen deficiency. Since oxygen is odorless, its shortage in atmosphere can only be perceived by the side effects on the respiratory processes.

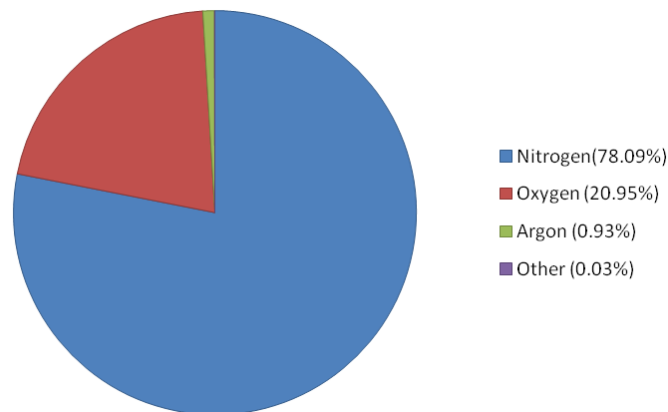


Figure 1.6: Atmospheric air composition

Atmospheric gases are non-toxic. However, when they increase in concentration, they have a great impact on life and combustion processes (specifically with oxygen). Even though oxygen is not flammable, it does support combustion. When there is change in the natural composition of air, human beings will be affected or even severely impaired which may also result in death. Oxygen deficiency occurs when other gases get added or mixed with air resulting in reduction of oxygen concentration (dilution) No human sense organ will give a quick indication of oxygen-reduced atmosphere. On the other hand, leaks in oxygen cylinder must be continuously monitored, as in the case of medical diagnostic centers and in hospitals. Hence for faster detection of oxygen concentration, these sensor devices should be placed close to potential leak points. Linde (2015).

1.2.1 Hazards from Oxygen Deficiency

Healthy human beings may survive exposure to low oxygen content (as low as 16%) for a very short duration. Unfortunately, any significant drop in oxygen levels is not accompanied by immediate signs making the deficiency impossible to be detected by humans. Thus, oxygen level sensors are essential part of any life critical medical equipments.

Another potential application of oxygen sensors is in automotive industry, where highly efficient sensors are invariably used in an exhaust of the automobile system to monitor and control the emission levels from the vehicles. Such fuel control mechanisms help in reducing the air pollution and in turn improves the quality of human life Amaechi and Godstime (2015), Brailsford and Logothetis (1998).

1.3 Materials for Gas Sensors

Fig. 1.7 shows the literatures available on sensors for different gaseous species Eranna *et al.* (2004). Carbon monoxide and nitrogen oxides share 16% each, hydrogen at 11%, ethanol vapor at 8%, carbon dioxide at 7%, oxygen at 6.8%, methane at 6%, and ozone is at 4%. The Semiconductors gas sensors are projected to dominate in the future, as they monitor air quality on a real-time basis. Thus, these sensors are widely used in air quality monitoring systems. It is expected that the gas sensors will play a pivotal role based on the type of gas to be sensed (Oxygen Sensors, Carbon Dioxide Sensors, Carbon Monoxide Sensors, Nitrogen Oxide Sensors, and Others) and by the type of application (Medical, Building Automation & Domestic Appliances, Environmental, Petrochemical, Automotive, Industrial, and Others).

Worldwide, the demand for oxygen sensors has been growing every year as the regulations become more and more stringent. Oxygen analyzers play a very important role during pandemics like SARS, COV-19, etc. where the oxygen level needs to be continuously monitored. Oxygen micro-sensors with better performance, e.g., faster response and light-off times, need to be developed.

Fig. 1.8 shows the table of sensing behavior of gaseous species for different metal oxides. It is evident that tin oxide is sensitive to maximum number of gaseous species. Fig. 1.8 helps in selection of metal oxide for specific gas detection. However, it also depends on the environment under which the detection is being carried out. Also in an unknown environment, the measured signals will be very difficult to analyze and

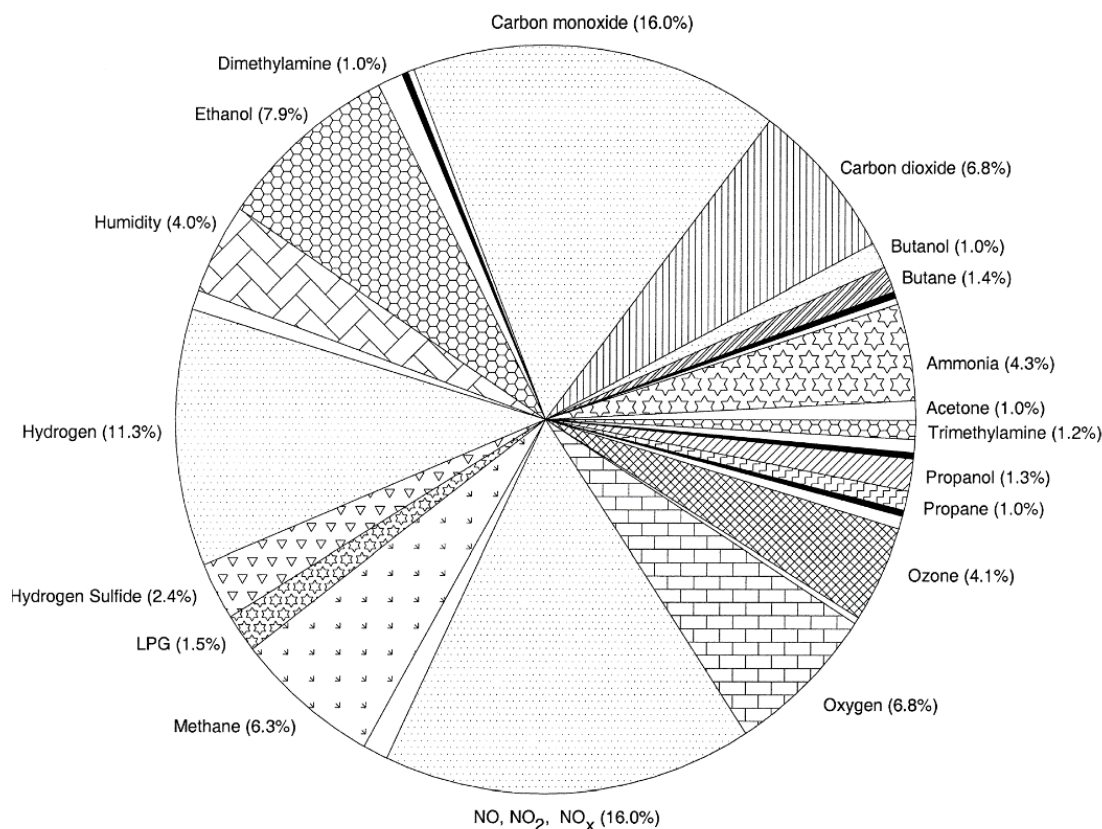


Figure 1.7: Relative comparison of different oxides used for gas-sensing application Eranna *et al.* (2004)

quantify. Although, SnO_2 sensors have been used for most of the gases, it has some disadvantages, namely, selectivity issues, large power consumption, long stabilizing time and influence of atmospheric humidity.

The above literature survey of various SMO's as sensing materials has given the motivation for selecting Cerium Oxide (CeO_2) as the sensing material for this thesis.

Current Research is aimed towards obtaining an accurate oxygen sensor by improving the three main parameters, namely, high Sensitivity, selectivity and stability.

Cerium oxide (CeO_2) is a wide bandgap 3.2 eV and 26th most abundant rare earth metal oxide. Cerium (Ce) is the chemical element with an atomic number of 58 and it is the second element in the lanthanide series. Cerium oxide (CeO_2) is a n-type semiconductor and is a very good electronic as well as ionic conductor Majumder and Roy (2018).

Ceria based materials are promising for number of applications, due to its chemical

Gas	Metal oxides																				
	Al	Bi	Cd	Ce	Cr	Co	Cu	Ga	In	Fe	Mn	Mo	Ni	Nb	Ta	Sn	Ti	W	Zn	Zr	Mx
Acetone (CH ₃ -CO-CH ₃)			X							X				X		X			X		
Acetaldehyde (CH ₃ CHO)																X					
Ammonia (NH ₃)					X	X		X	X			X	X	X		X	X	X	X		X
Arsine (AsH ₃)																X					
Automobile exhaust gases								X								X					X
Benzene (C ₆ H ₆)																X					
Butane (C ₄ H ₁₀)	X							X	X	X						X			X		
Butanol									X					X		X			X		
Carbon dioxide (CO ₂)	X	X	X	X	X	X	X			X			X			X	X		X	X	X
Carbon monoxide (CO)		X				X	X	X	X	X		X	X	X		X	X	X	X	X	X
Chlorine (Cl)									X							X					
Dimethyl disulfide																X			X		
Dimethylamine (DMA)									X					X		X	X	X	X		
Ethane (C ₂ H ₆)																X			X		
Ethanol (C ₂ H ₅ OH)	X			X			X	X	X	X		X		X		X	X	X	X	X	X
Humidity (H ₂ O)	X									X	X				X	X		X	X		X
Hydrocarbons (HC)																X				X	X
Hydrogen (H ₂)	X	X	X	X	X		X	X	X				X			X	X	X	X	X	X
Hydrogen sulfide (H ₂ S)				X			X									X		X	X		X
Inflammable Gases																X					
Liq Petroleum Gas (LPG)								X	X							X			X		X
Methane (CH ₄)					X	X		X	X				X			X	X		X		X
Methanol (CH ₃ OH)	X			X												X	X				
Methyl mercaptan (CH ₃ SH)																X					
NO, NO ₂ , NO _x					X	X		X	X	X		X	X			X	X	X	X	X	X
Oxygen (O ₂)	X	X	X	X	X	X	X	X	X	X		X	X			X	X	X	X	X	X
o-xylene																X					
Ozone (O ₃)								X	X		X					X	X	X	X		X
Petrol/Gasoline																X		X	X		
Phosphine (PH ₃)																X					
Propane (C ₃ H ₈)						X		X	X	X						X			X		
Propanol (C ₃ H ₇ OH)								X						X		X	X		X		
Smoke		X														X					
Sulfur dioxide (SO ₂)													X			X					X
Trimethylamine (TMA)								X						X		X	X	X	X		

Figure 1.8: Comparison of gaseous species studied by using various metal oxides Eranna *et al.* (2004)

stability and their suitability in technology applications, they have been widely investigated in recent years. It is having a lot of applications such as, protective coatings on superconducting thin films Aguiar *et al.* (1997), corrosion resistant coatings Di Maggio *et al.* (1997), electrochromic layers Aegerter *et al.* (1997), gate insulators on silicon Tye *et al.* (1994), gas sensors Gerblinger *et al.* (1995), electrolytes and electrodes in electrochemical process Pan *et al.* (1998), superconductor- insulator-semiconductor Qiao and Yang (1995), silicon on insulator (SOI) Morshed *et al.* (1997), as intermediate buffer layers for HTS and GMR perovskite films Castro *et al.* (1995), Dahmen and Carris (1997), dielectric layer structures in integrated circuits Fukuda *et al.* (1998), VOC sensors Majumder and Roy (2018), as sun screen cosmetics Yabe and Sato (2003), UV absorbent Wang *et al.* (2019) in Solid Oxide Fuel Cells (SOFCs) Jaiswal *et al.* (2019),

in biology, glucose sensor Qian *et al.* (2020), Triglyceride sensor Solanki *et al.* (2009), Cholesterol biosensor Patil *et al.* (2012) and in hydrogen peroxide sensors Malyukin *et al.* (2018).

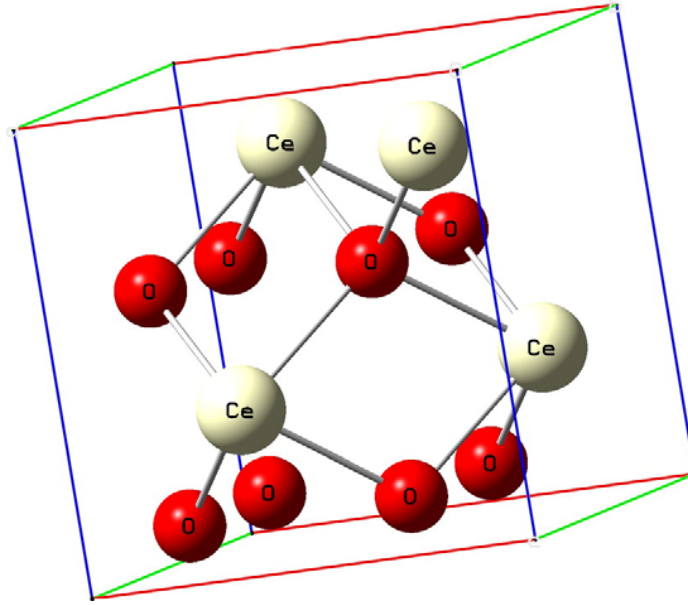


Figure 1.9: Cerium dioxide cubic fluorite structure Bumajdad *et al.* (2009)

Fig. 1.9 shows, schematically, the fluorite structure of ceria. The Ceria has fluorite structure with the oxygen four coordinate and cerium eight coordinate: one cerium atom is surrounded by eight oxygen atoms with space group $Fm\bar{3}m$.

Ceria based materials are promising materials for a number of applications due to their excellent properties such as chemical stability, thermodynamic stability, high thermal shock resistance, good dielectric properties, good ionic and electronic conductivity Millot and De Mierry (1985). Due to its unique property of co-existence as trivalent (Ce^{+3}) and tetravalent (Ce^{+4}) states of Ce atom and their ease of transition from one to another makes CeO_2 a promising candidate for oxygen storage, catalysis and gas sensing Trovarelli and Fornasiero (2013), Liu *et al.* (2012), Izu *et al.* (2002b). Formation of non-stoichiometric CeO_2 can occur due to oxygen release and reduction of Ce^{+4} to Ce^{+3} . The ratio of Ce^{+3}/Ce^{+4} states and oxygen vacancies play a crucial role in determining its oxygen storage capacity (OSC) Majumder and Roy (2018), Kašpar *et al.* (1999). It is mainly the oxygen vacancy distribution which governs the OSC of CeO_2 . Also, the OSC has been found to have strong dependency on orientation of crystal planes Mullins *et al.* (2012).

1.4 Research Objectives

Several sensors are available commercially for leak detection, yet they are bulky, expensive and consume more power. Considering these factors, it is proposed to develop Micro Electro Mechanical Systems (MEMS) Resistive based Oxygen sensors for leak detection since MEMS, when combined with appropriate metal-oxide sensing films, offer a small, low cost, and low power platform.

The main objective of this research is,

- To deposit CeO_2 sensor films by RF Sputtering technique and to optimize the process parameter (thickness) for sensing oxygen gas at reduced operating temperature.
- To deposit mixed oxide ($\text{CeO}_2 + \text{HfO}_2$) sensor films by RF Sputtering technique to improve the sensor performance in terms of response time, recovery time and sensitivity.
- To design and fabricate microheater, which is a key component of the gas sensor for providing very high temperature uniformity at low power consumption.
- To design read-out electronic circuitry.

1.5 Thesis Organization

Chapter 1 gives an introduction to gas sensors, their types, sensing mechanisms, basic characteristics and their applications. It also lists the research objectives and thesis organization.

Chapter 2 describes the review of work carried out on CeO_2 based films for oxygen sensor applications which is the main objective of this thesis. It emphasizes different deposition techniques to process the CeO_2 films, the effect of process parameters on characteristics of CeO_2 films.

Chapter 3 gives a detailed presentation on the adopted deposition technique and characterization techniques used in this study for the realization of gas sensing devices.

Chapter 4 presents the development of relatively low operating temperature CeO_2 thin film based oxygen gas sensors using RF sputtering by optimizing the process parameters and thickness.

Chapter 5 explains the synthesis of mixed oxide ($\text{CeO}_2 + \text{HfO}_2$) thin films by a novel technique in RF sputtering. The sensing performance and characteristics are evaluated using various characterization techniques such as TEM-EDS, SEM-EDS, XPS and XRD.

Chapter 6 describes the microheater designs and fabrication. This chapters gives the detailed simulation results of the two proposed microheater structures. This is followed by the realization of microheaters wherein various process steps involved in fabrication of microheaters is elaborated. Finally, the results of the prototype integrated gas sensor have been discussed.

Chapter 7 presents the design of the interface electronics circuit for thin film gas-sensors. It presents different approaches used in the read-out task and describes the chosen solution. The chapter also illustrates the circuit designed and reports its results.

Chapter 8 concludes the thesis by summarizing major research contributions and throws some light on future scope and possibilities of further research.

Chapter 2

Literature Survey

2.1 Introduction

As described in the previous chapter, Cerium oxide (CeO_2) is a wide band gap rare earth n-type semiconductor and is a very good electronic as well as ionic conductor. Ceria based materials are promising for a number of applications due to their excellent properties such as very good adhesion, high thermal shock resistance, chemical stability, good dielectric properties, good ionic and electronic conductivity, and no apparent aging under changing gas compositions Millot and De Mierry (1985). Thus, CeO_2 has been found in various applications such as optoelectronics, solid oxide fuel cells, heterogeneous catalysis and corrosion protection.

In general, thin films of CeO_2 possess columnar microstructure with a packing density of about 0.6 Netterfield *et al.* (1985). Hence these films are highly porous and are suitable for gas sensing applications. In addition to this, CeO_2 exhibits good oxidation-reduction properties at a broad range of temperature with excellent properties in gas sensing applications. CeO_2 is being used for oxygen sensing because of its high diffusion coefficient for oxygen vacancies and excellent chemical stability Beie and Gnörich (1991), Jasinski *et al.* (2003). CeO_2 has also been used as gas sensor for detection of gases such as NO, CO, Acetone, H_2S etc., Bene *et al.* (2000), Majumder and Roy (2018), Oosthuizen *et al.* (2020), Eranna *et al.* (2004).

This chapter describes the review of work carried out on CeO_2 based films for oxygen sensor applications which is the objective of this thesis. It emphasizes different deposition techniques to process the CeO_2 films, the effect of process parameters on characteristics of CeO_2 films.

2.2 CeO₂ film processing

Over several decades, many materials have been prepared in the form of thin films because of their technical values and of scientific curiosity in their properties. They have very wide range of applications extending from nanometer dots in nanoelectronics to coatings of several square meters on window glasses. Various techniques have been examined in search for the most reliable and economical method of producing such thin films. These include thin films resulting from oxidation of an evaporated metal, reactive and non-reactive sputtering techniques, thermal evaporation, molecular beam epitaxy, electron beam evaporation, ion plating, electro deposition, electroless deposition, anodization, chemical vapour deposition etc. Owing to their simplicity and inexpensiveness, chemical techniques have also been studied extensively for the preparation of thin films. Moreover, they facilitate materials to be designed on a molecular level.

Different deposition techniques have been used to form CeO₂ films, each with its own specific advantages and disadvantages. The commonly accepted deposition techniques are Physical Vapor Deposition (PVD), Metal-Organic Chemical Vapor Deposition (MOCVD), and Atomic Layer Deposition (ALD). As opposed to CVD techniques, PVD has the main advantage of not suffering from contamination originating from the precursor molecules. On the other hand, step coverage of 3D architectures is a specific concern in PVD techniques.

2.2.1 Screen Printing

The required quantity of CeO₂ powder is taken along with equal weight of the organic binder (usually terpincol or ethyl cellulose) and both are mixed thoroughly by blending in hybrid mixer to form a paste. This paste is then screen printed onto the cleaned substrates using a prefabricated screen with required window dimensions. This screen printed films will be further calcined in a furnace at a particular temperature and duration. The screen printing step is repeated to obtain thicker films. After each print, the film is dried for a short duration.

It provides very little material wastage, high packing density and high throughput. However controlling the profile is an issue. While drying, phase segregation and inhomogeneities occur.

2.2.2 Precipitation and Co-Precipitation

Chemical precipitation is widely used for synthesizing solid materials from solution. This method utilizes a liquid phase reaction to prepare insoluble solid that are crystalline or amorphous precipitates. Usually, ceria precipitation is carried out by calcinations of hydroxide or oxalate gel precipitated using the reaction of aqueous solution of inorganic cerium salt $\text{Ce}(\text{NO}_3)_3$, CeCl_3 , and $(\text{NH}_4)_2\text{Ce}(\text{NO}_3)_6$ with alkali solution NaOH , NH_4OH and $(\text{NH}_2)_2\text{H}_4\text{O}$ Leitenburg *et al.* (1997), Audebrand *et al.* (2000). However simply adding of solutions of the precipitant has little control on particle size and morphology because of the rapid change of solution concentration and discontinuous nature of precipitates formation. To overcome this disadvantage to some extent, a homogeneous precipitation method has been developed. In this process, precipitants are generated simultaneously and uniformly through the solution using controlled release of the reaction- participating ligands by another chemical source in the solution.

In the synthesis of mixed oxides, the co-precipitation method is a commonly used wet-chemical process. Generally salts of several metals are dissolved in the same solvent, usually water. This method consists of simultaneous precipitation from the precursor under reaction condition depending upon pH and concentration. But difference in solubility between several precipitating phases affects the precipitation kinetics of each metal ion component. Nanocrystalline CeO_2 particles of 5 nm was successfully prepared by the precipitation method using hydrogen peroxide as an oxidizer Choi *et al.* (2006). Co-precipitation method was utilized by Li *et al.* (2000), Fu *et al.* (2001), Liu and Flytzani-Stephanopoulos (1996) to synthesize a series of mixed oxide ceria catalyst (Au/CeO_2 , Pt/CeO_2 , $\text{NiO}-\text{CeO}_2$, $\text{CuO}-\text{CeO}_2$) for water-gas shift reaction and CO oxidation. Many other mixed oxide solid solutions such as $\text{Ce}_{1-x}\text{Zr}_x\text{O}_2$ ($x = 0.33$ and 0.5) Masui *et al.* (1998), Sergent *et al.* (2000), $\text{Ce}_{0.9}\text{M}_{0.1}\text{O}_{2-\delta}$ ($\text{M} = \text{Nd}, \text{Y}, \text{Ba}, \text{Sr}, \text{Pb}, \text{Mn}, \text{Co}$ and Cu) Zhang *et al.* (1995) were also synthesized by this method.

2.2.3 Sol-gel synthesis

This method is the extension of co-precipitation method. The method mainly constitutes careful selection of solvents, which leads to formation of a gel of required composition followed by slow drying and finally calcinations at higher temperature

for longer durations. Basically the sol-gel method is based on inorganic polymerization reactions. This process includes four steps: hydrolysis, polycondensation, drying and thermal decomposition. This method is specially suited for the synthesis of oxide materials at relatively low temperatures. Metal alkoxide and metal chloride are typical precursors. The process involves conversion of metal alkoxide/chloride solution into a colloidal suspension (sol) and gelation of the sol to form discrete particles or network polymers in a continuous liquid phase (gel). The particles are amorphous or crystalline and the particle aggregation is prevented by electrostatic repulsion. The particle size depends on the temperature, pH, solution composition, etc. Work carried out by Sol-gel synthesis has been reported in the next section.

2.2.4 Spray Pyrolysis

Spray pyrolysis is a thermally stimulated reaction between clusters of liquid and vapour atoms of different chemical species. This atomization technique of chemical species involves spraying a solution containing soluble salts with the help of a compressed gas or air through a nozzle. During this process, precursor solution is pulverized by means of a neutral gas (e.g., nitrogen) so that it arrives at the substrate in the form of very fine droplets. The compressed air or gas called as the carrier gas, which carries the atomized fine droplets may or may not play an active role in the pyrolytic reaction. The chemical reactants are selected such that the products other than the desired compound are volatile at the temperature of deposition. Thus the sprayed fine droplets on reaching the surface of the hot substrate undergo a chemical decomposition and reaction to form the required compound, which get adsorbed with the substrate, producing a thin film. These adsorbed molecules form the nucleus for the growth of crystallites or crystals contained in the thin films. As more and more droplets reach the substrate, clusters of nuclei cling together to form the crystallites resulting in film growth. The liquid solvent serves to carry the reactants and distribute them uniformly over the substrate area during the process.

Spray pyrolysis possess a number of advantages such as :

- Low cost (inexpensive apparatus, does not require high quality targets or vacuum).
- Easy control of composition and microstructure (facile way to dope material by merely adding doping element to the spray solution).

- Deposition at moderate temperatures of 100 - 500°C.
- Technological ability for mass production Patil (1999), Tomar and Garcia (1981).

They also have some disadvantages such as :

- Possible oxidation when processed in air atmosphere.
- Difficulties with growth temperature determination.
- Long processing time may render spray nozzle cluttered.
- Film quality depends on the droplet size and spray nozzle.

2.2.5 Spin coating

The spin coating process is a very useful technique owing to its versatility, effectiveness and practicality. The operation can be done in ambient conditions.

The solution precursors are prepared by placing 2g of cerium (III) nitrate hexahydrate ($\text{Ce}(\text{NO}_3)_3 \cdot 6\text{H}_2\text{O}$), and 0.2g of 10% polyvinyl alcohol (PVA) in 20 ml de-ionised water (DI H_2O). This solution is magnetically stirred for a certain duration for complete dissolution.

A typical spin coating process involves depositing a small puddle of a chemical solution resin onto the centre of a substrate followed by spinning the substrate at high speed, typically 3000 rpm. The centripetal acceleration will cause the chemical solution resin to spread to, and eventually off, the edge of the substrate. As the spin process continues, evaporation of the chemical solution takes place leaving behind a thin film on the substrate surface.

2.2.6 Metal Organic Chemical Vapor Deposition (MOCVD)

MOCVD is a flexible CVD technique, which allows good uniformity across the wafer and controlled growth of highly conformal films on planar and high-aspect ratio substrates. The particle formation during the deposition can be limited by using liquid precursors. High deposition temperature in the range of 400 - 600°C is used. Variation in pressure and gas flow results in variation in film composition. Though it is a potential deposition method, it introduces carbon contaminants. Further, it has less control on film composition and has high cost Choi *et al.* (2011).

2.2.7 Physical Vapor Deposition Techniques (PVD)

Though PVD processes have been commonly used for growing oxide films, it has been minimally explored for growing CeO_2 materials for oxygen sensing applications. Among the major concerns of preparing CeO_2 by chemical routes is uncontrolled oxidation and impurities since most of the processes are carried out in an open atmosphere. Moreover controlling the thickness of these films is really a challenging task and the films become pretty thick (ranging from micrometer to millimeter). Some advantages of RF sputtering are listed below:

- Sputtered atoms are of very high energy which leads to growth of high density thin films on the substrate
- Sputtering can be achieved from large-size targets, simplifying the deposition of thin films with uniform thickness over large wafers.
- Film thickness is easily controlled by fixing the operating parameters and by adjusting the deposition time.
- Sputtering provides better adhesion and step coverage, less radiation damage, easier to deposit alloys.
- Controlled deposition to achieve required stoichiometry of films.
- Sputter-cleaning of the substrate in vacuum prior to film deposition.
- The key benefits of sputtering are the speed of process, deposition rate stability and the processes can also be fully-automated.

2.3 Works reported on development of oxygen sensor using CeO_2 as sensing material

Beie and Gnörich (1991) have used CeO_2 in both thick and thin films form and developed a prototype oxygen sensor. The thickness of the thick films prepared by spin coating was in the range of 5-50 μm and 5-30 μm for screen printing. Ceria thin films were deposited by RF Sputtering technique and the thickness was between 0.5 to 1.5 μm . The authors concluded that responsiveness of oxygen gas sensors improved

when the particle size of the sensors were reduced from $7\ \mu\text{m}$ to $2\text{-}3\ \mu\text{m}$ and that the sensor kinetics were controlled by surface reaction. However they found that the response time was approximately 10 ms when the surface reaction rate is higher than the oxygen vacancy diffusion rate. The operating temperature was between $800\text{-}1000^\circ\text{C}$.

Later, Izu *et al.* (2002a), prepared Cerium oxide powder by mist pyrolysis and this powder was mixed with organic binder to form a paste which was screen printed. The response time was calculated as a function of diffusion coefficient, surface reaction coefficient and particle size. The response time obtained for particle size of $1\ \mu\text{m}$ or less was 35 s, 22 s, 15 s, 11 s and 8 s while operating at 1081 K, 1130 K, 1178 K, 1226 K and 1275 K temperatures respectively.

Further Izu *et al.* (2002b) prepared CeO_2 fine powder with an average particle size of 200nm. Using this powder, resistive oxygen gas sensors were fabricated by screen printing. The thickness was between $20\text{-}30\ \mu\text{m}$ and they achieved a response time of 10 s at an operating temperature of 712°C

Again, Izu *et al.* (2003b), reported fabrication of oxygen sensors based on CeO_2 porous thick films having an average particle size of 100nm and they have shown the response time as 11 s at an operating temperature of 615°C for CeO_2 films of thickness $20\text{-}30\ \mu\text{m}$, synthesized by screen printing technique. They concluded that the response time of the sensor could be reduced by decreasing the particle size of the thick film.

Izu *et al.* (2003a) fabricated the resistive oxygen gas sensors based on cerium oxide porous thick film by firing powder with various particle sizes at various temperatures to investigate the effects of changes in particle size and firing temperature on the response time for resistive oxygen gas sensor. They concluded that the response time was unaffected by particle size, but clearly depended on the firing temperature. The response time for the sensor using original powder fired at 1373 K was shorter than that using powder fired at 1473K; the crystallite size grew as the firing temperature increased. They further reported that the optimum particle size of the resistive oxygen sensors based on cerium oxide porous thick film should be 100-500 nm.

Manorama *et al.* (2003) reported that the CeO_{2-x} ($1.5 < x < 2$) is an n-type semiconducting oxide with fluorite structure which is suitable for oxygen gas sensing. They demonstrated that the sensitivity as well as the response time could be improved by using nanosized CeO_2 (50-100 nm) particles. They reported a response time of 9 s at an operating temperature of 905°C . The sensitivity exhibited a peak (around 0.30) at an operating temperature in the range of 1081–1178 K.

Jasinski *et al.* (2003) prepared dense thin films of CeO₂ by spin coating a polymer precursor solution onto a sapphire substrate. The solution was later coated onto a substrate and the typical thickness was 50nm per deposition. Multiple depositions allowed the film thickness to be increased into the micron range and the grains size of the film was controlled by the annealing temperature. The response was shown to be around 60s at an operating temperature of 700°C. They concluded that the temperatures in the range from 700 to 750°C appeared to be the best for sensor operation because of the fast response to the changes of oxygen concentration and moderate resistance range.

Izu *et al.* (2004) fabricated oxygen sensors with thin films of single-phase cerium oxide prepared by metal organic chemical vapor deposition (MOCVD) and sputtering, and investigated the properties of both sensors. The response times of the thin films (500 nm) prepared by MOCVD and sputtering were about 9 s when the films were heated to 888 K for the first time. However, the response time increased upto 80 s each time the sensor was heated to 1274 K. The deterioration of the response time in this study seems to be related to increasing crystallite size. It was concluded that the thin film prepared by sputtering was suitable for oxygen sensors compared with that prepared by MOCVD.

Liu *et al.* (2012) prepared large scale and polycrystalline CeO₂ nanofibers with an average diameter of 376 ± 55 nm using a facile two-step synthesis route including electrospinning and calcination. The as-prepared CeO₂ nanofibers showed good morphological and structural stability in high temperature environment (800-1000°C) and were further employed for in situ, real-time oxygen (O₂) and carbon monoxide sensing at 800°C and 1000°C, respectively, both of which showed sensitive, reversible and reproducible response. The response was 30 s at 800°C and 28 s at 1000°C.

Chen and Chang (2012) used as-precipitated CeO₂ with various amounts of ZrO₂ powders for screen printing onto Al₂O₃ substrates for the investigation of oxygen sensor properties. Zirconium ions were directly added into the CeO₂ ceramics during the preparation of precursor solutions to investigate the effect of ZrO₂ on the oxygen sensing behavior. The crystallite size of as-precipitated CeO₂ was decreased by doping with ZrO₂ and even after heat treatment at 1473 K, the ZrO₂-doped CeO₂ (ZDC) films still exhibited smaller grain sizes compared to the undoped equivalent. The response time of 10% doped ZrO₂ was 16 s at 1123 K and 17 s at 1073 K, but the recovery time was prolonging. It was concluded that doping with ZrO₂ may increase the amount of

Ce³⁺ in CeO₂, enhancing the conductivity of the solid solution film. Moreover, the smaller grain size of ZDC film may lower its resistance activation energy.

Chen *et al.* (2014) coated porous ceria films on the electrodes using different mixtures of two undoped ceria powders synthesized by spray-pyrolysis and precipitation respectively and the ratios of the two powders were varied to produce differences in the heat-treated porosity of the ceria films. The response time was between 11 s to 31 s at an operating temperature of 1073 K and 1123 K. The authors had concluded that the shortest response time was obtained due to the optimized porous structure, which provided sufficient paths for sensed gas to penetrate into the sensor coating.

Trinchi *et al.* (2003) prepared the CeO₂-TiO₂ thin films by sol-gel process using a non-alkoxide as the main precursor and presented good oxygen sensing performance at operating temperatures below 470°C. Several 0.15M solutions of different Ce-Ti atomic ratios were prepared. The response time at 420°C was typically between 40 and 60 s whereas the recovery time was approximately 80 s. It was shown that titanium segregation on the surface of the samples and its amount in the precursor solution can influence the Ce/Ti atomic ratio on the sample's surface. The cerium chemical state is influenced from the Ce/Ti atomic ratio in the precursor solution and from the annealing temperature. It was found that the CeO₂ dominated sensors have lower baseline resistance and larger response than those with higher concentrations of titanium.

It may be noted that CeO₂ films have been commonly prepared and synthesized by several processing methods such as Laser ablation, D.C. sputtering, Electron beam evaporation and Molecular beam epitaxy (MBE) Mihalache and Pasuk (2011), Nandasiri *et al.* (2011), Durrani *et al.* (2008), Anwar *et al.* (2011), Hollmann *et al.* (1993).

Films of CeO₂ have also been obtained by using chemical methods mainly by Metallo-organic chemical vapour deposition (MOCVD), Sol-gel processes, Spray pyrolysis and Mist pyrolysis Beie and Gnörich (1991), Izu *et al.* (2002a), Izu *et al.* (2003b), Shin *et al.* (2004), Manorama *et al.* (2003), Izu *et al.* (2002b)].

Most of the work reported (shown in Table 2.1) on CeO₂ for gas sensing applications has been carried out by chemical methods and also the thickness of the CeO₂ films are in the range of micrometer to millimeter Beie and Gnörich (1991), Izu *et al.* (2002a), Izu *et al.* (2003b), Shin *et al.* (2004), Manorama *et al.* (2003), Izu *et al.* (2002b), Jasinski *et al.* (2003), Izu *et al.* (2003a), Chen and Chang (2012), Gerblinger *et al.* (1995). Very few reports are available on the synthesis of CeO₂ films using

Table 2.1: Comparison of CeO₂ Sensors Performance with Reported Literature

Synthesis Method	Thickness	Operating Temp. (°C)	Response Time	Ref
Screen printing RF Sputtering	5-30 μm 0.5-1 μm	800	10 ms (Estimated by Fick's second law)	Beie and Gnörich (1991)
Mist Pyrolysis	–	808	35 s	Izu <i>et al.</i> (2002a)
		857	22 s	
		905	15 s	
		953	11 s	
		1002	8 s	
Mist Pyrolysis	20-30 μm	615	11s	Izu <i>et al.</i> (2003b)
Mist Pyrolysis	20-30 μm	712	10s	Izu <i>et al.</i> (2002b)
Mist Pyrolysis	30 μm	615	11-42 s	Izu <i>et al.</i> (2003a)
		662	16-20 s	
Spin coating	μm range	700	< 60s	Jasinski <i>et al.</i> (2003)
MOCVD Sputtering	500 nm	600–1000	9-80 s	Izu <i>et al.</i> (2004)
wet-chemical precipitation method	–	600-850	> 60s	Chen and Chang (2012)

RF sputtering for oxygen gas sensing applications Gerblinger *et al.* (1995), Izu *et al.* (2004), Ta *et al.* (2008). Further no report is available on the effect of thickness of the CeO₂ film on its structure, composition and gas sensing properties.

To the best of our knowledge, all the reports available in the literature on CeO₂ based oxygen sensors are operated at higher temperatures (>600°C). Also very few reports have revealed their sensitivity values.

The main aim of this thesis is to find the optimum thickness at which we can obtain better sensing performance (sensitivity, fast response and recovery time) and also to reduce the operating temperature at which the gas sensing is performed. This is done in-order to reduce the thermal budget.

Chapter 3

Experimental Details

3.1 Introduction

The process technologies and characterization techniques of the thin films are an integral part in realization of the gas sensing devices. In this chapter, the deposition of CeO₂ thin films by Radio Frequency (RF) Magnetron Sputtering and its characterization is discussed in detail. Also the parameter that needs to be considered in comprehensive characterization of gas sensitive materials are outlined. The objective of characterization is to establish the optimum operating conditions, the reproducibility and reliability of the sensors developed.

3.2 Overview of Deposition Techniques

Rapidly changing needs for the sensing film materials and devices are creating new opportunities for the development of the new processes, materials and technologies. A general classification scheme of thin film deposition is presented in Fig. 3.1.

Thin film deposition technologies grouped accordingly to evaporative methods, glow discharge methods, gas-phase chemical and liquid-phase chemical processes are shown in Table 3.1.

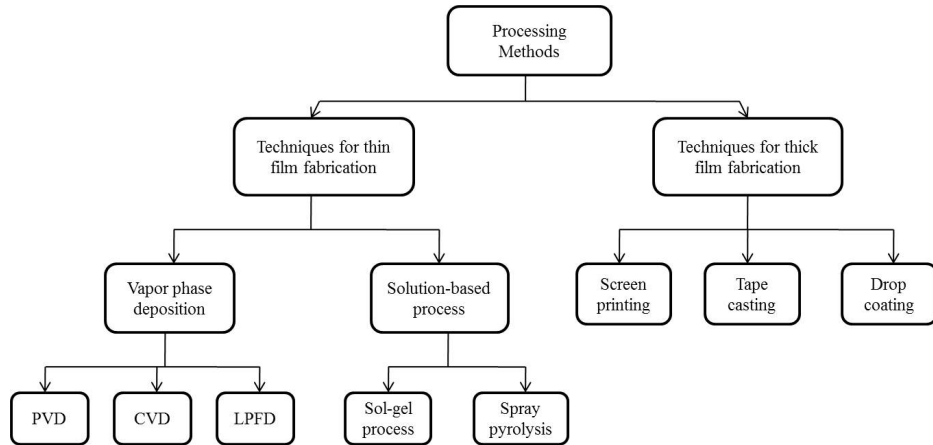


Figure 3.1: Broad classification of film deposition methods

3.3 Physical Vapor Deposition

Physical Vapor Deposition (PVD) is a process by which the thin film of a material is deposited on a substrate according to the following sequence of steps: 1) the material to be deposited is converted into vapor by physical means; 2) the vapor is transported across a region of low pressure from its source to the substrate; and 3) the vapor undergoes condensation on the substrate to form the thin film. In gas sensor fabrication, the primary PVD methods used are Evaporation and Sputtering. The other methods used are pulsed laser deposition, spin casting, RGTO (Rheotaxial Growth and Thermal Oxidation) etc.

3.3.1 Evaporation

Thin films can be deposited through evaporation of the material from a hot source onto a substrate. A sample of material to be deposited is placed in a crucible and the deposition chamber is evacuated to 10^{-6} to 10^{-7} torr. The high-vacuum environment ensures that the vaporized atoms or molecules will be transported to the substrate with minimal collision interference from other gas atoms or molecules. The crucible is then heated using a tungsten filament (resistive evaporation) or with an electron beam (e-beam evaporation). Evaporation can also be achieved by heating the source material with RF energy. This technique employs an RF induction heating coil that surrounds a crucible containing the source. This method of evaporation is known as inductive heating evaporation.

Table 3.1: Classifications of Deposition methods

Classification	Type
Evaporative methods (Vacuum Evaporation)	Conventional Vacuum Evaporation
	Molecular-Beam Epitaxy (MBE)
	Electron Beam Evaporation
	Pulsed Laser Deposition
Glow-Discharge Processes (Sputtering-Plasma Process)	Diode Sputtering
	Reactive Sputtering
	Plasma Oxidation
	Bias Sputtering
	Plasma Anodization
	Magnetron Sputtering
	Ion beam Sputter deposition
	Microwave ECR Plasma
	Gas-Phase chemical process (Chemical Vapour Deposition)
Atmospheric Pressure CVD	
Thermal nitridation	
Low-pressure CVD	
Thermal Polymerization	
Metallo-organic CVD	
Ion implantation	
Laser- Induced CVD (PCVD)	
Electron-enhanced CVD	
Liquid Phase Chemical techniques (Electro Processes- Mechanical Techniques)	Electroplating
	Spray pyrolysis
	Electroless plating
	Spray-on Techniques
	Electrolytic anodization

The advantages of evaporation are: 1) high film deposition rates; 2) less substrate surface damage from impinging atoms as the film is being formed; 3) excellent purity of the film because of the high vacuum condition used by evaporation; 4) less tendency for unintentional substrate heating.

The disadvantages of using evaporation are: 1) more difficult control of film composition than sputtering; 2) absence of capability to do in situ cleaning of substrate surfaces, which is possible in sputter deposition systems; 3) step coverage is more difficult to improve by evaporation than by sputtering; and 4) x-ray damage caused by electron beam evaporation can occur ESEMI (2002).

3.3.2 Sputtering

Sputtering is a mechanism by which atoms are dislodged from the surface of a material as a result of collision with high-energy particles. Thus, PVD by Sputtering is a term used to refer to a Physical Vapor Deposition (PVD) technique wherein atoms or molecules are ejected from a target material by high-energy particle bombardment, so that the ejected atoms or molecules can condense on the substrate as a thin film. Sputtering has become one of the most widely used techniques for depositing various metallic films on wafers including aluminum, aluminum alloys, platinum, gold, Ti, W and tungsten and also various insulating films like CuO, ZnO, SnO₂ etc by either RF or reactive sputtering. Sputtering as a deposition technique may be described as a sequence of these steps:

1. Ions are generated and directed at a target material
2. The ions sputter atoms from the target
3. The sputtered atoms get transported to the substrate through a region of reduced pressure
4. The sputtered atoms condense on the substrate, forming a thin film

Sputtering offers the following advantages over other PVD methods used in sensor fabrication:

- Sputtering can be achieved from large-size targets, simplifying the deposition of thin films with uniform thickness over large wafers.
- Film thickness is easily controlled by fixing the operating parameters and simply by adjusting the deposition time
- Control of the material composition, as well as other film properties such as step coverage and grain structure is more easily accomplished than by deposition through evaporation
- Sputter-cleaning of the substrate in vacuum prior to film deposition can be done
- Device damage from X-rays generated by electron beam evaporation is avoided

Sputtering, however, has the following disadvantages too:

- High capital expenses are required
- The rates of deposition of oxides are relatively low
- Some materials such as organic solids are easily degraded by ionic bombardment
- Sputtering has a greater tendency to introduce impurities in the substrate than deposition by evaporation because the former operates under a lesser vacuum range than the latter

3.3.2.1 Reactive RF Sputtering Principle:

The sputtering system consists of an evacuated chamber, a target (cathode) and a substrate table (anode). The electric field inside a sputtering chamber accelerates electrons which collide with Ar atoms producing Ar^+ ions and more electrons and a characteristic purple/blue plasma. These charge particles are then accelerated by the electric field: the electrons towards the anode and the Ar^+ ions towards the cathode (CeO_2 target) as shown in Fig.3.2. When an ion approaches the target, one of the following may occur:

- It may undergo elastic collision and be reflected.
- It may undergo inelastic collision and be buried into the target.
- It may produce structural rearrangement in the target material.
- The impact may set up a series of collisions between atoms of the target leading to the ejection of one of these targets
- Thus the sputtering process can be likened to a break in a game of “atomic” billiards. The excited ion, representing the cue ball, strikes the atomic array of the target - the neatly arranged pack - scattering them in all directions. Some of these will be ejected in the direction of the original approaching ion i.e. normal to the target surface. It is this ejected particle which is useful for deposition on the surface of the wafer. Hence the sputter process essentially involves knocking an atom or molecule out of the surface of a target. Under the right conditions, the sputtered species will travel through space until it strikes and condenses on the surface of the substrate Stuart (1983), Vossen and Cuomo (1978). When the sputtering is for realizing Nitride or oxide like silicon nitride, Tin oxide, to

maintain stoichiometry, apart from Ar (sputtering gas) nitrogen or oxygen will be passed into the chamber and this process is called reactive RF sputtering. The RF sputtering system allows the deposition of non-conductive materials at a practical rate. In such a system, the RF power alone is capable of generating the plasma and accelerates ions to the target to cause sputtering. This process is illustrated by Fig. 3.2.

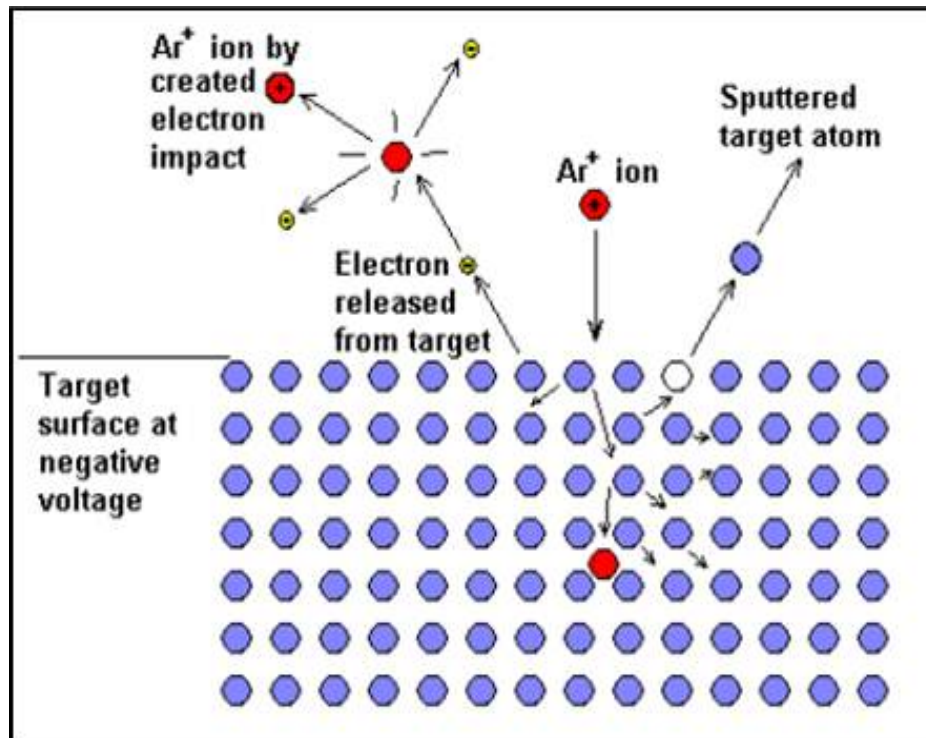


Figure 3.2: Sputtering at the Molecular Level Oxford Vacuum Science Ltd (2000)

3.3.2.2 RF Magnetron Sputtering

In order to increase the performance of RF sputtering, variations on the basic process have been developed Mattox (2010). One of the many variations involves the use of a magnetic field close to the cathode's plane. The use of this variation has certain advantages. It allows an increased sputter rate, higher plasma density, and the ability to sustain plasma at lower pressure, meaning that less gas is needed in the vacuum chamber. In conventional diode sputtering, electrons are created and they escape the effective plasma area near the target. Some fly around the chamber and create

undesirable side effects, such as heating the tooling. A magnetron-sputtering source addresses the electron problem by placing the magnets behind, and sometimes, at the sides of the target. These magnets capture the escaping electrons and confine them to the immediate vicinity of the target. This increases the ion current (density of ionized argon atoms hitting the target) by a factor of 10 over conventional diode targets, resulting in faster deposition rates at lower pressures, which help to produce cleaner films. The secondary electrons generated during the sputter process are trapped by this field and stay close to the cathode surface. Following helical paths as shown in Fig. 3.3 around the magnetic field lines, these electrons are forced to travel longer distances inside the chamber and thus induce more ionizations and finally increase the sputter yield (S) in a significant degree.

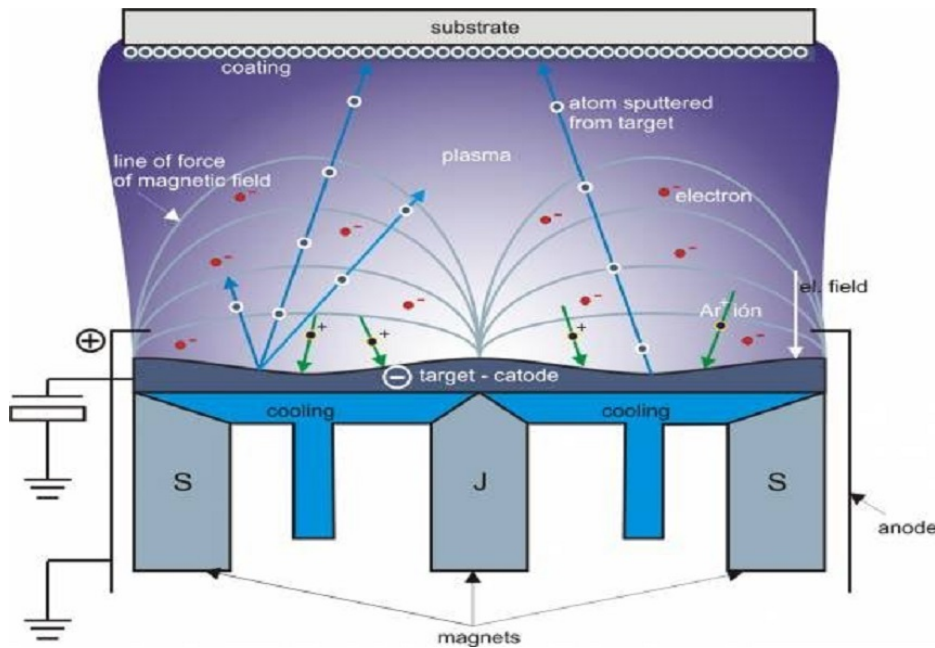


Figure 3.3: Schematic of magnetron sputtering principle Julissa (1994)

3.3.2.3 In house Developed RF Sputtering System

Fig. 3.4 shows the sputtering chamber and the associated RF power supply of the home made RF sputtering unit is shown in Fig 3.5. Both the top and the bottom electrodes are shielded by guard rings. The diameter of the top electrode is 20cm while that of the target electrode is 10 cm and the distance between them is 8cm. The RF generator is operated at 13.56 MHz.

The complete sputter system basically consists of five parts: a RF generator, a matching unit, the deposition chamber, a pumping system, and the gas inlet system. Each part plays a specific role in the sputter process as outlined below.

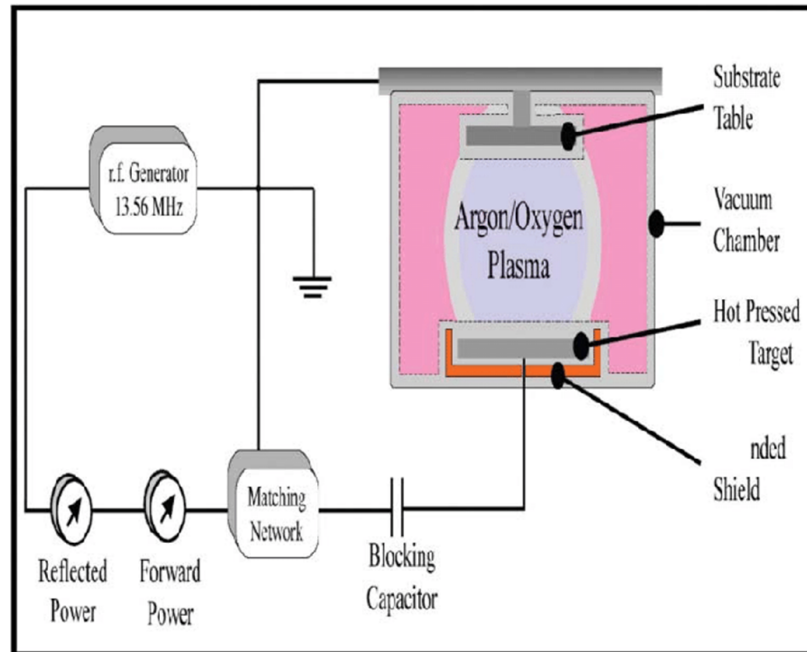


Figure 3.4: Schematic of the RF Sputtering Chamber Bashar (1998)

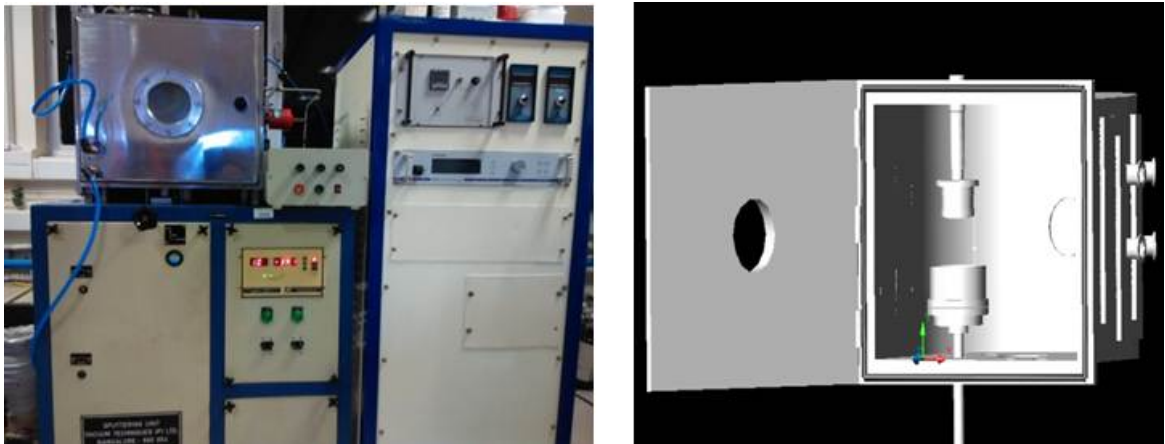


Figure 3.5: (a) Photograph of in-house fabricated RF sputtering unit. (b) Schematic of the sputtering chamber

The material to be sputtered is taken into a target form and mounted onto a circular copper backing plate in the sputter up configuration mode. In this case the

target consists of a circular disk of hot pressed 99.99% purity CeO₂ of 3” diameter and 3 mm thick. During deposition, the sample is inverted and placed into substrate table facing the target. There is a shutter which separates the target and the substrate. It prevents contamination of the target during sample loading-unloading and protects the sample during pre-conditioning. To ensure the uniformity of the deposited films, the substrate holder is kept in rotation by a stepper motor based rotating setup.

Table 3.2: Specifications of in house fabricated RF Sputtering chamber

Item	Description/Specification	Vendor/Model
Chamber	SS made 16” Diameter Semicircular box type	Vacuum Techniques
Pumping system	Turbomolecular Pump Rotary Pump	Pfeiffer
Gauge	Digital Pirani and Penning	Vacuum Techniques
Cathode	3 inch	Kurt J. Lesker
RF Supply	13.56 MHz, 1000 W with matching network	Advanced Energy Dressler Cessar-1310
MFC	Ar = 0-100 sccm O ₂ = 0-50 sccm	Eureka Industries
Substrate heater	RTP-900 ^o C with PID controller	Excel Instruments

3.4 Fabrication of Sensor Film

3.4.1 Sample Preparation

Single crystal Sapphire (Al₂O₃) substrates of a-plane were ultrasonically cleaned using CMOS grade acetone and isopropyl alcohol, each for 5 minutes to remove the organic contaminants. The wafers were thoroughly rinsed with deionized water between each step. Finally, the substrate is dried by blowing high purity nitrogen gas which removes the residual water droplets from the substrate.

3.4.2 Deposition of CeO₂ films by RF Sputtering Technique

The CeO₂ thin film depositions were carried out in an in-house fabricated RF magnetron sputtering system (shown in Fig. 3.5). The chamber was evacuated to a base

pressure of 2×10^{-6} mbar using a rotary and turbo molecular pumping combination. 99.99% pure CeO_2 target of 3 mm thickness with 3 inch diameter was used as a sputtering target. The cleaned Al_2O_3 substrates of $1\text{cm} \times 1\text{cm}$ size were loaded into the chamber. To ensure the uniformity of thickness and composition of the films, the substrate is subjected to rotation with a stepper motor arrangement. High purity argon and oxygen gas were admitted into the chamber and the operating pressure of 2×10^{-3} mbar was maintained. The target was pre-sputtered (shutter in-between the substrate and the target kept in the closed position) for 10 minutes at 25 Watts. The power was gradually increased in steps of 10 Watts for every 3-4 minutes. Finally on reaching 75 Watts, the shutter was opened and the film deposition was started. The duration of deposition was varied between 80-315 minutes. After sputtering, shutter was closed and the power was gradually reduced in steps of 15 Watts. This was done in order to prevent the sputtering target from thermal shock which may lead to development of cracks. The range of each deposition parameters whose influences are studied in the experiments is given in Table 3.3

Table 3.3: Sputtering parameters of Cerium Oxide

RF Power	75 Watts
Base pressure	1.5×10^{-6} mbar
Working pressure	5.0×10^{-3} mbar
Ar : O_2	22 : 2 sccm
Deposition Time	80 - 315 mins
Deposition Temperature	RTP to 400°C
Target to Substrate Distance	8.0 cm
Target	CeO_2 (99.99%), 3mm thick and 3" diameter
Pre sputtering time	15 mins
Annealing temperature	100-500 $^\circ\text{C}$
Annealing Duration	2 Hours

3.4.3 Deposition of Mixed Oxides ($\text{CeO}_2\text{-HfO}_2$) films by RF Sputtering Technique

$\text{CeO}_2\text{-HfO}_2$ mixed oxide films were deposited on Single crystal Sapphire substrates of a-plane at a fixed substrate temperature of 400°C by reactive RF magnetron sputtering. The substrates ($1\text{cm} \times 1\text{cm}$ pieces) were kept on the substrate holder and this

holder is rotated above the target to ensure the uniformity of thickness and composition of the films. HfO_2 films were mixed with CeO_2 by placing small HfO_2 chips of 1 mm thick on the cerium oxide target at various positions. The HfO_2 wt % in this process was changed by changing the number (between 2-4), size (from $5\text{mm} \times 5\text{mm}$, $4\text{mm} \times 4\text{mm}$, $3\text{mm} \times 3\text{mm}$, $2\text{mm} \times 2\text{mm}$ and $1\text{mm} \times 1\text{mm}$) and position of HfO_2 chips. The process can be treated as co-sputtering but the difference is that the hafnia chips are kept on the cerium oxide target itself and a single RF power source is used for sputtering. This method suited for our requirement as the HfO_2 content in the Cerium oxide films is very small.

The different arrangements of HfO_2 chips on the CeO_2 target are given in Fig. 3.6. Variation in the fashion and also the number of chips gives an additional deposition process parameter.

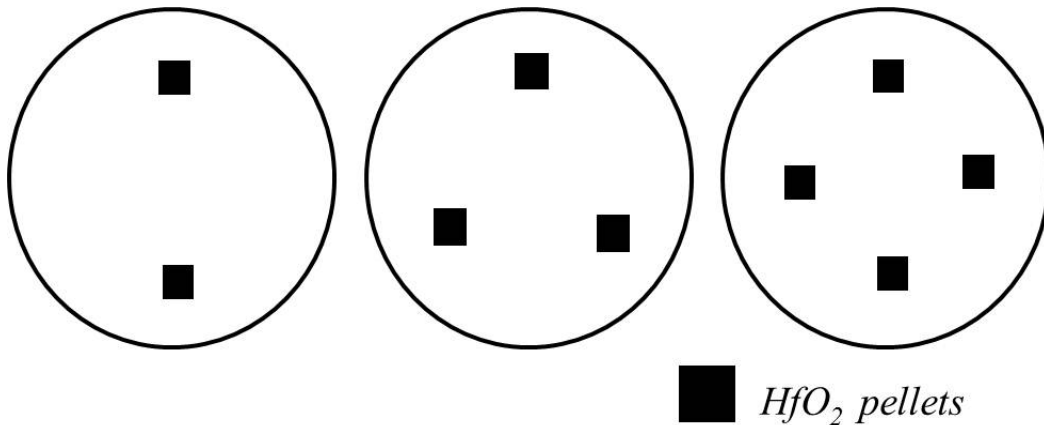


Figure 3.6: Arrangement of HfO_2 chips on the 3" Cerium Oxide target

The films deposited under different processing conditions are characterized for their composition by XRD, XPS, AFM, TEM and by other characterization methods which have been detailed in following section.

3.5 Characterization Techniques

The films deposited by RF Sputtering were characterized for their thickness, structure and composition. Primary characterization techniques for characterizing CeO_2 films: Thickness measurement techniques like Spectroscopic Ellipsometry and Cross-sectional SEM, composition and chemical information such as oxidation states and sur-

Table 3.4: Sputtering parameters for deposition of mixed oxides (CeO₂ + HfO₂ films)

Technique	RF Sputtering
Target	CeO ₂ (99.99%), 3mm thick and 3" diameter
No. of Pd chips	2- 4 each of size 5mm × 5mm × 1mm
Ar : O ₂	22 : 2 sccm
Base pressure	1.5 x 10 ⁻⁶ mbar
Working pressure	5.0 x 10 ⁻³ mbar
Pre sputtering time	15 mins
RF Power	75 Watts
Target to Substrate Distance	8.0 cm
Deposition Temperature	RTP to 400°C
Annealing temperature	100-500 °C
Annealing Duration	2 Hours

face composition using - X-ray Photoelectron Spectroscopy (XPS), structural characterization- X-ray diffraction and determination of surface roughness – Atomic Force Microscopy (AFM) were carried out.

3.5.1 Thickness measurement techniques

Thickness gives the rate of deposition and is also important in determining the thin film material properties. Hence in any thin film deposition the thickness measurement is very important, especially Micro and Nano electronic applications generally require the precise and reproducible film metrology, i.e. thickness as well as lateral dimensions.

3.5.1.1 Spectroscopic Ellipsometry

Spectroscopic ellipsometry is a versatile and powerful optical technique for the investigation of the optical properties of the materials. Thicknesses and optical constants such as refractive index and extinction coefficient of thin films can be measured by measuring amplitude and phase change information across the wavelength spectrum. The advantages of ellipsometry are its non-contact, non-destructive character, its high sensitivity due to the measurement of the phase change of the reflected light (less sensitive to the fluctuations of light intensity), and its large measurement range (from fractions of single layers to micrometers). It does not require any standards or reference and could be used for real time monitoring of etching and thin film deposition processes.

The basic principle of ellipsometer depend upon the fact that linearly polarized incident light has reflection coefficients which depend on the direction of polarization. The two polarization directions of interest are the E_p or TM (electric field parallel to the plane of incidence) and the E_s or TE (electric field perpendicular to the plane of incidence). Linearly polarized light is decomposed into the p and s components as shown in Fig. 3.7

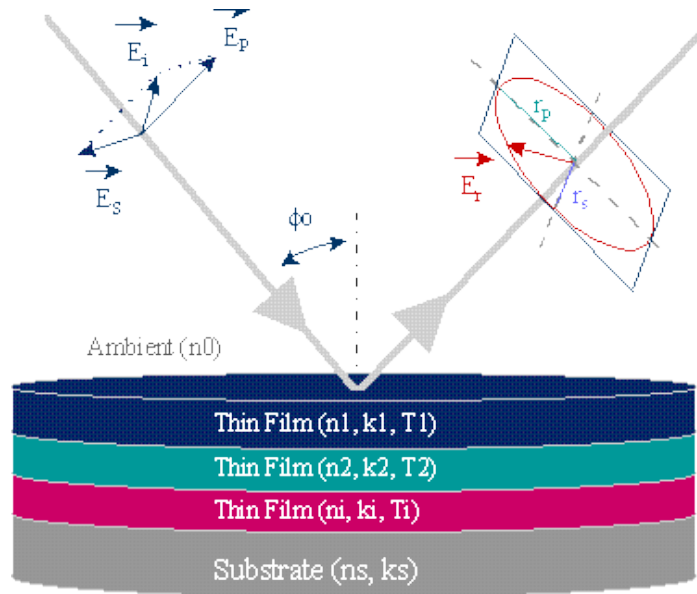


Figure 3.7: Spectroscopic Ellipsometry measurements

These component waves experience different amplitude attenuations, and different absolute phase shifts upon reflection; hence, the state of polarization is changed. Ellipsometry refers to the measurement of the state of polarization before and after reflection for the purpose of studying the properties of the reflecting boundary and also finding the thickness of the films Jung (2004) and Irene (1993).

In the present study, the films were characterized using a VASE spectroscopic ellipsometer (SE) M-2000 (J.A. Woolam Co., Inc., USA) in the spectral range 200-1000nm, the SE data was acquired and analyzed using WVASE software supplied with the ellipsometer Tompkins (2006) Woollam *et al.* (1999). The SE data were fitted to a 3-layer model including surface roughness, the bulk oxide film with simple Gaussian oscillator, and the silicon substrate, where the surface roughness was modeled using a 50% air and 50% bulk oxide Bruggeman effective medium Aspnes *et al.* (1979). SE provides film thickness, effective surface roughness, refractive index and extinction

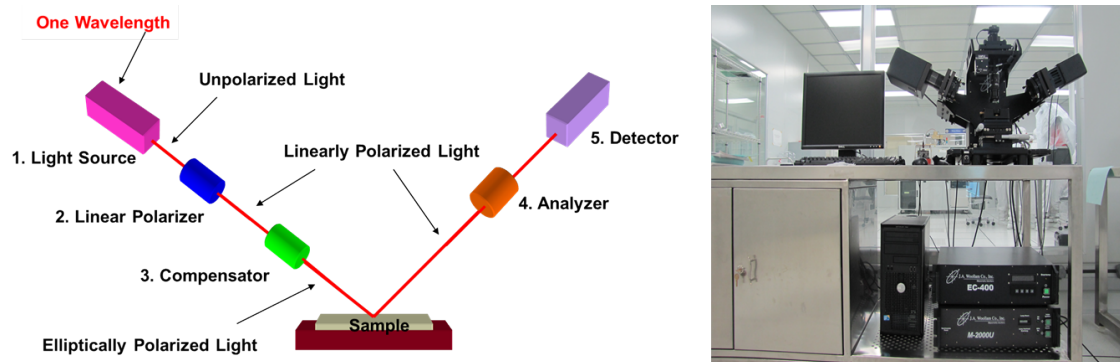


Figure 3.8: Schematic diagram and picture of Ellipsometry equipment Woollam Spectroscopic Ellipsometer (M-2000)

coefficient. The relative error in thickness determination is below 1%, while the relative error in refractive index determination is below 3%.

3.5.1.2 Scanning Electron Microscopy (SEM)

Scanning Electron Microscopy (SEM) is a method for high-resolution imaging of surfaces. The SEM uses electrons for imaging, much as a light microscope uses visible light. The advantage of SEM over light microscope includes greater magnification and much greater depth of field.

An incident electron beam raster scanned across the sample surface and resulting electrons emitted from the sample are collected to form an image of the surface. Imaging is typically obtained using secondary electrons for best resolution of fine surface topographical features. Alternatively, imaging with back-scattered electrons gives contrast based on atomic number to resolve microscopic composition variation, as well as topographical information. Qualitative and quantitative chemical analysis information is also obtained using an energy dispersive x-ray spectrometer with SEM.

In this study, Zeiss Ultra 55 (FESEM) for cross-sectional imaging as well as morphology study was used. The combination of Schottky type field emission source and the through-lens detection technology constitutes the basis for the ultra-high resolution. The high resolution EDX attachment allowed simultaneous chemical analysis.

3.5.1.3 Atomic Force Microscopy (AFM)

Atomic force microscopy has been used for the topographic mapping of the thin film surfaces. In AFM, a probe tip is mounted on a cantilever, which is used for scanning



Figure 3.9: ULTRA 55 - Ultra high resolution scanning electron imaging coupled with material spectroscopy tools

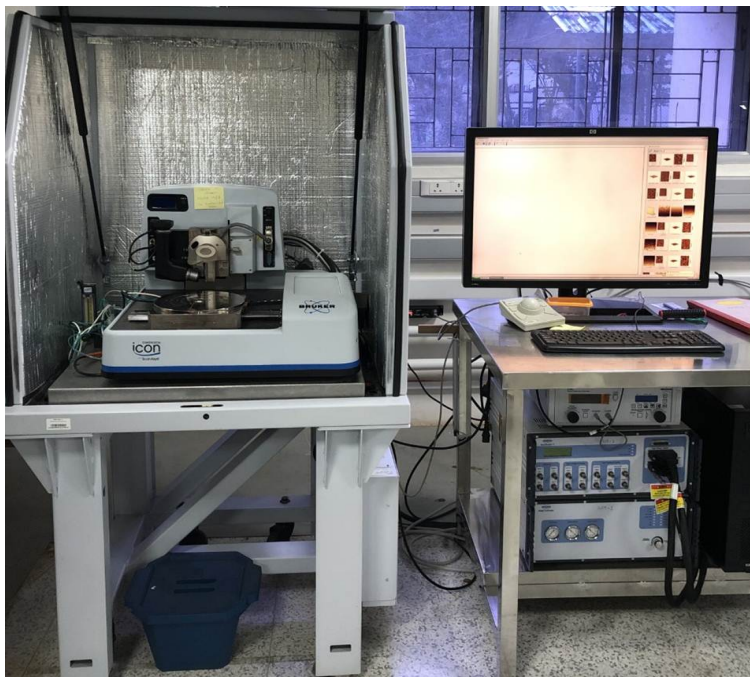


Figure 3.10: Bruker AFM instrument

the surface of the thin film samples. The force of interaction between the sample and the tip after approaching each other causes the cantilever to deflect according to well-

known Hooke's law. The deflections can be sensed with high sensitivity by optical detection method.

There are certain advantages in using the AFM for the surface topographical mapping over the other imaging techniques such as STM and TEM. AFM scanning could be performed even on the insulating substrates whereas STM imaging could be done only on the conducting surfaces. TEM requires a careful sample preparation technique but for AFM scanning there is no such requirements. AFM studies give surface defects, dislocations, terraces and steps in the nano layer systems Wiesendanger and Roland (1994). In this work, Bruker AFM instrument (Model : Dimension ICON) has been used.

3.5.1.4 X-ray Diffraction (XRD)

One of the phenomena of interaction of X-rays with crystalline matter is its diffraction, produced by the reticular planes that form the atoms of the crystal Klug *et al.* (1962), Warren (1990) and Reynolds (1989). A crystal diffracts an X-ray beam passing through it to produce beams at specific angles depending on the X-ray wavelength, the crystal orientation and the structure of the crystal. In the macroscopic version of X-ray diffraction, a certain wavelength of radiation will constructively interfere when partially reflected between surfaces (i.e., the atomic planes) that produce a path difference equal to an integral number of wavelengths. This condition is described by the Bragg's law Barrett *et al.* (1980):

$$2d \sin \theta = n\lambda \quad (3.1)$$

Where n is an integer, λ is the wavelength of the radiation, d is the spacing between surfaces and θ is the angle between the radiation and the surfaces. This relation demonstrates that interference effects are observable only when radiation interacts with physical dimensions that are approximately the same size as the wavelength of the radiation. Since the distances between atoms or ions are in the order of 1\AA , diffraction methods require radiation in the X-ray region of the electromagnetic spectrum, or beams of electrons or neutrons with similar wavelength. So, through X-ray spectra one can identify and analyze any crystalline matter. Crystal structure of the sample can be identified by analyzing the diffraction peaks of the sample and comparing with the diffraction patterns data base (JCPDS data).

X-ray diffraction patterns were recorded using a Rigaku smartlab diffractometer with Cu $K\alpha$ radiation. All the diffraction patterns were obtained in GIXRD mode by varying 2θ from 10° - 90° in a continuous scan mode with the scan step of 0.010. Incident angle (ω) was kept at 0.30 to avoid the intensity contribution from the substrate.



Figure 3.11: Rigaku SmartLab High Resolution X-ray Diffractometer system.

3.5.1.5 X-ray Photoelectron Spectroscopy (XPS)

X-ray photoelectron spectroscopy, also known as electron spectroscopy for chemical analysis (ESCA), is a powerful surface-sensitive technique for the determination of chemical composition of materials. It is accomplished by irradiating a sample with X-rays for the excitation of the material and energy analyzing of emitted photoelectrons. The source used for the soft X-rays are generally $MgK\alpha$ (1253.6 eV) or $AlK\alpha$ (1486.6 eV). Depending on the matrix of atoms in structure of materials, incident X-rays can travel in solids from 1 to 10 nm.

The emitted photoelectrons overcome the binding energy, E_b , of certain energy state and have a kinetic energy, E_k . The binding energy is measured by analyzing the resultant kinetic energy of photoelectrons and the number of electrons that escape from the surface of materials. Comparing the binding energies of materials with

energy database, the types of elements, the chemical state and their concentration on the surface can be identified. The relation of the process can be written as:

$$E_b = hv - E_k - \phi \quad (3.2)$$

where, ϕ is the work function of the material. It is defined as the potential difference between the Fermi level of the sample and the vacuum level.

Since for each element there is a characteristic binding energy of an electron associated with specific atomic orbital (s, p, d, f, etc.), by using the XPS measurement one can identify the elements present in the material. The concentration of them can also be measured since the intensity of the photoelectron lines is taken as the measure of this quantity. Due to the Coulombic interaction between electron and its surrounding there is an important effect of atomic environment on binding energy of an electron. This interaction results in shifting in binding energy of electrons and give rises to the identification of bonds on an atom constructing with surrounding atoms and subsequently revealing the compounds present in the structure Watts and Wolstenholme (2003).

For the non-conducting materials, a positive charge is built up in the sample surface following to the ejection of electrons from the specimen under X-ray irradiation and results in lowering the kinetic energy of liberated electrons due to the coulombic interaction taking place between surface charge and electrons. To eliminate the effect of surface charging on shifting binding or kinetic energy, the correction is done based on the calibration of the binding energies with known reference binding energy of photoelectron line (in general, C 1s (284.6 eV)).

The identification of chemical states of determined element is accomplished by comparing the calculated binding energies of each component with reported state values by taking the chemical shift into account. Furthermore, the relative amount of present phases in specimen is revealed from the relative area under each component state. So, following all these complex analyzing stages, XPS measurement can reveal important surface properties of a material like the identification of elements present at the surface, chemical state of elements, quantity of chemical state of each element, spatial distribution of the material in 3-D, and concentration of element present in the material Watts and Wolstenholme (2003).

XPS analysis of the films was performed with Axis Ultra from Kratos. The resid-

ual pressure inside the analysis chamber was 1.0×10^{-10} mbar. The spectrometer was calibrated using photoemission lines of Ag (Ag $3d_{3/2} = 367$ eV with reference to Fermi level). The photoelectrons were excited with an Mg $K\alpha$ (1253.6eV) x-ray source operating at 100W power. Survey spectra was collected using pass energy 40 eV and high resolution spectra of the elements were collected using pass energy of 20 eV with step size of 0.1eV. The film surface was sputtered by Ar^+ ions having energy of 5 KeV with a current of $30 \mu A$ for 3 min to obtain the depth profiles. Charging effects were corrected by setting the C1s peak for adventitious carbon at 284.6eV for the surface and by flood gun after Ar^+ ion etching and shifting the entire spectrum correspondingly. Shirley background correction and 30% Gaussian and 70% Lorentzian peak fitting was used. The recorded spectrum was calibrated by using the binding energy of carbon (C1s, 284.6eV). XPS signals were analyzed by CASA XPS software.



Figure 3.12: Multi-technique X-ray Photoelectron Spectroscopy with XPS-mapping capability

3.5.1.6 Electron Probe Micro Analyzer (EPMA)

The Electron Probe Micro Analyzer (EPMA) is used for identification of constituent elements in the specimen and study their distribution as well as for morphological observation. Analyses are performed by illuminating the specimen surface with a finely focussed electron beam and measuring the wavelengths and intensities of characteristic electrons from it.

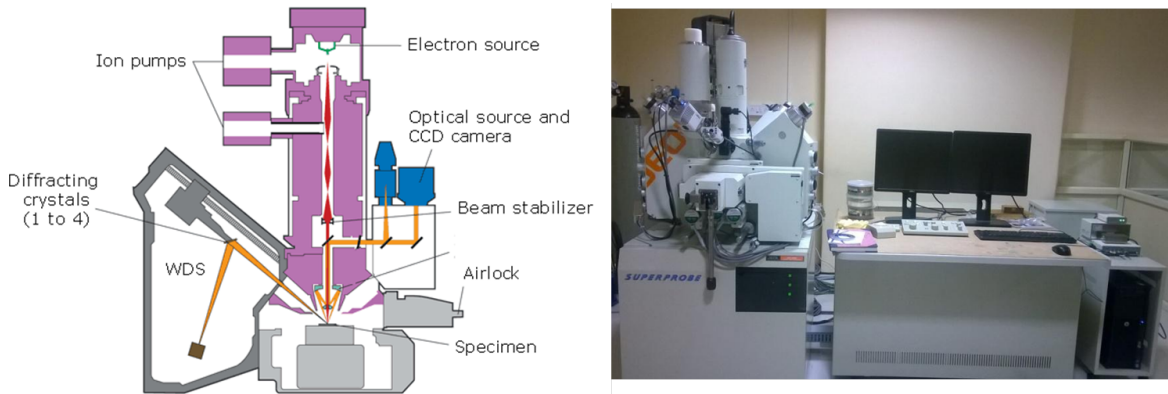


Figure 3.13: Schematic of EPMA and Picture of EPMA Tool (Model : JEOL JXA-8530F)

EPMA works by bombarding a micro-volume of a sample with a focused electron beam (typical energy = 5-30 keV) and collecting the X-ray photons thereby emitted by the various elemental species. Because the wavelengths of these X-rays are characteristic of the emitting species, the sample composition can be easily identified by recording WDS spectra (Wavelength Dispersive Spectroscopy). WDS spectrometers operate based on Bragg's law and use various moveable, shaped monocrystals as monochromators Science Education Resource Center (2019).

- EPMA is a fully qualitative and quantitative method of non-destructive elemental analysis of micron-sized volumes at the surface of materials, with sensitivity at the level of ppm. Routine quantification to 1% reproducibility is obtained over several days. It is the most precise and accurate micro-analysis technique available and all elements from B to U and above can be analyzed
- EPMA is fully compatible with routine analysis sessions, with easy and direct interpretation of the results

- EPMA instruments are equipped with a complete kit of built-in microscopy tools that allow simultaneous X-ray (WDS and EDS), SEM and BSE imaging, plus sophisticated visible light optics; they provide very flexible sample inspection with image magnification ranging from 40 to 400,000
- Determination of thickness and elemental composition from nm to mm thick layers in stratified materials is possible

EPMA provides much better results than standard SEM/EDS systems. Because of the internal properties of WDS, the general sensitivity, analysis of light elements and risks of erroneous interpretation of qualitative spectra are all superior with EPMA. Spectral resolution and detector dead time are much better than EDS (Energy Dispersive Spectroscopy). The excitation beam regulation system and sophisticated sample stage capabilities guarantee that this technique provides outstanding stability and measurement repeatability CAMECA (2017).

3.6 Fabrication of Electrodes or Contacts

Aluminum electrodes of thickness 100nm (to measure the conductivity changes) were deposited using Thermal Evaporation Technique. The locally fabricated standard mask was kept underneath the substrate for proper patterning of electrodes. Fig. 3.14 shows the schematic cross section of the basic oxygen sensor.

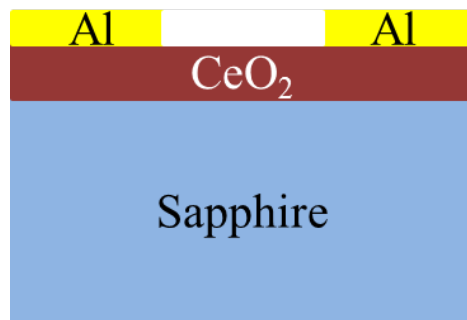


Figure 3.14: Schematic of oxygen sensor

3.7 Gas Sensing Measurements

For gas sensing test, the sensor device called as chemiresistor and measurement system were designed using the concept of resistance variation in the sensing materials after the target gas exposure. The gas sensing behavior of chemiresistor sensors was studied by calculating the change in the surface resistance of sensing film with time towards the exposure of the target gas (step by step varying the concentration) with a fixed temperature. The resistance variation was measured by Keithley source meter (SMU 2405). The chemiresistor type sensors were mounted on the hot plate (If it is an integrated gas sensor, microheater will be incorporated with the gas sensing film itself.) which was coupled with ceramic base stand. The film placed above the heater is connected to two probes which are further connected in series with a Programmable D.C. Power Supply and Keithley High-Voltage Source-Measure Unit. Finally this sensor setup was fixed into the homemade gas sensing chamber. The electrical connections for gas sensing measurements, thermocouple and temperature variation were made using instrumentation feed through.

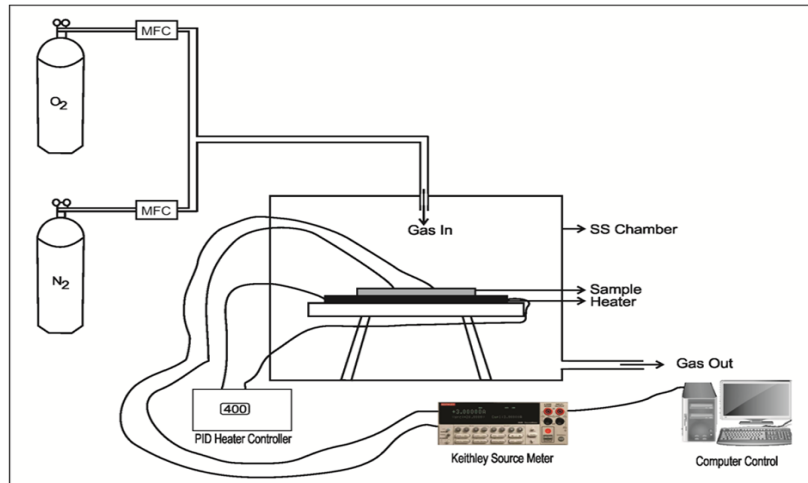


Figure 3.15: Schematic block diagram of gas sensing setup used

The schematic block diagram of gas sensor setup is shown in Fig. 3.15 and the in house fabricated gas sensing setup is shown in fig 3.16.

During the sensing measurement, the sensor was exposed to pure N₂ until the constant baseline resistance was achieved and then the gas analyte (O₂ in this case) was introduced in the chamber and the resistance of the sensor was recorded. During this time the steady resistance had been achieved, and then the sensing chamber was



Figure 3.16: Gas sensor setup used for O₂ sensitivity measurement

flushed with pure N₂ consecutively to allow the surface of the sensitive film to regain atmospheric condition and the resistance of it reached steady and kept stable. The response of sensor was monitored in terms of the normalized resistance calculated by Response (R_g/R_o) and the sensitivity factor was monitored. R_g is the resistance of the sensor in the presence of analyte gas and R_o is the initial baseline resistance of the films.

Once the resistance changes are noted down in the gas sensing experiments, to get the sensitivity analysis the sensitivity response curves had been drawn based on the schematic shown in Fig. 3.17

3.7.1 Thermal Characterization of Microheaters

To capture the thermal image, the microheater is placed on the test bench and the electrodes are connected to the Keithley source meter 2410C and current or voltage is given as input in regular step. When the heater temperature is raised, the thermal image is captured by the FLIR camera. The detector used in this camera is InSb and the lens used is G5. The scanned spectrum range is 1.5-5.1 μm and the temperature range is from -20°C to 3000°C. During this process the emissivity of the Platinum is kept at 0.1. The inbuilt software program [ALTAIR] enabled us to directly read the real-time temperature of the microheater.

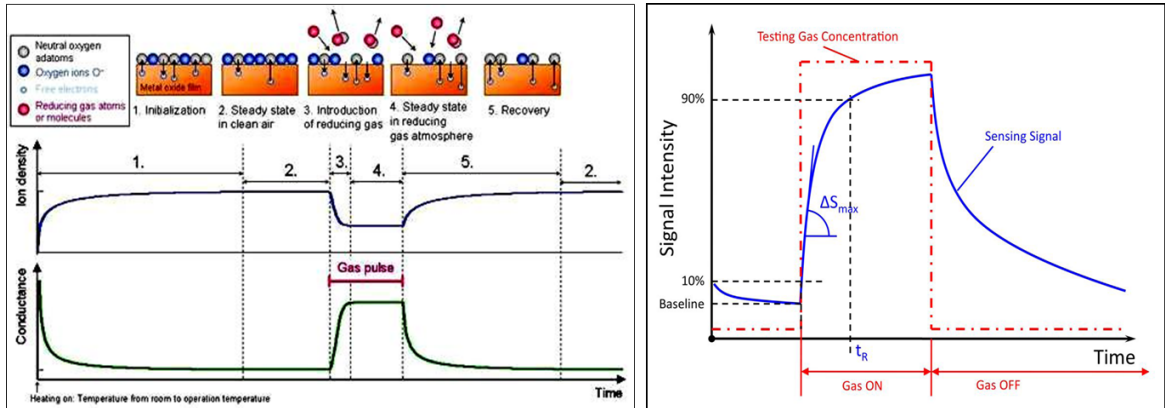


Figure 3.17: a) Schematic response curve of gas sensor testing. The typical characteristic values extracted from the measurement are identified on the plots b) schematic of a typical response curve of gas sensor testing

Parameters adjustable in the infra red camera are: emissivity, background temperature, windows size and integration time; each one of them is very important for thermal imaging. The temperature of the heater element was measured using a IR camera from FLIR (Model: SC5200). The thermal imaging camera can convert the IR radiant energy received by the detector into an electrical signal point by point in the view area, the analog signals are then amplified, modified and converted into digital signal and displayed in the monitor as a thermal image. This system is capable of recording 50 images per second allowing the dynamics of the system to be analyzed.

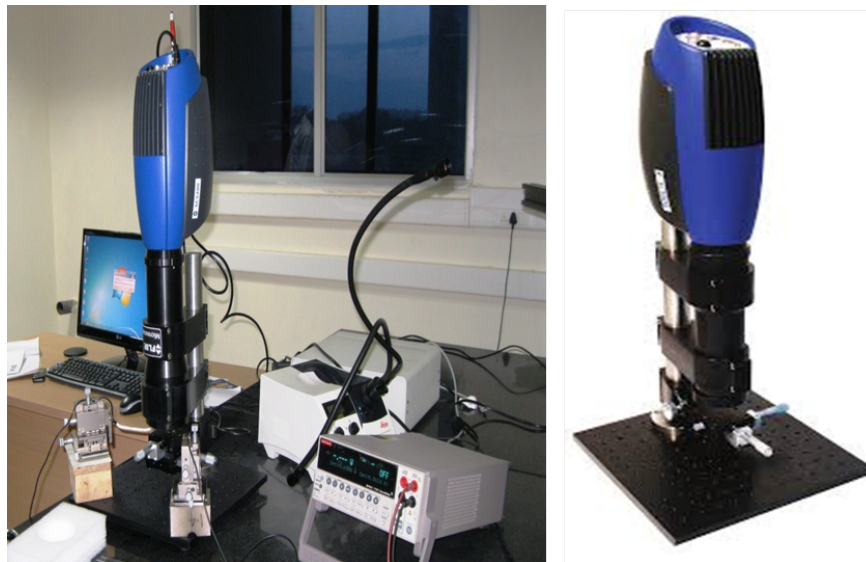


Figure 3.18: FLIR SC 5200 IR Camera Setup

Chapter 4

RF Sputtered CeO₂ Thin Films Based Oxygen Sensors

4.1 Introduction

CeO₂ is a potential candidate material for oxygen gas sensor applications due to their excellent properties such as good ionic and electronic conductivity, high chemical and thermodynamic stability, high thermal shock resistance and good dielectric properties. Also, CeO₂ exhibits a unique property of co-existence of trivalent (Ce^{+3}) and tetravalent (Ce^{+4}) states of Ce atom and they transform easily from one to another. To the best of our knowledge, all the reports available in the literature on CeO₂ based oxygen sensors operates at higher temperatures ($>600^{\circ}C$), are developed by chemical methods and the thickness of the sensing film (CeO₂) is in the range of μm to mm. Very few reports are available on the synthesis of CeO₂ films using RF sputtering for oxygen gas sensing applications. However, no systematic work has been carried out on the effect of CeO₂ film thickness on oxygen sensing characteristics.

This chapter discusses the development of relatively low operating temperature CeO₂ thin film based oxygen gas sensors using RF sputtering by optimizing the process parameters and thickness (~ 260 nm). The sensor performance was understood and evaluated by using electrical, compositional, structural and morphological data of CeO₂ films. The developed CeO₂ based oxygen sensors are CMOS compatible, scalable and show high sensitivity, fast response, and operates at relatively low temperature ($400^{\circ}C$).

4.2 Sensor Fabrication

Single crystal Sapphire (Al_2O_3) substrates of a-plane were ultrasonically cleaned using CMOS grade acetone and isopropyl alcohol, each for 5 minutes to remove the organic contaminants. The wafers were thoroughly rinsed with deionized water between each step. Finally, the substrate is dried by blowing high purity nitrogen gas which removes the residual water droplets from the substrate.

The CeO_2 thin film depositions were carried out in an in-house fabricated RF magnetron sputtering system. The chamber was evacuated to a base pressure of 2×10^{-6} mbar using a rotary and turbo molecular pumping combination. 99.99% pure CeO_2 target of 3 mm thickness with 3 inch diameter was used as a sputtering target. The cleaned Al_2O_3 substrates of 1cm x 1cm size were loaded into the chamber. The distance between the substrate and target was 8.0 cm. To ensure the thickness and composition uniformity of the films, the substrate is subjected to rotation with a stepper motor arrangement. High purity argon and oxygen gas were admitted into the chamber at 25 and 2 sccm respectively and the operating pressure of 2×10^{-3} mbar was maintained. The target was pre-sputtered (shutter in-between the substrate and the target kept in the closed position) for 10 minutes at 25 Watts. The power was gradually increased in steps of 10 Watts for every 3-4 minutes. Finally on reaching 75 Watts, the shutter was opened and the sputtering was started. The duration of deposition was varied between 80-315 minutes. Similarly, after sputtering, the power was gradually reduced in steps of 15 Watts. This was done in order to prevent the sputtering target from thermal shock which may lead to development of cracks. The substrate temperature during deposition was $400^\circ C$ and post deposition, annealing was done for 2 hours at $500^\circ C$. The process parameters used in this work are listed below in Table 4.1.

The deposited CeO_2 films were characterized by using Ellipsometry for determining the thickness and X-ray diffraction (Rigaku SmartLab system) for phase identification and structural analysis. X-ray photoelectron spectroscopy (AXIS Ultra DLD) was employed to determine the chemical composition and core level binding energies. The photoelectrons were excited with a monochromatic Al $K\alpha$ (1486.3eV) X-ray source operating at 117 W power. Survey spectra were collected using pass energy 160 eV and high-resolution spectra of the elements (Ce-3d, O-1s, and C-1s) were collected using pass energy of 20 eV with a step size of 0.1eV. Charging effects were corrected by

Table 4.1: Sputtering parameters used for deposition of CeO₂

Technique	RF sputtering
Target	CeO ₂ (99.99%)
Argon	25 sccm
Oxygen	2 sccm
Sputtering gas pressure	2.5 x 10 ⁻³ mbar
Power	75 W
Substrate to target distance	8.0 cm
Substrate temperature	400°C
Annealing temperature	500°C
Annealing duration	2 Hours

setting the C1s peak for adventitious carbon at 284.6eV for the surface and shifting the entire spectrum correspondingly. Shirley background correction, 30% Gaussian and 70% Lorentzian peak fitting were used.

Aluminum electrodes of thickness 100nm (to measure the conductivity changes) were deposited using Thermal Evaporation Technique. The locally fabricated standard mask was kept underneath the substrate for proper patterning of electrodes.

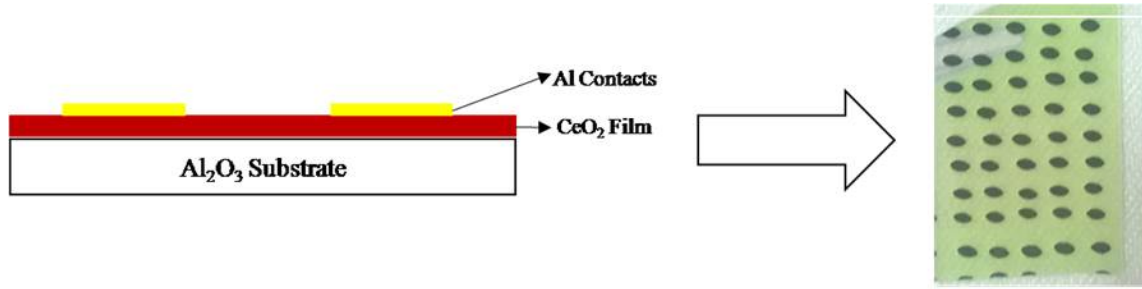


Figure 4.1: Schematic and photographic image of the fabricated sensor

4.3 Results and Discussion

Here the characterization of CeO₂ films which includes thickness, structural, compositional/chemical, and surface morphology properties is presented. Finally, the gas sensing results are discussed.

4.3.1 Physical properties

CeO₂ thin films of different thicknesses have been deposited on Al₂O₃ substrates by varying the deposition time from 80-315 minutes and keeping all other process parameters constant. The thickness of the films has been measured using Ellipsometry and is validated using cross-sectional SEM and Dektak surface profilometer. The measured thickness of the films is in the range of 90-340 nm and varies linearly with the deposition time at constant power. The refractive index of the films is in the range of 2.38 to 2.42 which is in agreement with the reported literature values Singh and Srivatsa (2016). The thickness of the films was measured using ellipsometry. Fig. 4.2 shows the variation of thickness with deposition time at constant power. The rate of deposition was found to be around 1.08nm per minute. It clearly shows that the thickness varies linearly with time at constant power. Fig. 4.3 shows the cross-sectional SEM images of the film deposited for 200 and 240 mins and the measured thickness is respectively around 220 nm ± 10 nm and 250 nm ± 10 nm, which is in good agreement with the ellipsometry data.

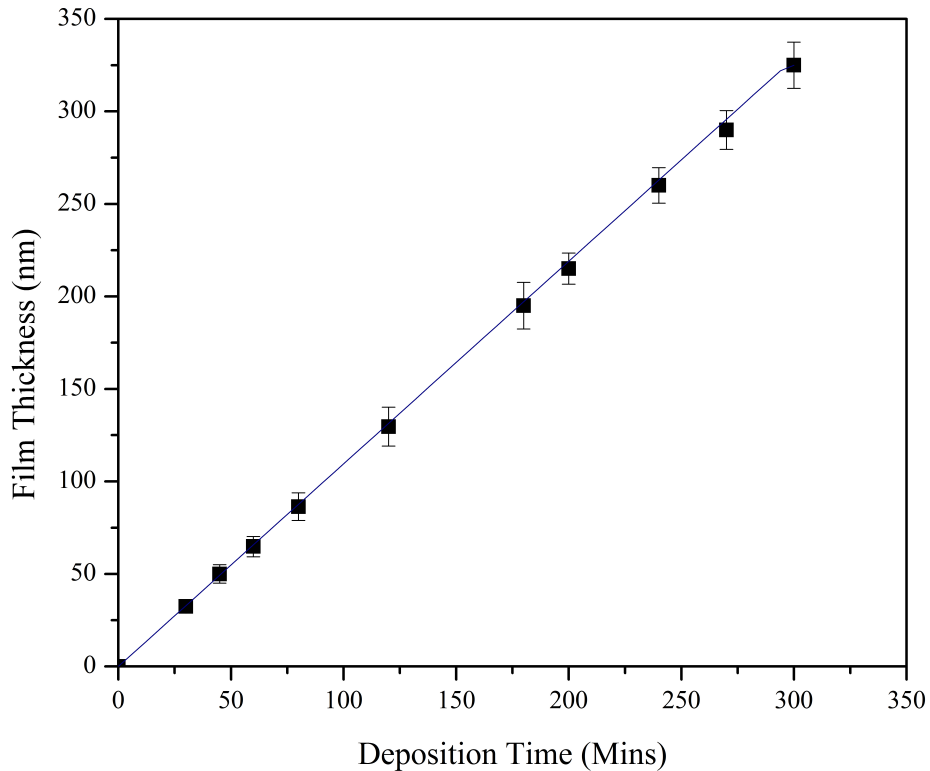


Figure 4.2: Variation of thickness with deposition time

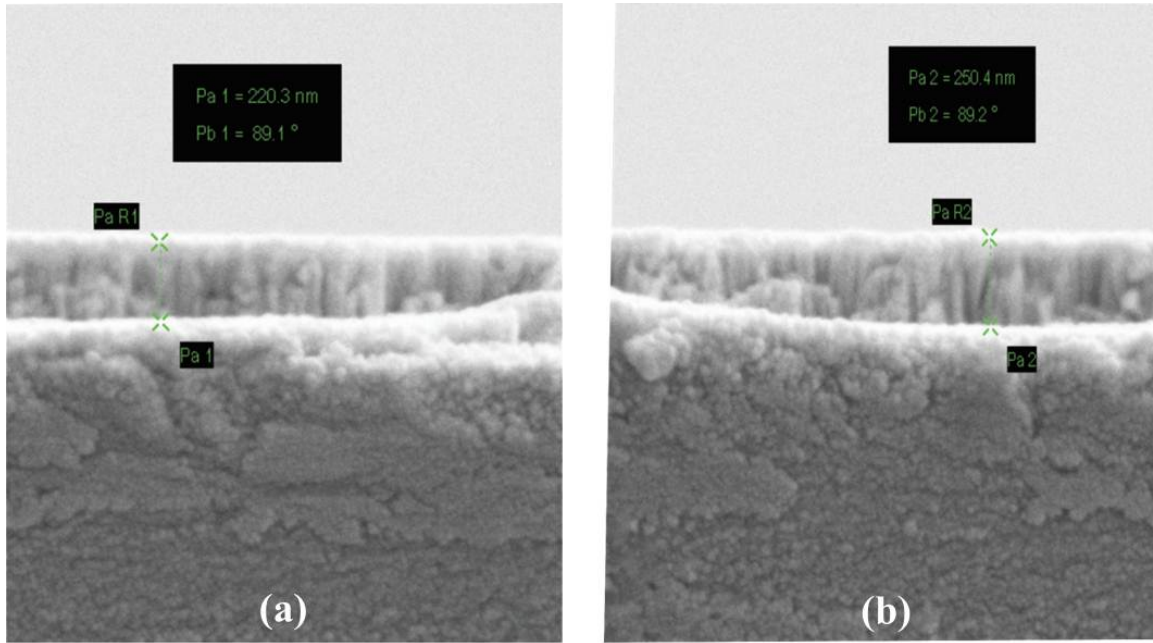


Figure 4.3: Cross-sectional SEM images of the CeO_2 film deposited for (a) 200 minutes and (b) 240 minutes

4.3.2 Compositional properties

The elemental composition of the deposited CeO_2 thin films was calculated from the XPS wide or survey spectra (shown in Fig. 4.4). It clearly indicated that the deposited films were pure (single phase) in nature. In other words, no other impurity peaks were observed except Ce and O.

Fig. 4.5 shows the high resolution XPS spectra (Ce-3d level) of CeO_2 films for different thickness. The Ce-3d level has a complex structure due to the strong hybridization of Ce-4f and O-2p states in Cerium oxide. The ratio of O/Ce atomic concentrations were extracted by using relative sensitivity factors (RSF) of the individual elements. It was found that the O/Ce ratio has increased from 1.4 ± 0.1 to 2 ± 0.1 with increase in thickness from 90 nm to 195 nm and then became saturated at 2 ± 0.1 for higher thicknesses (≥ 195 nm). This indicates that the thicker films, ≥ 195 nm appear to be stoichiometric (CeO_2). Manorama *et al.* (2003) reported that the CeO_{2-x} ($1.5 < x < 2$) is an n-type semiconducting oxide with fluorite structure which is suitable for oxygen gas sensing. However, the sensing also depends on the other factors such as structure, grain size, surface energy, and diffusion coefficient of the sensing materials.

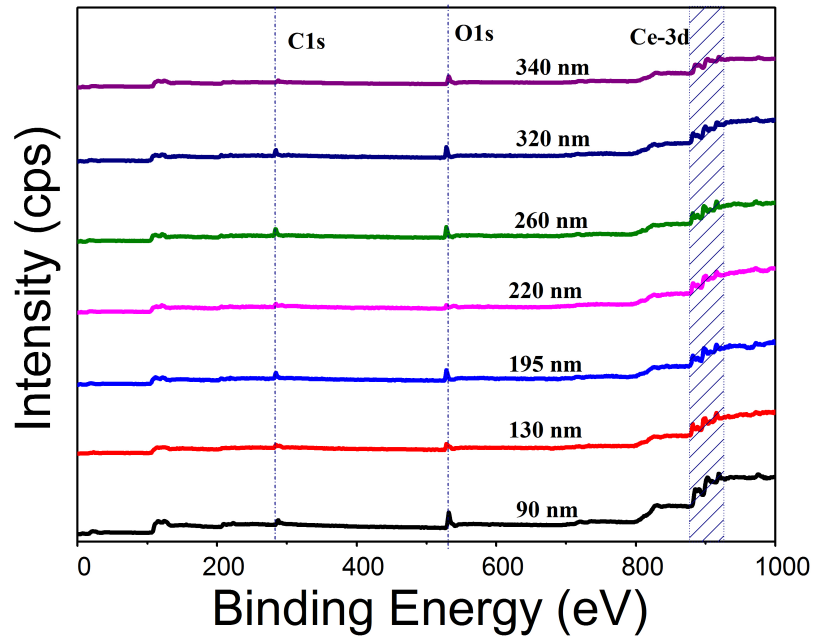


Figure 4.4: XPS wide spectra of CeO₂ films of various thicknesses

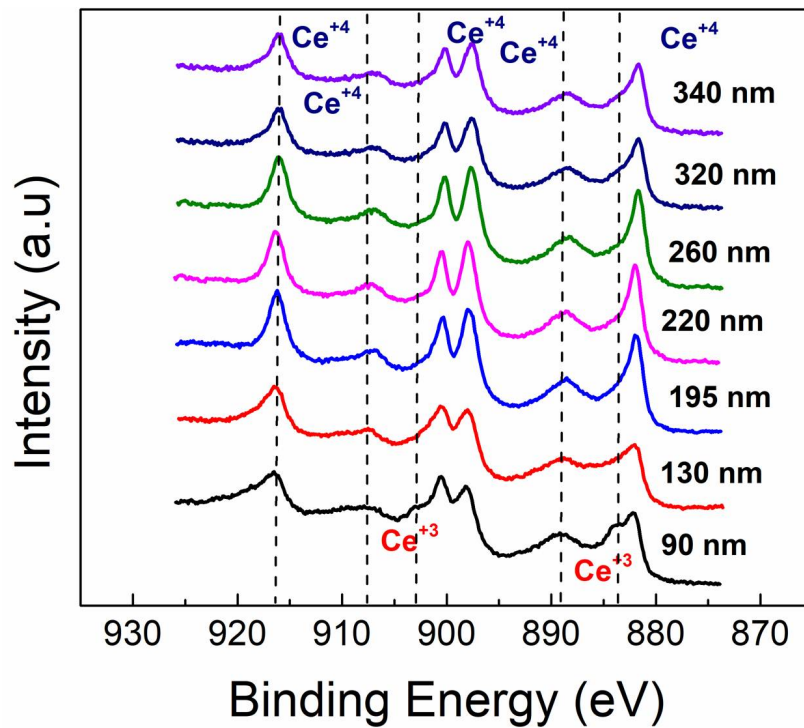


Figure 4.5: High Resolution XPS spectra (Ce-3d level) of CeO₂ films for different thickness

To quantify the oxidation states of Ce (Ce^{+4} and Ce^{+3}) and their variation with the CeO_2 film thicknesses, the Ce-3d spectrum was deconvoluted using Casa XPS software with Shirley background correction, 30% Gaussian and 70% Lorentzian peak fitting. The peaks at 882.0, 884.9, 888.5 and 897.9 eV corresponds to the components of $Ce-3d_{5/2}$, while the peaks at 900.6, 903.6, 907.2 and 916.2 eV are attributed to the components of $Ce-3d_{3/2}$. The Ce-3d level consists of two components : the major component (peaks at the B.E 882.5, 888.2, 898, 901.1, 907.2 and 916 eV) corresponds to Ce^{+4} cations (as marked in Fig. 4.5) in the CeO_2 lattice and the minor component (peaks at the B.E 881.1, 885.83, 899.65 and 904.3 eV) corresponds to Ce^{+3} in amorphous Ce_2O_3 Zhang *et al.* (2016), Holgado *et al.* (2000) and Zhu *et al.* (2014). The total fraction of Ce_2O_3 (Ce^{+3}) in the deposited CeO_2 films were estimated by taking the percentage of fitted Ce^{+3} spectral weight to the total weight of the spectra ($Ce^{+3} + Ce^{+4}$) and calculated using the following equation Zhu *et al.* (2014):

$$\%Ce^{+3} = \frac{Ce^{+3}}{Ce^{+3} + Ce^{+4}} \quad (4.1)$$

As there are no other Ce oxidation states detected in the CeO_2 films except Ce^{+4} and Ce^{+3} , the fraction of except Ce^{+4} (CeO_2) can be calculated by :

$$\%Ce^{+4} = 1 - \%Ce^{+3} \quad (4.2)$$

All the calculated $\%Ce^{+4}$ and $\%Ce^{+3}$ components and their fraction $Ce^{+3}/(Ce^{+3} + Ce^{+4})$ are summarized in Table 4.2.

Table 4.2: Summary of calculated $\%Ce^{+3}$ and $\%Ce^{+4}$ components and fraction of Ce^{+3} components

Thickness (nm)	Ce^{+3} (%)	Ce^{+4} (%)	$Ce^{+3}/(Ce^{+3} + Ce^{+4})$
90	27.0	73.0	0.27
130	27.5	72.5	0.275
195	19.6	80.4	0.20
220	17.0	83.0	0.17
260	16.0	84.0	0.16
320	12.0	88.0	0.13

It has been observed that the $\%Ce^{+3}$ component and the fraction $Ce^{+3}/(Ce^{+3} + Ce^{+4})$ are decreasing with increase in CeO_2 film thickness, which indicates that the

defects and the oxygen vacancies are decreasing Zhao *et al.* (2013), Ujjain *et al.* (2014) and Sudarsanam *et al.* (2014). This shows that the stoichiometry and quality of the films are improving with increase in thickness (from 90 to 340 nm). However the stoichiometry of the thinner films (≤ 90 nm) can be improved by controlling the process parameters such as oxygen flow rate, substrate temperature and deposition rate which needs to be investigated.

4.3.3 Surface topography

Fig. 4.6 shows the AFM (3D) micrographs of CeO₂ films of various thicknesses. It clearly shows that the grain size increases with the increase of thickness which might be due to improvement in grain growth with the thickness. This is in good agreement with the XRD data. Also, it has been observed that the RMS roughness of the films increases monotonically with the thickness; however the increment is very minimal.

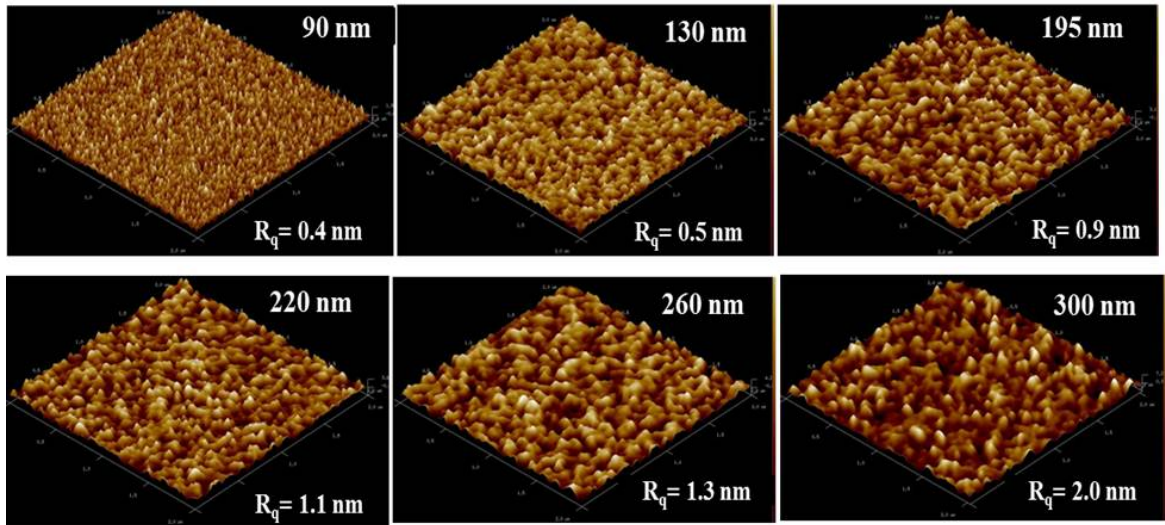


Figure 4.6: 3D AFM micrographs of CeO₂ films of various thicknesses

It is important to note that the films are grown at high temperature (400°C) which may result in hillocks type of film structure Denhoff *et al.* (1995) due to high surface mobility at higher temperature. This causes increase in surface roughness which might affect the gas sensitivity of the film since larger roughness results in larger contact area with the gaseous species Majumder and Roy (2018), Durrani *et al.* (2008), Sucheai *et al.* (2006).

4.3.4 Structural properties

XRD characterization has been carried out to understand the structural details of the grown films. Fig. 4.7 shows the XRD patterns of the CeO_2 films of various thicknesses.

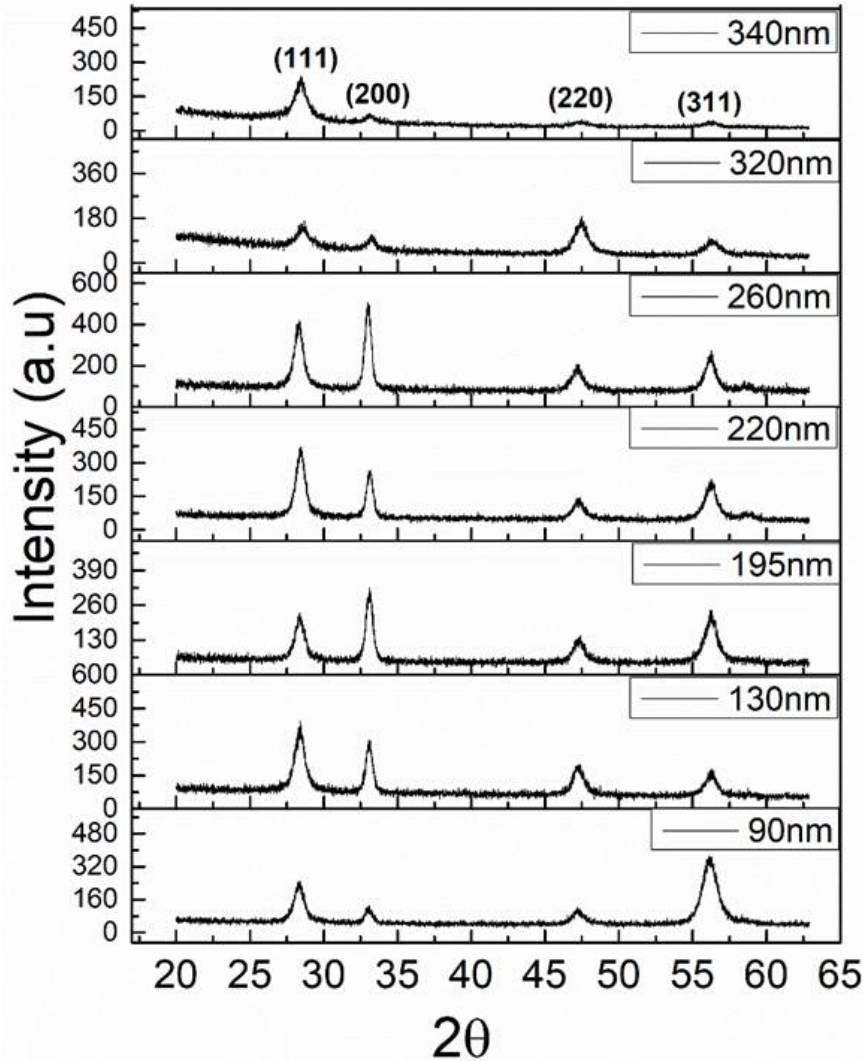


Figure 4.7: XRD patterns of CeO_2 films of various thicknesses

The characteristic peaks of the XRD patterns match with that of CeO_2 (JCPDS no. 043-1002). The peaks were indexed with fluorite cubic structure with $Fm-3m$ space group. XRD patterns are composed of four strong and broad peaks corresponding to the (111), (200), (220) and (311) reflections from CeO_2 films peaks at a 2θ of 28.4° , 33.1° , 47.3° and 56.2° respectively. This indicates that all the films are polycrystalline in nature. No other phases of CeO_2 such as Ce_2O_3 and CeO_{2-x} have been observed as

seen from XPS data (Ce^{+3} oxidation state), however Ce_2O_3 might be present in the amorphous form and below the XRD detection limit.

The crystallite size of all the films was calculated from (111), (200), (220) and (311) peaks of XRD using Scherrer's formula Cullity (1956) and the values are presented in Table 4.3. The crystallite size has been increasing with the increase of thickness upto 260 nm, which might be due to improvement in grain growth with an increase in thickness, however, crystallite size has decreased in thicker films (>260 nm). Above 260 nm, the interaction between the added (added atom) layer and substrate may be decreasing with increase in thickness. This might be due to low mobility of the add atoms on the surface of the growing film which may hamper the grain growth and film orientation. However, it requires detailed investigation to understand the nucleation process.

In general, the fluorite cubic CeO_2 has a tendency to grow in (111) orientation under normal deposition conditions because of the lowest surface energy due to highest atomic packing density along (111) plane Izu *et al.* (2002a), Izu *et al.* (2003b). But in this case, it has been observed that the intensity of (200) plane increases with the increase of CeO_2 film thickness.

To quantify the preferred orientation, texture coefficient has been calculated using the following expression Agashe *et al.* (1988) and the values are presented in the Table 4.3.

$$TC(hkl) = \frac{\frac{I(hkl)}{I_o(hkl)}}{\frac{1}{N} \sum N \frac{I(hkl)}{I_o(hkl)}} \quad (4.3)$$

where N is the number of diffraction peaks, $I(hkl)$ and $I_o(hkl)$ are respectively the measured and corresponding recorded intensities according to (JCPDS no. 043-1002) card.

From Table 4.3, it is also seen that the growth along the (200) orientation increases with increase in thickness upto 260 nm and then decreased for higher thicknesses (>260 nm). It appears that the 260 nm is the critical thickness where the film has stoichiometry, lowest resistance due to better crystallinity, reasonable surface roughness and also orientation in (200) direction which has the highest surface energy compared to other planes.

Table 4.3: Summary of Crystallite Size (D) and Texture Coefficient (TC) of CeO₂ Films of Various Thicknesses

Thickness nm	(111)		(200)		(220)		(311)		Average Crystallite size
	D (nm)	TC	D (nm)	TC	D (nm)	TC	D (nm)	TC	
90	10.4	0.51	14.7	0.95	9.5	0.55	7.8	1.99	10.6
130	10.6	0.65	15.6	1.83	10.3	0.72	10.1	0.80	11.6
195	11.1	0.65	15.4	1.69	9.9	0.52	9.1	1.20	11.4
220	11.7	0.41	16.4	1.90	10.3	0.54	9.9	1.12	12.1
260	11.8	0.50	16.9	2.13	10.2	0.54	11.4	0.80	12.6
320	10.6	0.51	13.8	1.30	8.2	1.30	7.6	0.90	10.1
340	9.3	1.28	12.8	1.41	6.9	0.55	7.1	0.75	9.1

4.3.5 Gas Sensing Characteristics

For sensing measurement, initially the sensing chamber was evacuated by connecting it to a high capacity vacuum pump. The sensor was exposed to pure nitrogen gas until the constant baseline resistance was achieved and then the gas analyte (oxygen) was introduced into the chamber. The signal from the sensor was continuously recorded in real time with the help of a Matlab R2010a programme through which the data is acquired every second. During this time, the steady resistance has been achieved, and then the sensing chamber was flushed with pure nitrogen consecutively to allow the surface of the sensitive film to regain atmospheric condition and the resistance reached steady and kept stable. The Sensitivity is defined as :

$$Sensitivity(S) = \frac{R_g}{R_a} \quad (4.4)$$

where R_g is the real time film resistance upon exposure to target gas and R_a is the initial film resistance in high purity nitrogen atmosphere.

Fig. 4.8 shows the variation of the response of the sensor (sensitivity) with the CeO₂ film thickness at an operating temperature of 400°C.

The variation in sensitivity of the films with respect to thickness is explained on the basis of the structural, electrical and compositional data. The 90 nm CeO₂ film did not show any response with oxygen gas because of very high resistance. From Fig. 4.8, it has been observed that the sensitivity has increased with increase in CeO₂ film thickness from 130 nm to 260 nm and then decreased for films thicker than 260

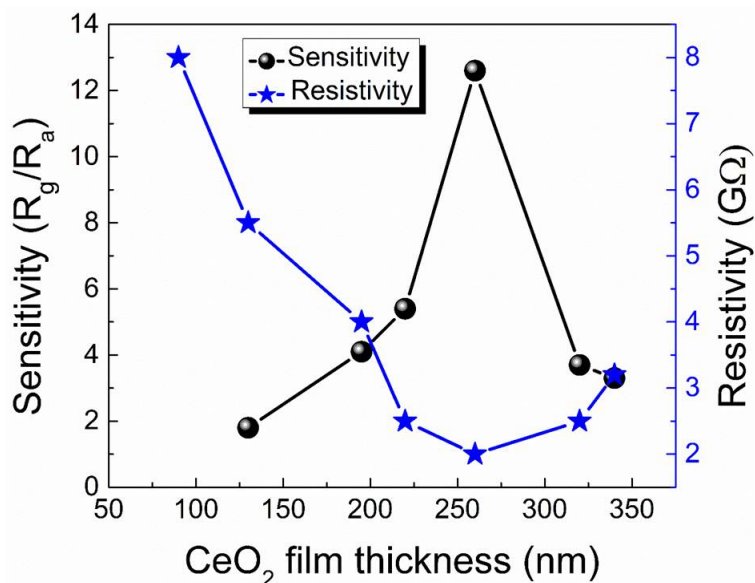


Figure 4.8: Variation of response of the sensor (sensitivity) and resistance with the CeO₂ film thickness at an operating temperature of 400°C

nm. The increase of sensitivity with an increase in thickness may be attributed to the increase of (200) preferred orientation as evident from XRD data (as shown in Table 4.3). The (200) plane of CeO₂ has highest surface energy and hence high reactivity when compared to other planes due to defects or oxygen vacancies Younis *et al.* (2016) and Hu *et al.* (2016). Along with the (200) plane, the contribution of other planes (111) (220) (311) are also significant which indicates more polycrystalline nature and hence more active sites. The low sensitivity for films thicker than 260nm compared to other films (≤ 260 nm) can be probably attributed to the high resistance of the film at 400°C. From this, we may conclude that a thickness of 260 nm with perfect stoichiometry, reasonable surface roughness, lowest resistance (better crystallinity), and also orientation in (200) direction (highest surface energy compared to other planes) seems to be the optimum thickness for CeO₂ based oxygen sensors

Fig. 4.9 shows the response of 260 nm CeO₂ film at an operating temperature of 400°C for 100% gas concentration. From this figure, it clearly indicates that the sensors response is reproducible.

Fig. 4.10 shows the dynamic response (sensitivity) of the 260 nm CeO₂ thin film sensor at an operating temperature of 400°C. The sensor was exposed to pure N₂ followed by successive oxygen gas pulses of 100%, 50%, 35%, 20%, 10% and 1%.

From Fig. 4.10, it is evident that the sensor responds even at low oxygen levels (1%

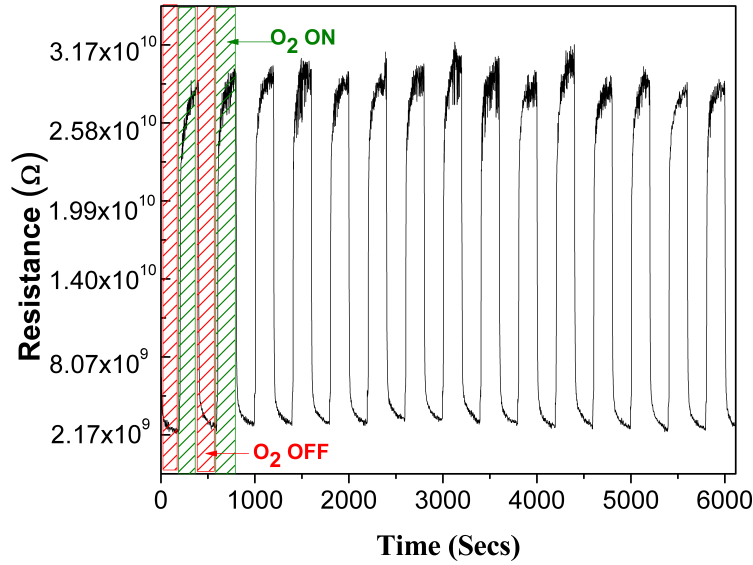


Figure 4.9: Reproducible sensor's response of the 260 nm CeO₂ film at fixed O₂ concentration of 100%

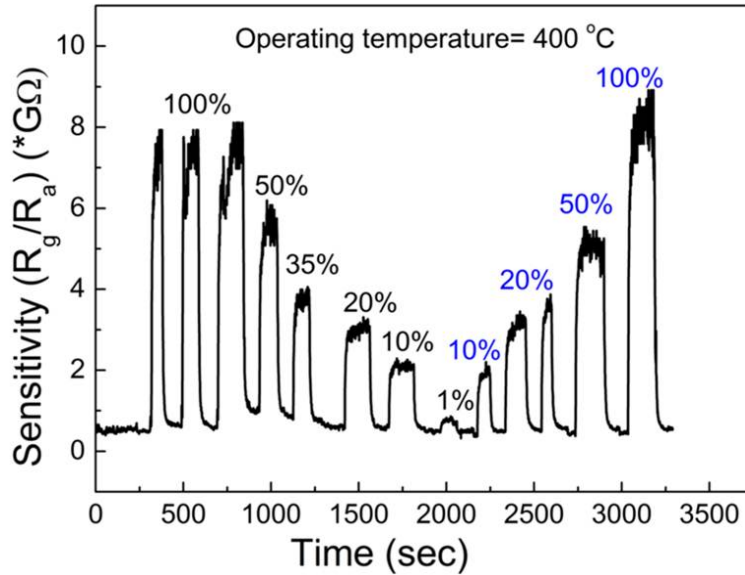


Figure 4.10: Dynamic response (sensitivity) of the 260 nm CeO₂ thin film sensor at an operating temperature of 400°C

which is equivalent to 10,000 ppm). However, it has been observed that the response of the sensor (sensitivity) decreases with the decrease of O₂ levels without much change in response time ($\tilde{10}$ -15 s). The measured response time is typically ≤ 10 s whereas the recovery time (t_{90}) is approximately 15s along with very high sensitivity of 12.6 for 100% oxygen levels. Izu *et al.* (2002a) calculated the response time as 35 s and 8

s at the operating temperatures of 808°C and 1002°C respectively for the CeO₂ based oxygen sensors based on diffusion coefficient, surface reaction coefficient and particle size. Our sensor performance has been compared with the best CeO₂ based oxygen sensors reported in the literature and summarized in Table 4.4.

Table 4.4: Comparison of this sensor performance with reported literature

Synthesis method	Thickness	Operating Temperature (°C)	Response Time	Ref
RF Sputtering	90-340 nm	400	≤10s	This work
Screen printing	5-30 μm	800	10 ms	Beie and Gnörich (1991)
RF Sputtering	0.5-1μm		(Estimated by Fick's second law)	
Mist Pyrolysis	–	808	35 s	Izu <i>et al.</i> (2002a)
		857	22 s	
		905	15 s	
		953	11 s	
Mist Pyrolysis	20-30μm	1002	8 s	Izu <i>et al.</i> (2003b)
		615	11s	
Mist Pyrolysis	20-30μm	712	10s	Izu <i>et al.</i> (2002b)
Mist Pyrolysis	30μm	615	11-42 s	Izu <i>et al.</i> (2003a)
		662	16-20 s	
Spin coating	μm range	700	<60s	Jasinski <i>et al.</i> (2003)
MOCVD	500 nm	600 - 1000	9-80 s	Izu <i>et al.</i> (2004)
Sputtering				
wet-chemical precipitation method	–	600-850	>60s	Chen and Chang (2012)

This sensor's response time (≤10 s) and recovery time (15 s) reported are the lowest values with very high sensitivity (12.6) at a lowest operating temperature (400°C) reported till today in case of undoped CeO₂ thin film sensors. Also, the response of our sensor is reproducible for all concentrations tested returning to the baseline resistance following each successive pulse of analyte (oxygen gas). The composition, porosity and packing density of the sensor film may change after exposure to target gas (oxygen), which can change the base resistance of the film. As such, we did not observe any change in the base resistance of the sensor film (CeO₂) after the exposure to oxygen at 400°C, which indicates that the sensor film is stable in terms

of composition and packing density, and also attains its equilibrium condition once the gas is removed. The base resistance of the CeO₂ film is stable and no drift has been observed over many cycles of gas sensing at different gas concentrations. Since the base resistance is stable, we did not perform any characterizations to check the quality of the CeO₂ film after exposure to oxygen gas. This superior performance of CeO₂ thin film based oxygen sensor may be attributed to the combination of three factors i.e :

1. high surface energy and reactivity due to the presence of (200) oriented CeO₂ plane
2. low resistance due to better crystallinity
3. perfect stoichiometry with required roughness

The cross sensitivity measurements have been performed on different gases such as CO₂, CO, NO_x and no response has been found for gases other than oxygen. The optimized CeO₂ (260 nm) films did not show any sensing at 400°C towards CO₂ (1000 ppm), CO (5 ppm) and NO_x (5 ppm) which indicates that these films may not be highly porous and having required surface to volume ratio as compared to nanoparticles and nano structures of CeO₂ Durrani *et al.* (2008), Chougule (2018) and Aboud *et al.* (2018). This indicates that our CeO₂ films are selective to oxygen gas at an operating temperature of 400°C. However the CeO₂ films may show sensing towards CO₂, CO and NO_x at higher concentrations, which needs further investigation.

For practical applications, this sensor should be associated with some measurement solution systems which are based on current conveyor, resistance to frequency, resistance to number, resistance to period and logarithmic, high precision, differential circuits. It also requires a user interface consisting of gas sensor with various level of electronic signal conditioning in terms of both hardware and software, to achieve the measured resistance.

4.4 Conclusion

CeO₂ thin films of different thicknesses ranging from 90 nm to 340 nm have been deposited at 400°C using RF magnetron sputtering on Al₂O₃ substrate. Characterization

techniques such as Ellipsometry, XRD, XPS and AFM have been used to characterize the CeO₂ films for their thickness, structural, compositional/chemical and surface morphological properties. The O/Ce ratio increased from 1.4 to 2.0 with increase in thickness from 90 to 195 nm. All the films with thickness more than 195 nm appear to be stoichiometric. The film resistivity seems to be related with (200) plane orientation. It is minimum for oriented film of thickness 260 nm which has maximum textured coefficient and the corresponding sensitivity is maximum. Surface roughness increased with film thickness. Once the film has the required composition and roughness, the crystallinity and orientation of (200) plane are contributing to minimum resistivity and maximum sensitivity. The CeO₂ film with an optimum thickness of 260 nm has shown very high sensitivity (12.6), fast response time (≤ 10 s) and recovery time (15 s) at a low operating temperature of 400°C, which are the best values reported till date in case of undoped CeO₂ thin film based sensors. The response time of CeO₂ based sensor may be reduced further by increasing the conductivity of the CeO₂ films with appropriate dopants.

Chapter 5

Process Optimization and Characterization of $\text{CeO}_2\text{--HfO}_2$ films deposited by RF Sputtering Technique

5.1 Introduction

In recent years, mixed metal oxide compounds are getting lot of attention for the development of high performance sensors. In mixed oxides, the resistance of the compound, for ease of electronic interface can be controlled or modified by varying the composition of the constituents which can be alter the structural and electrical properties of the mixed oxide.

As a sensing material, metal oxide such as Hafnium oxide (HfO_2) is one of the potential metal oxide for gas sensors because of its excellent properties such as chemical, thermal, and mechanical stability Capone *et al.* (1998). Also, it is very sensitive to reaction of target molecules with adsorbed oxygen or the oxygen in the lattice itself because of its good ionic conduction properties. Nevertheless, impurities, defects, and oxygen vacancies due to deposition technique processes can generate intermediate states in the gap of the oxide, making it an n-type semiconductor Capone *et al.* (1998), Durrani and Al-Kuhaili (2008).

No extensive study on the effect of thickness of mixed oxide films (CeO_2 and HfO_2)

has been reported though both possess excellent properties to be used in gas sensors. Hence, here in this chapter we report the oxygen gas sensors based of CeO₂ and HfO₂ mixed oxide thin films developed by RF-sputtering technique.

This chapter discusses the synthesis of mixed oxide (CeO₂ and HfO₂) thin films by a novel technique in RF sputtering. Best oxygen sensors based on mixed oxide (CeO₂ - HfO₂) thin films have been developed by controlling and tuning the resistance of the films. This has been done by varying the size (from 1 mm × 1 mm to 5 mm × 5 mm) and number (from 2 to 4) of HfO₂ pellets which are placed on 3-inch CeO₂ sputtering target. The sensor performance is better than the CeO₂ based oxygen sensors reported in Chapter-4. The sensing performance and characteristics have been understood and evaluated using various characterization techniques like TEM-EDS, SEM-EDS, XPS and XRD.

5.2 Results and discussion

The sputtering process parameters used in this chapter are listed below in Table 5.1.

Table 5.1: Sputtering parameters used for deposition of CeO₂-HfO₂

Technique	RF sputtering
Target	CeO ₂ (99.99%)
HfO ₂ pellets	2-4; 1 mm thick
Argon	25 sccm
Oxygen	2 sccm
Sputtering gas pressure	2.5 × 10 ⁻³ mbar
Power	75 W
Substrate to target distance	8.0 cm
Substrate temperature	400 °C
Annealing temperature	500 °C
Annealing duration	2 hours

Here the characterization of CeO₂-HfO₂ films which includes thickness, structural, compositional/chemical, and surface morphology properties are presented along with the gas sensing results.

5.2.1 Thickness measurement

The $\text{CeO}_2\text{-HfO}_2$ mixed oxide thin films of different thicknesses were deposited on Al_2O_3 substrates by placing two HfO_2 pellets of size $5\text{ mm} \times 5\text{ mm} \times 1\text{ mm}$ on the 3-inch CeO_2 target; the deposition time was varied from 30–240 minutes, keeping all the other process parameters as constant. The thickness of the deposited films was measured using ellipsometry and validated using cross-sectional SEM and Dektak surface profilometer. The measured thickness of the films was in the range of 38–295 nm and varied linearly with the deposition time at constant power. The Fig. 5.1 shows the cross-sectional SEM images of the film deposited for 180 minutes and the measured thickness was around $220 \pm 10\text{ nm}$, which is in good agreement with the ellipsometry data.



Figure 5.1: Cross-sectional SEM image of the $\text{CeO}_2\text{-HfO}_2$ film deposited for 180 minutes

5.2.2 Gas sensing characteristics

The gas sensing measurements were performed with N₂ and N₂-O₂ mixtures at an elevated temperature of 400°C for different concentrations of oxygen varying from 20–100% and changes in the resistance of sensor were recorded.

It was observed that the sensor film (CeO₂-HfO₂) did not show any response to oxygen gas upto a film thickness of 80 nm because of very high resistance. The films of thickness around 86 nm showed sensing, but the response and recovery times were higher (41 s and 49 s respectively). The sensor's performance (sensitivity, response and recovery times) improved with an increase in thickness from 86 to 220 nm; however, a decreasing trend was observed above an optimum thickness of 220 nm. The decrease in the sensor's performance above 220 nm may be because of the dominance of bulk conductivity over the change in surface conductance. In semiconductor based gas sensors, the surface conductance or resistance modulation is the key for sensor response rather than a change in bulk conductance Rudraswamy and Bhat (2016). The oxygen sensitivity of the 220 nm CeO₂-HfO₂ film was ~14.15, which is higher than pure CeO₂ oxide thin films Ramshanker *et al.* (2019). However, the response and recovery times were still higher (20 s and 22 s respectively). This may be improved further by tuning the resistance and structure of the mixed oxide films, which can be achieved by controlling the Ce and Hf concentrations of the mixed oxide (CeO₂-HfO₂) thin films. Hence, the next set of experiments were carried out to tune the Hf concentration by varying the size and number of HfO₂ pellets to be placed on the CeO₂ target. One set of experiments were carried out by varying the size of the pellets from 1 mm × 1 mm to 5 mm × 5 mm while fixing the number of pellets as 2. Another set of experiments were carried out by varying the number of pellets between 2–4. The sample details and the corresponding gas sensing characteristics are listed in Table 5.2.

From Table 5.2, it can be clearly observed that the mixed oxide films deposited with 2 HfO₂ pellets of size 3 mm × 3 mm and 4 mm × 4 mm show better sensing performance compared to all other films. The variation in response of the films with oxygen gas can be explained on the basis of the electrical, compositional data structural characteristics of the CeO₂-HfO₂ mixed oxide films.

It was observed that the introduction of HfO₂ in CeO₂ significantly lowers the resistance (from 10⁹ to 10⁷ Ω) when compared to the previous work on pure CeO₂ Ramshanker *et al.* (2019). This falls in line with the resistance measurements reported by Izu *et al.* (2005b), Izu *et al.* (2005a), Izu *et al.* (2007), Scheffe *et al.* (2013)]. Hence,

Table 5.2: Summary of the oxygen gas sensing characteristics of CeO₂-HfO₂ mixed oxide films (t=220 nm) deposited by varying number and size of HfO₂ pellets

No. of HfO ₂ pellets	Size of pellets (mm)	Response time (s)	Recovery time (s)
2	1 × 1	15	17
2	2 × 2	12	15
2	3 × 3	8	10
2	4 × 4	8	10
2	5 × 5	15	20
3	5 × 5	30	33
4	5 × 5	37	48

the variation in the resistance of CeO₂-HfO₂ mixed oxide films can be attributed to the variation of Hf concentration in the films. Therefore, the atomic concentrations of Ce and Hf elements were calculated to understand the oxygen sensing characteristics and also to identify a suitable Hf concentration to develop the best oxygen sensor.

5.2.3 Compositional results

In order to determine the composition (atomic concentrations) of the CeO₂-HfO₂ mixed oxide films, a combination of Transmission Electron Microscopy (TEM) and Energy Dispersive Spectroscopy (EDS) was used. The samples were analyzed by focusing a narrow electron beam on the sample and obtaining the resulting x-ray spectrum. Each of the elements of interest (Ce and Hf) have distinct x-ray emission spectra, as shown in Fig. 5.2. The qualitative maps of the composition were constructed by collecting the x-ray spectra from an array of points and it was found that Hf was distributed uniformly in the films. The quantitative average elemental composition (atomic percentage of each element) was measured by expanding the beam to cover a large area and the error estimates were obtained using the Velox software. The summary of the atomic percentage of Ce and Hf elements in the mixed oxide thin films and their corresponding oxygen sensing characteristics are shown in Table 5.3. The atomic concentration of Hf varies from 7% to 23% with an increase in the size and number of HfO₂ pellets.

From Table 5.3, it is clear that the Hf concentration increases with an increase in the size as well as the number of pellets and hence, the Hf concentration can be controlled via the size or number of HfO₂ pellets. From the oxygen sensing data,

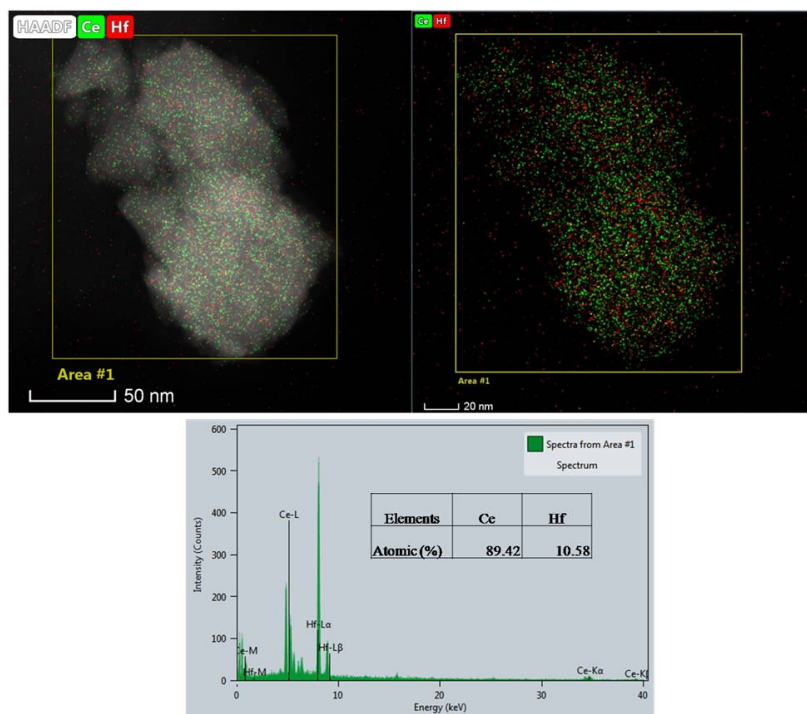


Figure 5.2: TEM-EDS mapping of Ce-Hf film

it appears that films with around 10–11% of Hf concentration have better sensing performance in terms of response and recovery times of 8 s and 10 s respectively.

Table 5.3: Summary of varied atomic concentration (by varying the size and number of HfO₂ pellets) of Ce and Hf and their corresponding gas sensing characteristic.

No. of HfO ₂ pellets	Size of pellets (mm)	Ce (at %)	Hf (at %)	Response time (s)	Recovery time (s)
2	1×1	93.9	6.9	15	17
2	2×2	91.0	9.0	12	15
2	3×3	89.4	10.6	8	10
2	4×4	88.8	11.2	8	10
2	5×5	87.5	12.5	15	20
3	5×5	80.1	19.9	30	33
4	5×5	77.1	22.9	37	48

The elemental composition of these films was also validated through FESEM–EDS (shown in Fig. 5.3) and XPS analysis.

The Fig. 5.4 (a) shows the XPS survey spectrum of the film deposited with two

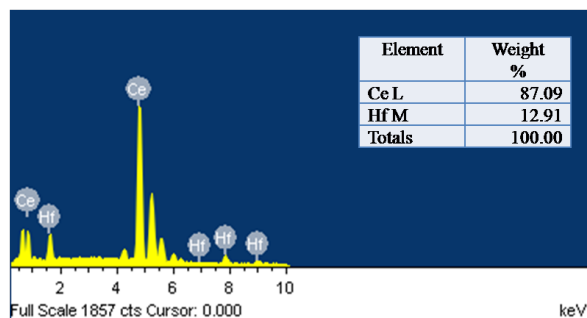


Figure 5.3: SEM-EDS of Ce-Hf Analysis

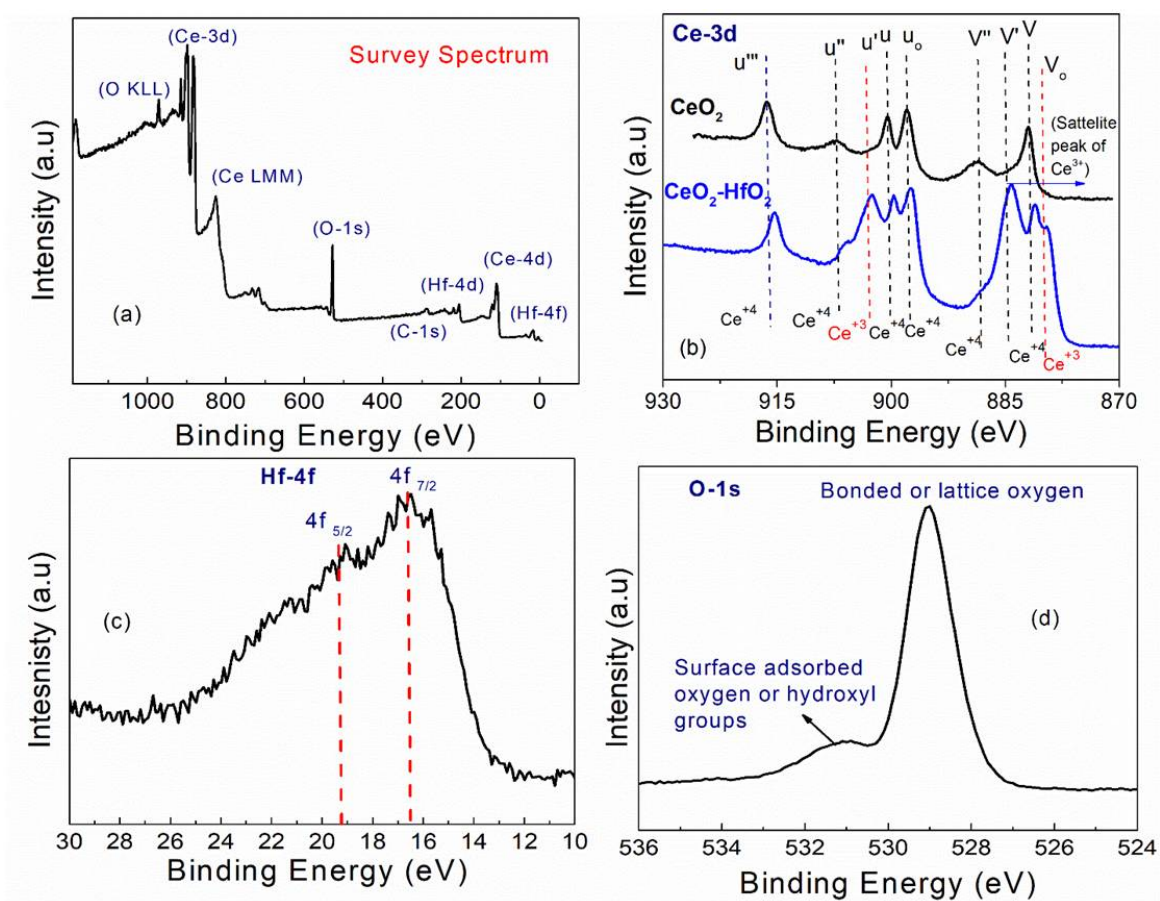


Figure 5.4: (a) XPS survey spectra of 220 nm $\text{CeO}_2\text{-HfO}_2$ mixed thin film; (b) high resolution XPS spectra of Ce-3d of standalone 220 nm CeO_2 film and mixed oxide film; (c) and (d) high resolution XPS spectra of Hf-4f and O-1s of 220 nm $\text{CeO}_2\text{-HfO}_2$ mixed thin films respectively

HfO_2 pellets of size 4 mm \times 4 mm. The spectrum clearly shows the presence of Hf in the film. The atomic concentrations of Ce and Hf present in the mixed oxide films

were extracted by using relative sensitivity factors (RSF) of the individual elements. It was found that the Hf concentration increases with an increase in the size and number of HfO₂ pellets and the results are in good agreement with the TEM-EDS analysis.

XPS was also used to investigate the oxidation states of Ce and Hf in the mixed oxides. The Ce-3d core level peak (as shown in Fig. 5.4 (b)) had a complex structure due to the strong hybridization of the Ce-4f and O-2p states in cerium oxide. Two possible oxidation states of cerium oxide, Ce³⁺ and Ce⁴⁺ having nine different features were found in the Ce-3d region. The interpretation was done by the standard notations used in literature Zhang *et al.* (2016), Holgado *et al.* (2000) and Zhu *et al.* (2014). The assignment of features in the Ce-3d spectra can be seen in Fig. 5.4(b) for both pure CeO₂ films and CeO₂-HfO₂ mixed oxide films. The peaks labeled as '*v*' correspond to Ce 3d_{5/2} contributions and those labeled as '*u*' represent the Ce 3d_{3/2} contributions. The peaks *u_o* and *u* are the main Ce 3d_{3/2} lines of Ce³⁺, and the peaks *v_o* and *v* are the main Ce 3d_{5/2} lines of Ce⁴⁺. The peak labeled as *v'* is a satellite to the Ce³⁺ 3d_{5/2} main line *v_o*, whereas *v''* is related to Ce⁴⁺ (main line *v*). From Fig. 5.4(b), it is evident that the Ce³⁺ concentration was more in the mixed oxide films (CeO₂-HfO₂) compared to pure CeO₂ films. Moreover, the peaks centered around 899.5 eV and 881.1 eV are the principal binding energies of Ce 3d_{3/2} and Ce 3d_{5/2} respectively, which are significantly lower (0.5 to 1 eV) than the values typical for Ce⁴⁺ (900.2–900.6 and 881.7–882.0 eV respectively) in CeO₂. This suggests a significant concentration of Ce³⁺ ions on the surface region of the mixed oxide films and hence, the surface region is strongly reduced.

The Fig. 5.4(c) shows the high resolution spectrum of Hf-4f; this is a broad peak that can be de-convoluted into four peaks. The broadness of the peak may be attributed to the low concentration of Hf in the film. The binding energy of the Hf-4f_{7/2} peak would be around 16.5–17 eV and the spin orbit splitting (the separation between Hf-4f_{7/2} and Hf-4f_{5/2}) would be 1.7 eV for bulk and stoichiometric HfO₂ films Lakshmi Ganapathi *et al.* (2013) and Ganapathi *et al.* (2014). From Fig. 5.4(c), it was observed that the Hf-4f_{7/2} peak was centered at around 16.7 eV but the spin orbit splitting was between 2.2–2.4 eV. This indicates that hafnium is not in the Hf⁴⁺ oxidation state on the surface of the mixed oxide film and may be present in the form of HfO_x where x<2. The position of the primary O 1s feature was ~529.1 eV (shown in Fig. 5.4(d)), which is almost 1 eV lower than the lattice oxygen present in

the stoichiometric mixed cerium–hafnium oxide (530.3 eV in $Ce_xHf_{1-x}O_2$) reported in literature Izu *et al.* (2005b). The small peak centered at around 531 eV may be attributed to the surface adsorbed oxygen (possibly from absorbed water and/or carbonates). The XPS results conclude that the surface of the CeO_2 – HfO_2 mixed oxide film is strongly reduced due to oxygen vacancy formation with the addition of HfO_2 to CeO_2 . The reduced surface of the mixed oxide film may be the reason for the high response towards oxygen gas compared to CeO_2 standalone films. The optimum atomic concentration of Hf (10–11%) plays an important role in high performance oxygen gas sensing in terms of response and recovery times, which can be explained based on the structural data.

5.2.4 Structural analysis

XRD characterization was carried out to understand the structural details of the mixed oxide films. The Fig. 5.5 shows XRD patterns of the CeO_2 – HfO_2 films.

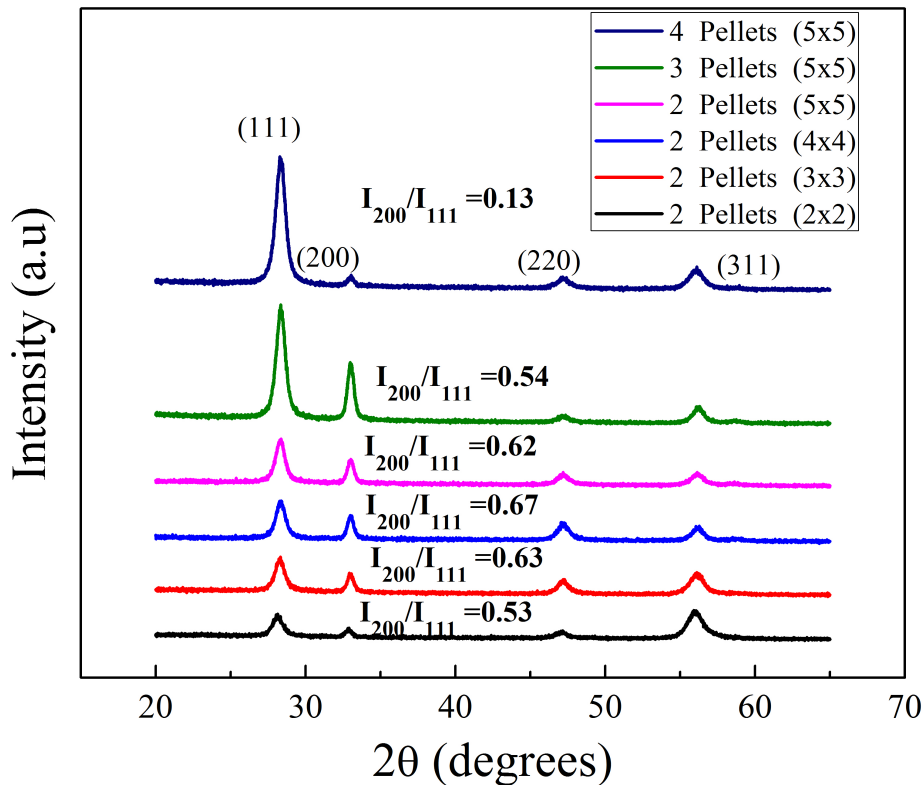


Figure 5.5: XRD patterns of CeO_2 – HfO_2 mixed oxide films with varying Hf concentrations

The characteristic peaks of the XRD patterns were matched with that of CeO₂ (JCPDS no. 043–1002). The peaks were indexed with fluorite cubic structure with Fm-3m space group. The XRD patterns were composed of four strong and broad peaks corresponding to the (111), (200), (220) and (311) reflections from CeO₂ films peaks at 2θ of 28.4°, 33.1°, 47.3° and 56.2° respectively. This indicates that all the films are polycrystalline in nature. No other phases of CeO₂ such as Ce₂O₃ and CeO_{2-x} were observed as seen from the XPS data (Ce³⁺ oxidation state). Also, no characteristic peaks related to HfO₂ were observed; this may be due to the presence of HfO₂ in the amorphous phase. However, a slight shift in all the peak positions around 0.3 to 0.4 degrees towards a higher angle was observed. This shift in the peak positions can be attributed to the presence of Hf in the film, which may have induced a strain in the CeO₂ lattice Izu *et al.* (2005b), Izu *et al.* (2007), Wang *et al.* (2008), Bonk *et al.* (2016).

In general, the fluorite cubic CeO₂ tends to grow in the (111) orientation under normal deposition conditions because of the lowest surface energy due to the highest atomic packing density along the (111) plane Izu *et al.* (2002a), Izu *et al.* (2003b). But, in this work, it was observed that the intensity of the (200) plane increases with an increase in the Hf concentration upto 11% in the CeO₂ film, after which it showed a decreasing trend. To quantify the preferred orientation, the intensity ratios of the (200) and (111) planes were calculated; it was found that the ratio increased to 0.67 upto 11% of Hf concentration and then showed a decreasing trend. A detailed investigation is required to understand the nucleation process.

The improvement in the oxygen sensing characteristics in CeO₂-HfO₂ films with an increase of Hf concentration (upto 11%) can be attributed to the increase of (200) preferred orientation since the (200) plane of CeO₂ has highest surface energy and hence, high reactivity when compared to other planes Younis *et al.* (2016), Hu *et al.* (2016).

From the XRD and XPS data, it can be concluded that the good sensing characteristics of CeO₂-HfO₂ mixed oxide films between 10–11% atomic concentration of Hf can be attributed to the existence of the highly reactive plane (200) with the highest surface energy and strongly reduced surface, with oxygen vacancy formation due to the presence of Ce³⁺ ions and HfO_x, x<2 on the surface of the mixed oxide films.

From the gas sensing data, it was observed that as the Hf concentration increases upto 11%, there is an improvement in the response and recovery times. This might

be due to an increase in oxygen vacancies with introduction of Hf. Further increase in Hf concentration (above 11%) is leading to structural changes [from XRD data it has been observed that the preferred orientation of the films, (200) orientation has changed to (111) plane orientation], which may limit the oxygen vacancies as the (111) orientation is highly packed plane. This can result in an increase of response and recovery times due to low surface energy of (111) planes with low defect density compared to (200) oriented planes.

The uniform distribution of Hf was validated using the Field Emission Electron Probe Microscope Analysis (EPMA) using the EPMA-JEOL JXA-8530F tool. The EPMA results (Fig. 5.6) showed that Hf is uniformly distributed in the film and CeO₂ matrix (red colour = Ce, blue colour = Hf and green colour = Oxygen). These results are in good agreement with the TEM-EDS mapping.

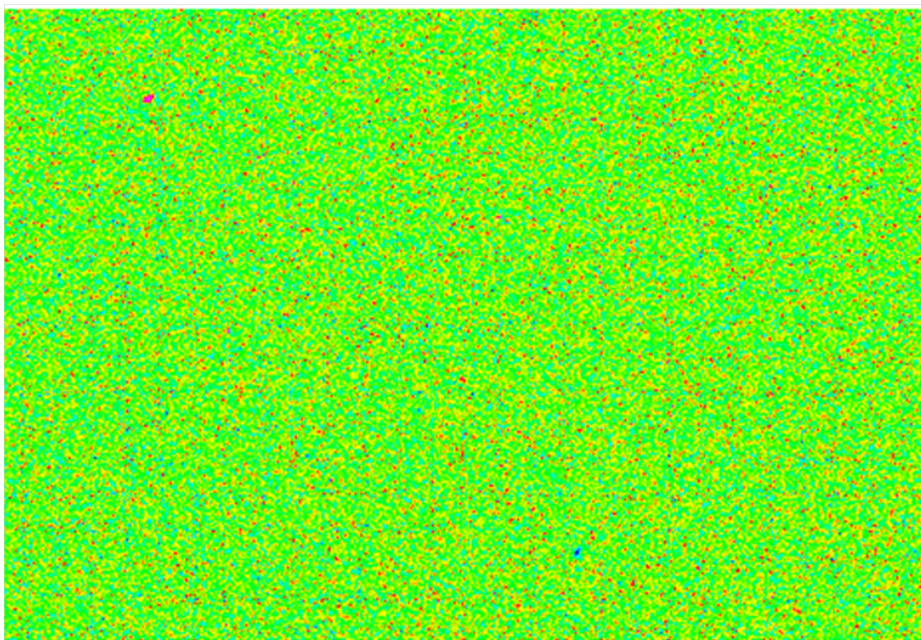


Figure 5.6: EPMA analysis showing the uniform distribution of Hf

5.2.5 Optimized CeO₂–HfO₂ mixed oxide thin film sensor performance

The optimized sensor film, CeO₂–HfO₂ (between 10–11% of Hf concentration) of thickness 220 nm was tested (by exposure to oxygen gas) at different temperatures ranging

between 300 to 400°C at 50°C intervals to identify the suitable operating temperatures. The sensor film could sense oxygen gas at all the three operating temperatures of 300, 350 and 400°C. It was observed that as the operating temperature decreased from 400 to 300°C, there was a slight increase in the response and recovery times from 8 s and 12 s to 10 s and 15 s respectively. All the reported CeO₂ oxygen sensors have been operated at very high temperatures of >600°C. As reported in Chapter 4, a CeO₂ oxygen sensor was developed that operates at a low temperature of 400°C; however, the sensor did not respond below 400°C because of very high resistance of the sensing film in the order of GΩ (10⁹Ω). The addition of HfO₂ to CeO₂ altered the structural and surface properties of the CeO₂ thin films, thereby leading to a reduction in the resistance values from 10⁹ to 10⁷ Ω. Hence, there was an improvement in the sensor performance in terms of sensitivity, response and recovery times. The films were also able to sense oxygen gas at a relatively low temperature of 300°C.

Fig. 5.7 illustrates repeatability of the sensor when subjected to identical gas concentrations of 100% indicating that the sensor can recover fairly well. A maximum sensitivity of 15 for oxygen concentration of 10,000 ppm at 400°C temperature was observed.

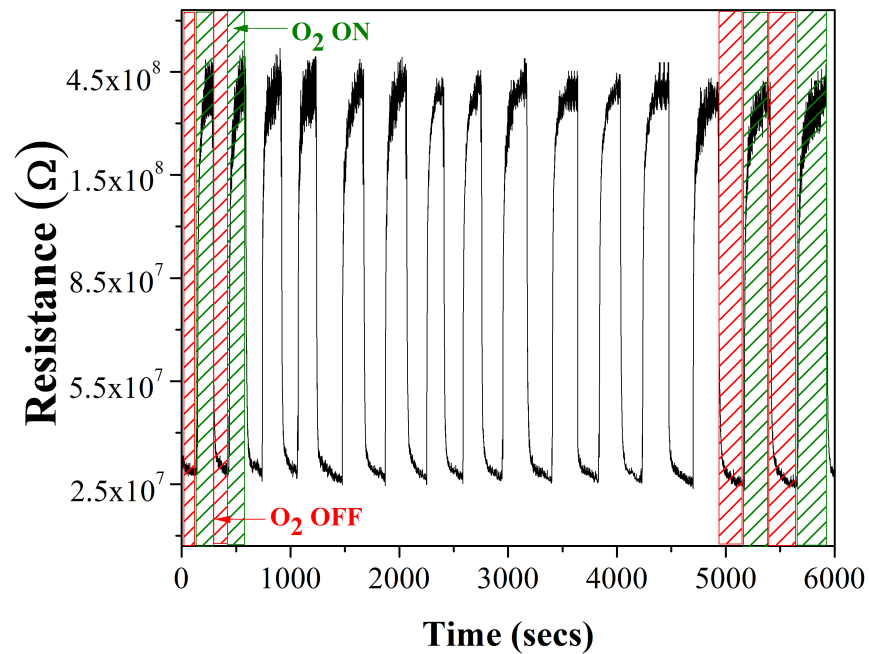


Figure 5.7: Response of the 220 nm film for fixed concentration (100%) at an operating temperature of 400°C

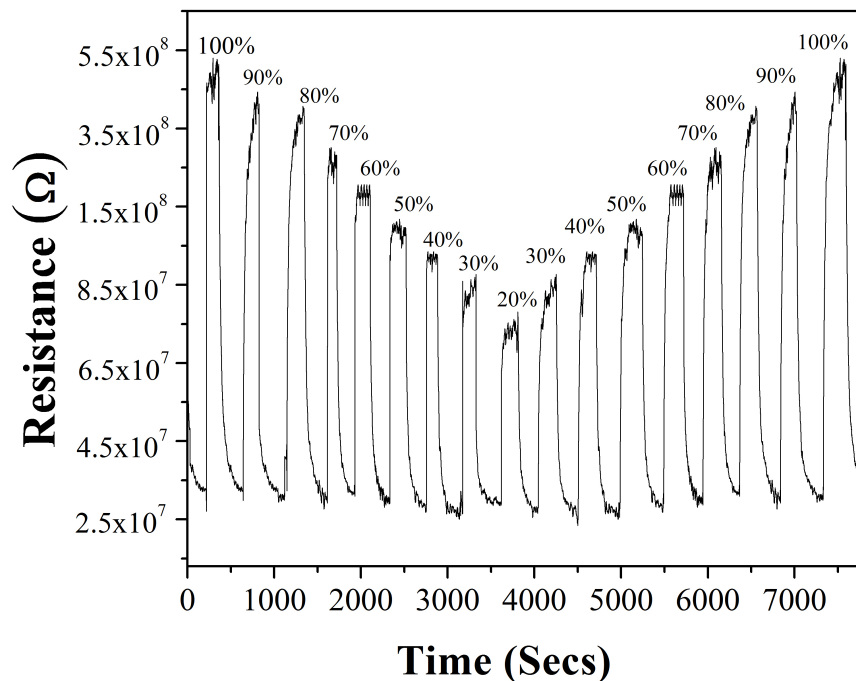


Figure 5.8: Dynamic response of the 220 nm film at an operating temperature of 400°C

Fig. 5.8 shows the dynamic response of the 220 nm $\text{CeO}_2\text{-HfO}_2$ thin film sensor at an operating temperature of 400°C. The sensor was exposed to pure N_2 followed by successive oxygen gas pulses of 100%, 90%, 80%, 70%, 60% upto 20%. From Fig. 5.8, it is evident that the sensor response increased with an increase in oxygen concentration and could even sense at low oxygen levels of 20%. Not much drift was observed in the baseline resistance when subjected to increasing and decreasing concentrations (Fig. 5.8). This clearly indicates that the oxygen vacancies on the reduced mixed oxide surface do not affect the stability and reproducibility of the sensors.

5.3 Conclusions

A novel technique was used for the synthesis $\text{CeO}_2\text{-HfO}_2$ mixed oxide thin films using RF sputtering. The mixed oxide films showed better sensing performance in comparison with pure CeO_2 films. The Hf atomic concentration was controlled using the size and number of HfO_2 pellets to achieve the best sensing performance. The characteristics and sensing performance were evaluated using various characterization techniques such as TEM-EDS, FESEM-EDS, XPS and XRD. The EDS and XPS data indicated

that the Hf concentration increases with an increase in size as well as number of HfO₂ pellets. From the XRD and XPS data, it was understood and concluded that the best sensing characteristics of CeO₂-HfO₂ mixed oxide films with 10–11% atomic concentration of Hf can be attributed to the existence of the highly reactive plane (200) with the highest surface energy and strongly reduced surface with oxygen vacancy formation due to the presence of Ce³⁺ ions and HfO_x, x<2 on the surface of the mixed oxide film.

The sensor film (CeO₂-HfO₂) could sense oxygen gas even at low temperatures of <400°C; however, the response and recovery times were slightly higher.

The fabricated/optimized CeO₂-HfO₂ mixed oxide sensor showed excellent sensitivity (~15), response time (8 s) and recovery time (10 s) at low operating temperatures of 400°C compared to reported values in literature till date. The sensor's performance is reproducible without any drift in the base line resistance. This work may pave the path towards development of scalable oxygen sensors using mixed metal oxides.

Chapter 6

Design and Development of Microheaters with High Temperature Uniformity for Gas Sensors

6.1 Introduction

A sensing element such as a metal oxide film can sense the target gas with maximum sensitivity only at certain temperature, hence localized heating arrangement with good uniform temperature profile is very much necessary to realize the developed oxide thin films in a viable sensor technology. microheaters with appropriate design and the physical properties of heating element at that length scale will play crucial role in achieving uniform temperature profile in the desired area of the sensing element. Moreover, the design should be process compatible. In this chapter, the design, simulation, fabrication and testing of the microheaters will be discussed.

Conventional heaters with larger dimensions have high power consumption, long heating times and long cooling cycles. In contrast, microheater has a fast heating response as compared to the conventional heaters Hwang *et al.* (2011). However, the heating response time and cooling cycles depend on the heating element (material) and their physical dimensions (length, width and thickness) as well as their physical properties (resistance and thermal conductivity) at that length scale.

Microheaters or Micro-hotplates are high-temperature generators, with precise control, that can offer very high temperatures (in excess of 1000°C) depending on the heater material. It consists of a substrate on which a heating element is fabricated. Heating element is a thin conducting path made of a high resistive material which exhibits joule heating when a current is passed through it. The substrate distributes the heat of the heating element uniformly over its surface. Due to their low power consumption and short response time, microheaters have been extensively used in micro systems based gas sensors Moon *et al.* (2012), Liu *et al.* (2018) and Li *et al.* (2017).

Platinum has been extensively used as heater material in fabrication of microheaters mainly due to its stable temperature coefficient of resistance, tolerance of large current density, high melting temperature also exhibit high stability in temperature cycles Li *et al.* (2017), Akasaka *et al.* (2019) and Cardinali *et al.* (1997). The main advantage of platinum is that it is resist to oxidation even over 500°C Spannhake *et al.* (2006). Other than platinum, materials such as molybdenum Mele *et al.* (2012), titanium nitride (TiN) Creemer *et al.* (2008), polysilicon Laconte *et al.* (2004), platinum–tantalum (Pt–Ta) Maeder *et al.* (1998), Firebaugh *et al.* (1998) and Esch *et al.* (2000), are also used in fabrication of microheaters.

Microheaters happen to be the very important component in MEMS gas sensors since the sensitivity and selectivity of the gas sensing film is decided by the heater temperature. While integrated gas sensor aims at precision measurement of gas concentration, the operating temperature of the thin film sensor should be uniform. Highly non-uniform temperature profile gives rise to ambiguity of the operating temperature. It will also degrade the selectivity and sensitivity. Moreover, this is also the most power consuming part in gas sensors which is decided by the geometry of the heater.

6.2 Design and Electro Thermal Modeling of Microheaters

The aim of this design is to optimize the geometry shape of the microheater to achieve very good temperature uniformity and higher temperature throughout its surface. The temperature uniformity across heater structure can be increased by optimizing the space between the elements of heater.

Resistive microheaters generate heat by the inherent resistance of metal conductors

to electron flow. By controlling the voltage supplied to a resistor, a predictable amount of power in the form of heat energy per unit time can be emitted from the resistor. The Power (P) equation which relates conductor is :

$$P = \frac{V^2}{R} \quad (6.1)$$

where V is the applied voltage and R is the Resistance. The resistance of the heater with material properties and its geometry is given by :

$$R = \frac{\rho L}{A} \quad (6.2)$$

where ρ - resistivity (Ω/\square), L - Length, A - Cross sectional area of the conductor. Thermoresistive effects of the thin metal films can be considered advantageous to measure the temperature to a high degree of precision and linearity. The equation which relates the resistance and temperature for thin metal films is given by :

$$R_T = R_o[1 + \alpha_R(T - T_o)] \quad (6.3)$$

where R_T - Resistance measured at different Temperature, R_o - Resistance at Room Temperature T_o , α_R - Temperature Coefficient of Resistance (TCR) of the heater material and T - Measured Temperature in $^{\circ}\text{C}$.

$$R_T = \frac{\rho L}{WD}[1 + \alpha_R(T - T_o)] \quad (6.4)$$

For a conductive line made with material resistivity ρ , length L , width W and thickness D , the heater pattern can be tailored within the limits of the processing capabilities by variably reducing the line width of the pattern.

Modeling of micro-heating elements has been performed for years. COMSOL is the most convenient MEMS design tool used in the industry these days. It is an efficient integrated design environment that reduces design risk, speeds time-to-market and lowers the development costs. The simulation tool enables schematic-based structural modeling and detailed 3D multi-physics numerical analysis to support every MEMS application, such as automotive sensors, RF devices, optical MEMS, acoustics and micro fluidics Messina *et al.* (2007),Bechtold *et al.* (2004),Ali *et al.* (2008), Li *et al.* (2006), Udrea *et al.* (2001), Pike and Gardner (1997), Astie *et al.* (1998), Joy and Antony (2015), Elmi *et al.* (2006), Biró *et al.* (2014), Kumar *et al.* (2014), Noor *et al.*

(2014), Venkatesh *et al.* (2016) and Kwak *et al.* (2018).

The electric current density ' J ' is proportional to the electric field. Due to the electric current, there is resistive heating which is shown to be proportional to the square of magnitude of the electric current density ' J '. This is referred to as Joule heating. The Joule heating predefined multiphysics coupling combines a *Conductive Media DC application mode* from COMSOL Multiphysics with the *Heat Transfer Module*. The Joule heating model node in COMSOL uses the following heat equation for mathematical modeling of heat transfer in solids:

$$Q \propto |J|^2 \tag{6.5}$$

where Q is the amount of heat generated and J is the Current density in (A/m^2)

Correct design of microheater is an important aspect since this is the most power consuming part in any device it is integrated into. In the past, extensive research has been carried out to optimize the geometries of the microheater, and geometries such as square plate with central hole, meander, S-shape, fan shape, honey comb and double spiral are most commonly used geometries Singh and Mohan (2005), Velmathi *et al.* (2010), Sujatha *et al.* (2012), Bhowmick *et al.* (2017), and Lee *et al.* (2003). However not much work on shapes and patterns have been reported. The Square plate with central hole structure suffers from undistributed hot spots near the hole and it also consumes more power Singh and Mohan (2005). Though single meander is extensively studied due to its simple geometry, it consumes high power and hot spots were observed at very high temperatures leading to large temperature variations across the hot plate Lee *et al.* (2003). S-shaped heaters will be suitable only for smaller dimension sensing films and they suffer from high stress due to thermal expansion Je and Lee (2014) and Velmathi (2017). Though Fan shaped heater consumes less power, it suffers from process compatibility Bhatt and Arora (2014).

Recently, six commonly used structures (Square plate with center hole, Honey comb structure, Fan shape, Meander structure, Double Spiral shape and S-Shape) of microheaters were simulated and fabricated and it was reported that double spiral and fan shape consumes less power Velmathi *et al.* (2010). However, as seen from the simulation results in Fig. 6.1, though the dimension of the heaters are $500\mu m \times 500\mu m$, the temperature is uniformly distributed only for a smaller area of around $200\mu m \times 200\mu m$. This clearly indicates that the entire heater area is not fully utilized due to non-uniformity of temperature. This will affect the sensor's performance.

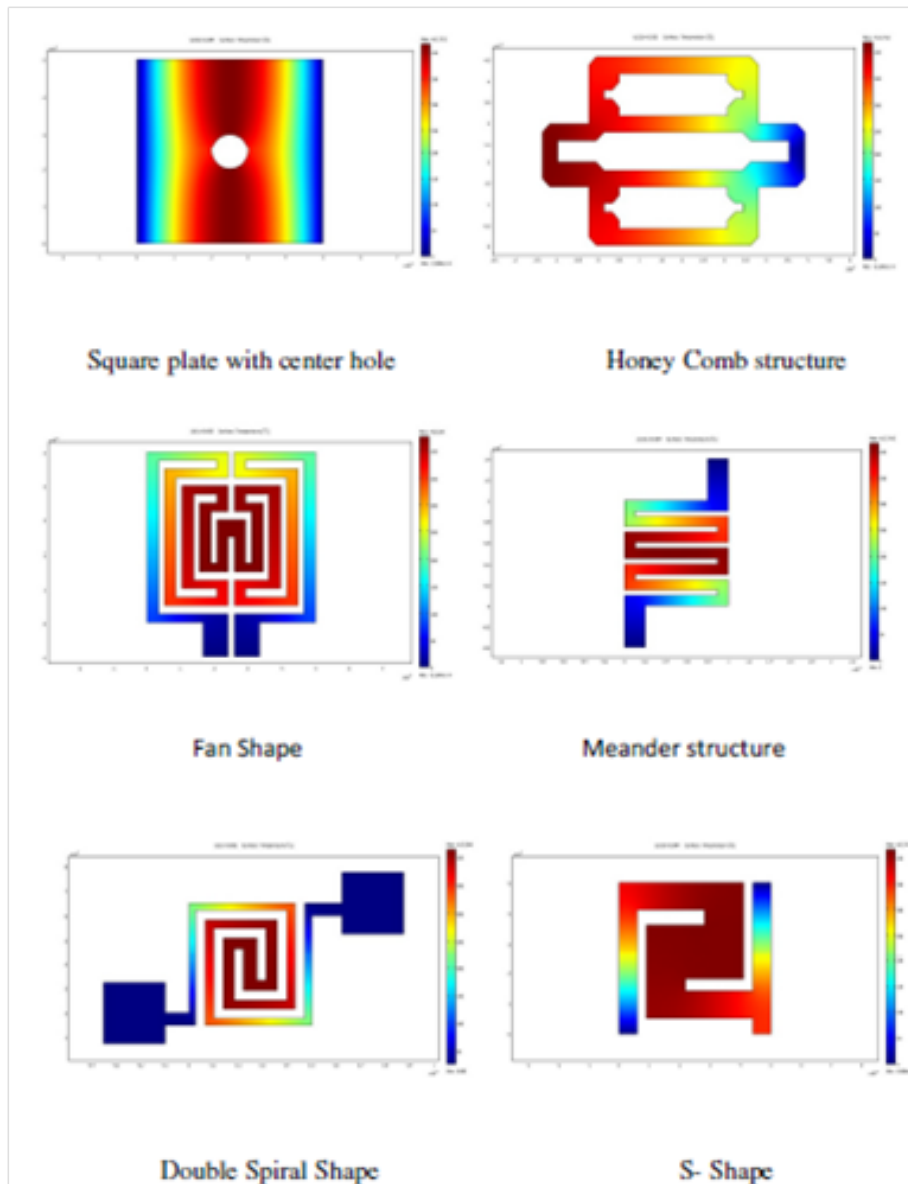


Figure 6.1: Simulated results of commonly used heater structures for $500\mu m \times 500\mu m$ Velmathi *et al.* (2010).

With this in background, the design, simulation and fabrication of microheaters with focus on improving the temperature uniformity is attempted and reported in this chapter.

The uniformity in temperature profile can be improved by increasing the resistance of the heating element. Usually the heating profile is modified by increasing the length of these elements. However the temperature profile can also be improved by modifying

the area of the heater. In this work, the area of the heater is optimized in order to increase the resistance by adopting novel designs / geometries.

The single meander shape was taken as a reference design Velmathi *et al.* (2010), Singh and Mohan (2005) and several modifications were done on this structure to cover more area under heat. After several iterations and optimizations, a novel designs namely Perforated Type 1 and Type 2 microheaters have been developed with an array of connectors placed at different points as shown in Fig. 6.2. This was done in order to improve the heating and maximize the current density over the entire structure which leads to higher heat generation. Thermal insulation was provided to achieve an improved temperature profile.

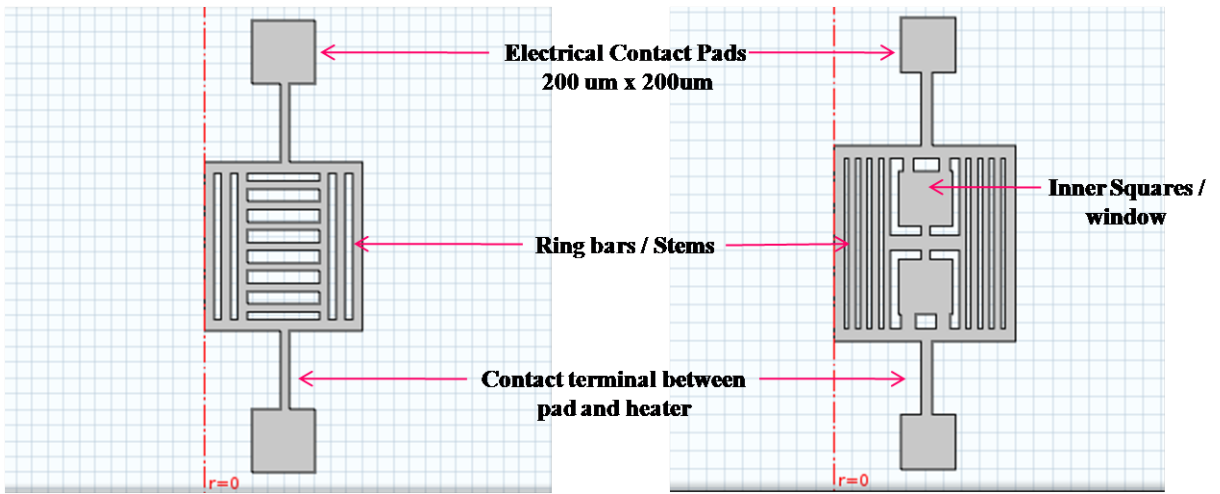


Figure 6.2: Perforated Type 1 and Type 2 microheater designs of $500\mu\text{m} \times 500\mu\text{m}$ dimension.

6.2.1 Meshing in COMSOL

A mesh is a partition of the geometry model into small units of simple shapes. In COMSOL Multiphysics a default mesh could be created which are triangular in shape for a 2D simulation and tetrahedral if the simulation is 3D. A mapped mesh also could be created for user defined element shapes.

In both the cases some parameters mentioned below could be adjusted:

- Predefined mesh sizes: It is possible to choose the size of the mesh for each sub-domain, boundary or edge in the model. More important parts can be adjusted to smaller mesh sizes.

- Scale geometry : For this parameter, the scale factor in each direction (x, y, z) is adjustable. Scale factors are used to generate anisotropic meshes, they are useful when there is large aspect ratio in the geometry, like cases where x, y parameters include micrometers and z parameter is in nanometer scale.

Microheater geometry chosen in this report is $500\mu m \times 500\mu m \times 100nm$

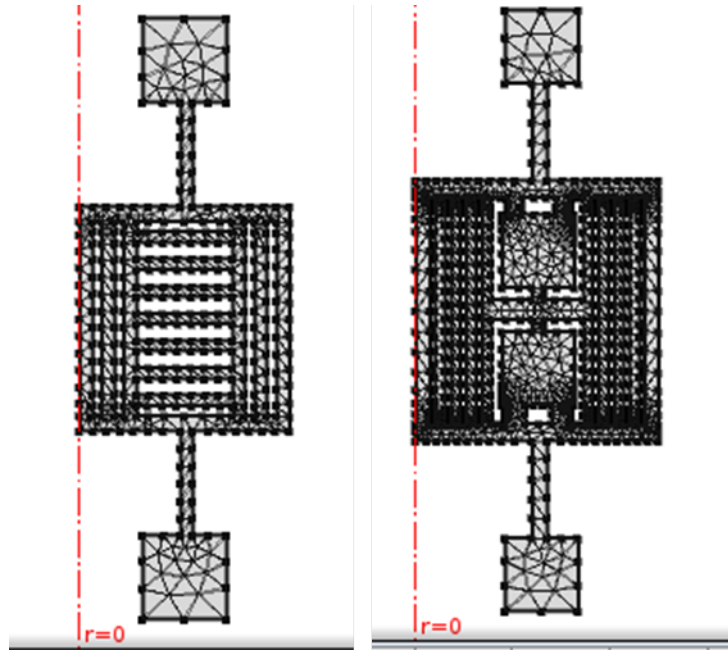


Figure 6.3: Meshing of Perforated Type 1 and Type 2 microheater.

6.2.2 Simulation Results

The microheaters are modeled for the area of $500\mu m \times 500\mu m$ and a thickness of $100nm$. The thermal profile of each heater geometry to produce around $400^{\circ}C$ is shown in Fig. 6.4 and 6.5. The temperature profile in both the designs have shown excellent temperature uniformity throughout the entire area of the heater.

Both types of microheaters are fabricated and characterized thermally & electrically and their results are compared in order to validate the design strategy and simulations. These microheaters have been fabricated at Center for Nano Science and Engineering (CeNSE), Indian Institute of Science (IISc), INDIA.

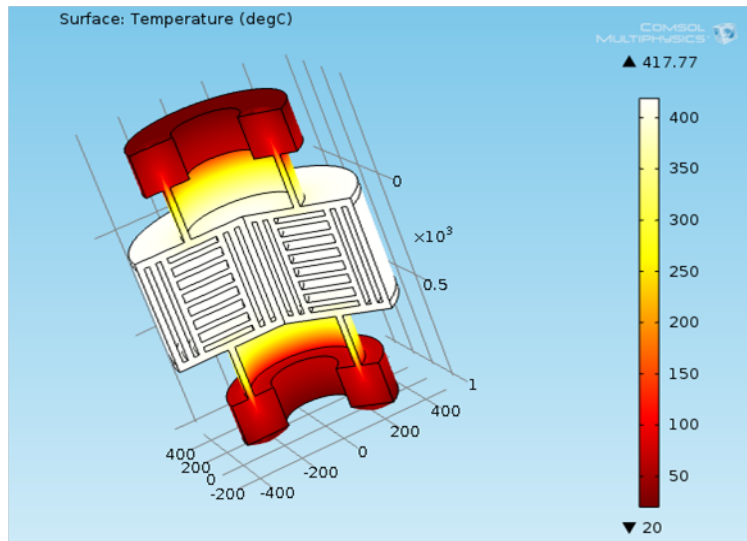


Figure 6.4: Temperature Profile of Perforated Type 1 microheater.

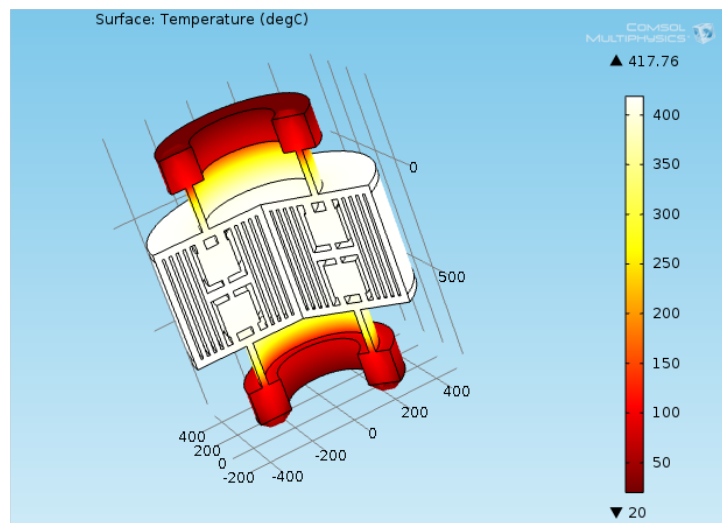


Figure 6.5: Temperature Profile of Perforated Type 2 microheater.

6.3 Fabrication of Microheaters

Schematic of microheater fabrication process is shown in Fig. 6.6. Microheater fabrication consists of the following steps:

1. Wafer cleaning
2. SiO₂ by PECVD
3. Lithography

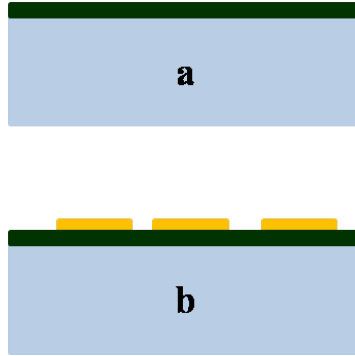


Figure 6.6: Microheater Fabrication :- (a): Deposition of 1 micron PECVD SiO₂ on RCA cleaned Si Wafer, (b): Microheater patterning and lift-off (Ti/Pt - 10/100 nm thickness).

4. Pt deposition (by sputtering) and lift-off

Si wafer (one quarter of 3") was cleaned with RCA-1 and RCA-2 solutions. Then 1 μ m oxide layer is grown using PECVD Technique on top of the polished surface of the wafer. Photoresist AZ5214E is applied using a spin coater. An array (16 \times 16) of heater patterns (as shown in Fig. 6.7) are directly written upon the photoresist using Optical Lithography technique (Tool: Heidelberg UPG 501) which is also called as Laser / LED writing. Subsequently the heater patterns are developed in MF26A developer solution and rinsed with DI water followed by nitrogen drying. This was followed by deposition of Ti/Pt - 10/100nm by sputtering technique. Ti was used as an adhesion layer. Finally the sacrificial photoresist was removed using lift-off technique.

6.4 Microheater Characterization

The fabricated devices are visually inspected using optical microscope (Fig. 6.8), to check short circuits, cracks in the wafer or in the microheaters, and overall quality. Also, a color CCD equipped with 100x magnification lenses was used via a desktop PC to inspect the wafers. Any platinum left on the edges of the wafers was removed to prevent short circuits, and then a continuity test was performed.

The fabricated microheaters were also inspected by using high resolution SEM. This was done in order to validate the physical dimensions, finishing at the surface and the edges. The SEM images of the fabricated microheaters shown in Fig. 6.9

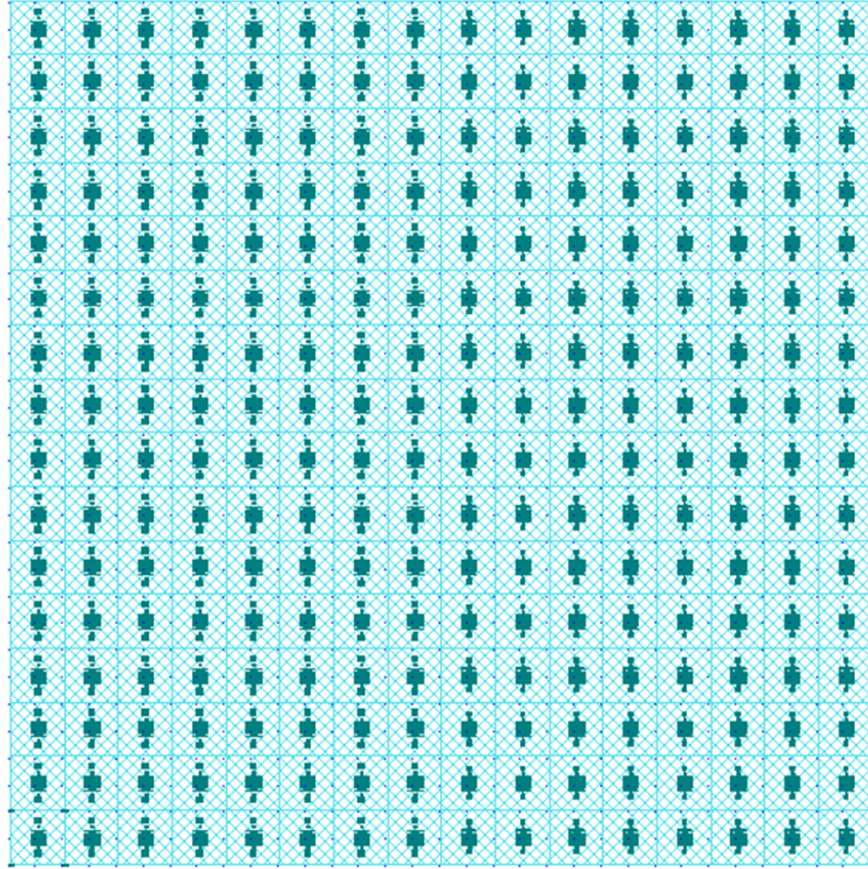


Figure 6.7: The .cif file consisting of array of heater patterns created by direct writing.



Figure 6.8: Visual inspection of fabricated microheaters using optical microscope.

clearly indicate that there is no deviation w.r.t the original design.

The fabricated microheaters are characterized for their thermal and electrical prop-

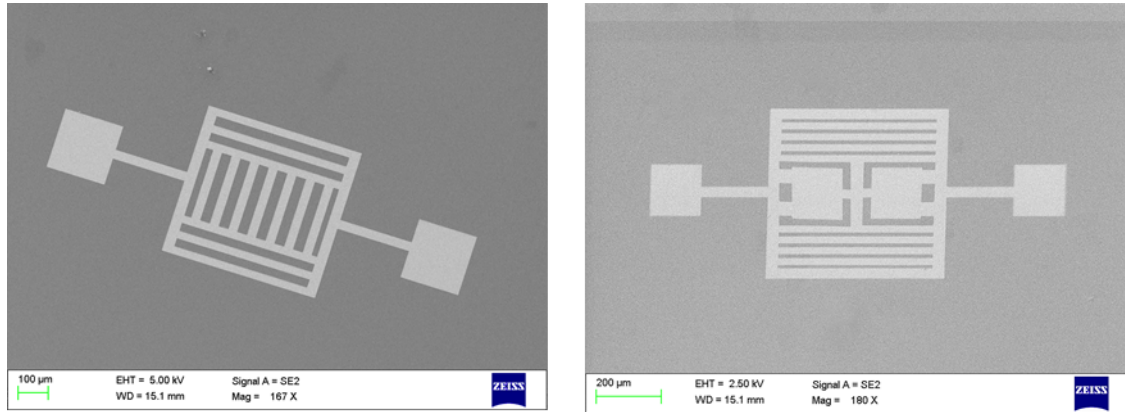


Figure 6.9: SEM Images of fabricated microheater patterns.

erties to ascertain the temperature uniformity and power consumption. To perform this, firstly the die is separated from the array of devices by using the Automatic Dicing Machine (DAD321 Disco Wafer Dicer). The die is then attached to the IC header with the help of non-conductive adhesive. The electrical contacts are obtained by connecting the contact pads using of the wire bonding (HB16 TPT Wirebonder) technique. Microheaters are wired bonded using 25μ thick gold wire. Keithley source meter is used for the measurement of electric parameters and FLIR SC5200 infrared camera is used for thermal imaging.

6.4.1 Thermal Images of the Microheater Patterns

The thermal images of the microheaters are captured by IR camera - FLIR SC 5200. The microheater is placed on the test bench of the thermal imaging camera and the electrical contacts of the heater are connected to the probes of the source meter for driving current or voltage. After setting up adequate capturing parameters such as emissivity and number of frames, the thermal images are acquired and shown in Fig. 6.10 to Fig.6.12.

Fig. 6.10 shows the FLIR image of the two heaters. From Figures 6.11 to 6.12, it is clear that the heater elements exhibits uniform temperature throughout the entire area as observed in the simulated results. Even at very high temperatures, the fabricated structures showed high stability and without any hot spots.

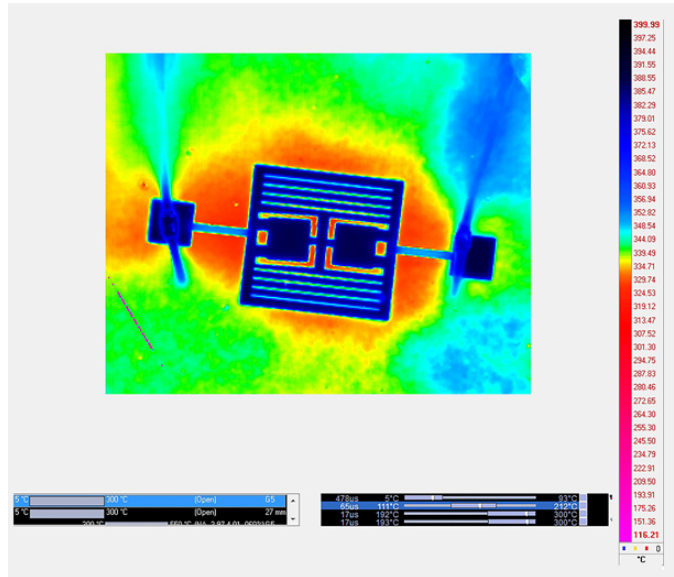


Figure 6.12: FLIR thermal image of Perforated Type 2 microheater showing the uniform temperature distribution along the heater.

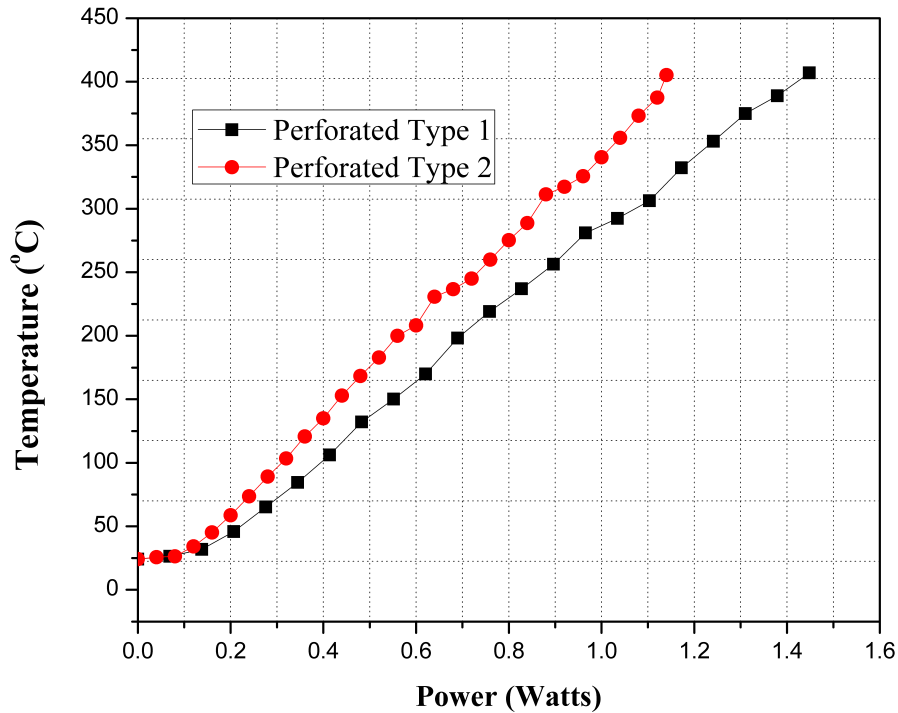


Figure 6.13: Temperature-Power curve for comparison of two types of heaters.

perature of around 400°C, whereas the Perforated Type 1 heater consumes 1.44 watts to reach the same temperature. Velmathi (2015) designed and fabricated a membrane

based double spiral shape heater which consumed 1.8 W to reach 400°C. Yoon *et al.* (2002) have used a microheater of spiral groove of size $280\mu m \times 280\mu m$ for polymerase chain reaction (PCR) application. Their results indicate that the power consumed is 1.34 W for a temperature rise to 90°C. The results presented in our work are better than those presented in the literature. The excellent temperature uniformity and low power consumption can be attributed to the novel designing technique obtained by optimizing the area of the heater.

The power consumption could be further reduced by micromachining the area below the heater. This is done by removing the Si underneath the heater area. However this needs additional process steps namely patterning the area to be etched and etching of Si wafer by wet or dry etch technique.

6.5 Integrated Gas Sensor (Microheater + Sensing Element)

The microheater fabrication process was explained in Section 6.3. Steps (a) and (b) shown in Fig. 6.6 followed for fabrication of microheater will remain same. The subsequent fabrication steps involved in Integrated Gas Sensor are shown in Fig. 6.14 and are discussed below.

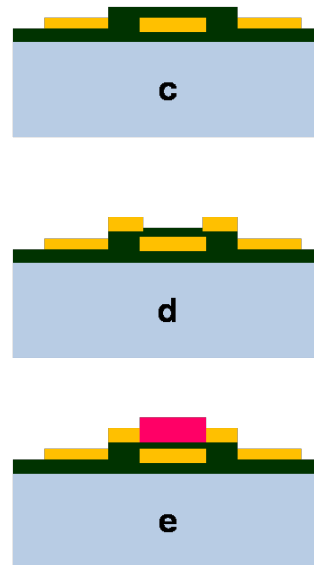


Figure 6.14: Fabrication Steps of Integrated Oxygen Gas Sensor (c) Deposition of SiO_2 , (d) Deposition of Electrodes (Ti/Pt) (e) Sensor Film Deposition.

As shown in step (c) of 6.14, a thin, $1\mu\text{m}$ film of SiO_2 is deposited on microheaters using PECVD technique. This layer acts as a barrier layer or an electrical insulator between the microheaters and sensing electrodes. Since SiO_2 is required only on top of the microheater, this area is masked (by photoresist) and SiO_2 is etched from the rest (unmasked) of the areas by Reactive Ion Etching (RIE). Later the Ti/Pt interdigitated sensing electrodes (IDE) of thickness 10/50 nm is deposited by sputtering method which is carried out by lift-off technique after necessary patterning (as shown in 6.14 step d). Finally, as shown in 6.14 step e, the sensor film ($\text{CeO}_2 + \text{HfO}_2$) is deposited by sputtering technique (as discussed in Chapter 5) on top of the electrodes with necessary masking (to protect the other areas).

The fabricated integrated gas sensor is shown in Fig. 6.15(a). Individual dies (as shown in Fig. 6.15(b)) are separated after proper dicing. The contact pads (microheater and IDE's) of the fabricated gas sensor of different patterns are then attached on the header with suitable wire bonding techniques. The prototype of the integrated sensor mounted on two different headers (TO5 and Plastic) are shown in Fig. 6.15 (c and d).

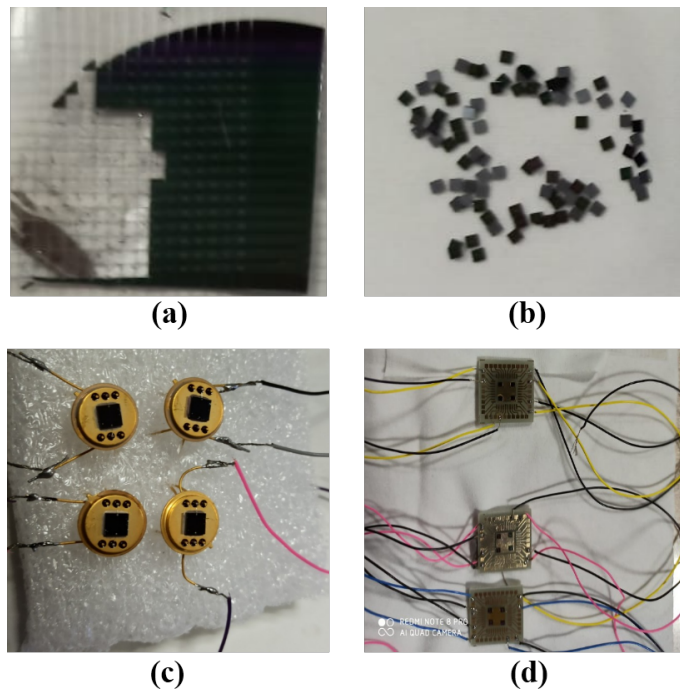


Figure 6.15: Integrated gas sensor (a) Wafer level, (b) Die level, (c) Sensor mounted on TO5 header and (d) Sensor mounted on plastic header

The gas sensing measurements for sensing oxygen gas were carried out using the sensor developed. The response and recovery time for these sensors were found to be of 13 and 20 seconds respectively which is in good agreement to the results discussed in Chapter 5. The gas sensing curve performed on 100% oxygen gas is shown in Fig. 6.16. The gas sensing was carried out for 1.5 hours duration and the results were found to be reproducible with no drift in the baseline resistance.

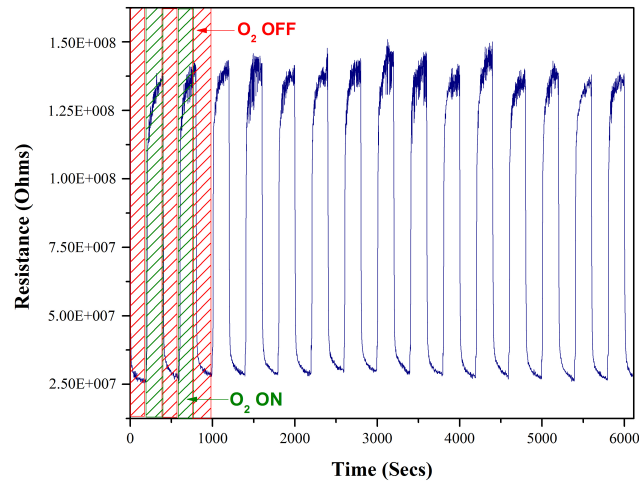


Figure 6.16: Gas sensing results on Integrated Sensor.

6.6 Conclusion

Microheaters play a crucial role in MEMS gas sensor technology. Several microheater designs have been studied and new heater patterns with excellent temperature uniformity and low power consumption have been developed.

Two different geometrical structures namely Perforated Type 1 and Type 2 Platinum microheaters of dimension $500\mu m \times 500\mu m$ were designed and analyzed using FEM based software COMSOL. The simulated results show the temperature being distributed uniformly across the entire structure in both the designs.

The designed microheaters were fabricated and characterized thermally and electrically. The results showed excellent temperature uniformity in the entire heater area and the power consumed to raise the temperature to 400°C is nearly between 1.14 to 1.44 W which was considerably lower than that reported in the literature. This can be attributed to the novel microheater designs obtained by optimizing the area of the heater.

The fabricated heaters were integrated into a gas sensor and the device was tested for oxygen gas. The sensing results (response time of 13 seconds and recovery time of 20 seconds) were found to be in good agreement with the results obtained using a bulk or conventional heater (as discussed in Chapter 5).

Apart from gas sensor applications, microheaters with high temperature uniformity, low power and high thermal stability find very wide applications, such as, in shape memory alloy microactuators, heater actuated cantilevers and BioMEMS applications where precise temperature control is one of the important requirements.

Chapter 7

Design of Wide Range Readout Circuit

7.1 Gas Sensor Readout circuit Design

Readout circuits are circuits used to convert the sensed signal, such as voltage, current, resistance etc. or changes in it into a more convenient form of the same or different type of signal for further processing. This chapter presents a brief review on resistance readout interface circuits reported in the literature and explains the requirements of the readout circuit. The chapter also presents a highly efficient readout circuit designed for measurement of very high resistances.

7.1.1 Interface circuit requirements and state of art

An intelligent design and integration of the electronic circuitry (for drive, signal conditioning/compensation, and readout) with the gas sensing element can mitigate some of the significant issues inherent in solid-state gas sensors, such as strong temperature and humidity dependence, signal drift, aging, poisoning, and weak selectivity.

There are two possible ways of implementing smart gas sensors, viz.,

1. Hybrid approach and
2. Monolithic approach

Hybrid Approach

In this approach, the gas sensor and the interface circuitry form two different chips, as

shown in Fig. 7.1a and these two can come from different foundries and hence have the advantage of fewer thermal and material design constraints. Also, in this approach, the electronic circuit dies can be reused even if there is a problem with the sensing chip. However, the parasitic capacitance/resistance arising because of the interconnect between the chips is clearly larger, less predictable and less repeatable than with the monolithic approach. Furthermore, there is the additional cost of fabricating, interconnecting and mounting two chips (with a larger area) into a single package.

Monolithic Approach

In this approach, both the sensors and the interface electronics are on the same silicon chip as shown in Fig. 7.1b and this approach benefits from a well established microelectronics process that leads to a reliable and reproducible performance with less parasitic effect. However, the gas sensing component can only be made with foundry provided materials and a defect in the sensing element will result in the failure of the whole integrated chip even if the readout circuitry is working properly. Hence the cost of device failure is significantly higher.

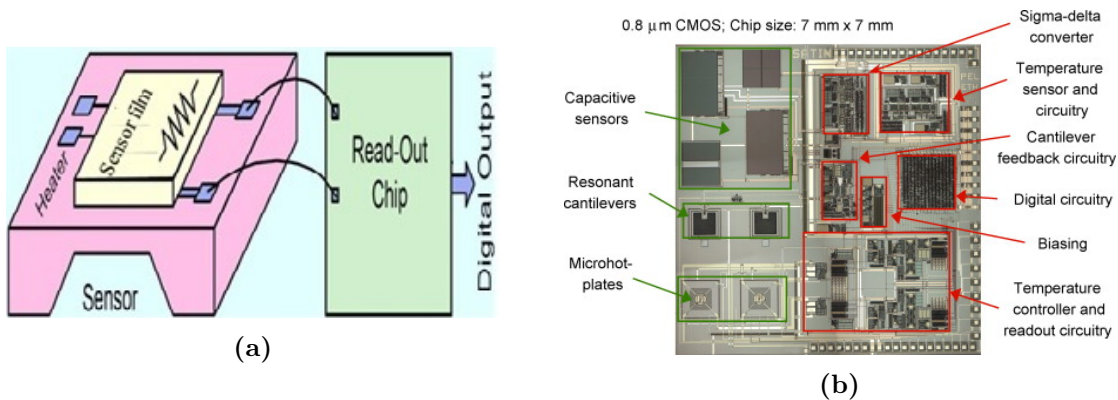


Figure 7.1: Gas Sensing film integrated with the Readout Chip in (a) Hybrid Approach and (b) Monolithic Approach Li *et al.* (2007)

7.1.2 Interface circuit requirements

All gas sensors require a sufficiently fast interface circuitry in order to manage transient data acquisition and limiting the signal distortion to minimum. For gas monitoring applications, the range of resistance values to be measured is significantly wide. In order to detect a variety of gases of interest with enough accuracy usually in the order

of tens of parts per million (ppm), it is important to measure the sensor resistance value (R_{sens}) with a precision better than 1% (Malcovati *et al.* (1996)). Furthermore, considering the state of the art in oxide sensors manufacturing Martinelli *et al.* (2004), the sensor resistance values may vary widely because of the effect of three typical sensor response components listed below. A wide-range of readout performance is also needed (Barrettino *et al.* (2004)) because the sensor resistance value, (R_{sens}), may vary by several orders of magnitude (decades when expressed in dB) due to the combination of the following three variable components Burresti *et al.* (2005), Capone and Siciliano (2004), Far *et al.* (2008).

- The baseline value R_0 , which typically depends on the fabrication technique.
- The deviation from the baseline ΔR_0 , due to technological and aging spread as well as temperature.
- The resistance variation ΔR_{GAS} , which depends on gas concentration and which is negative for most gas types (its value can be as large as a couple of decades below the baseline value).

Thus the resistance value can be written as,

$$R_{sens} = R_0 + \Delta R_0 - \Delta R_{GAS} \quad (7.1)$$

Resistance measurements are divided into three types- low resistance measurement, medium resistance measurement and high resistance measurement. If the resistance measurement is from a few milli ohms to micro ohms, then it is considered as a low resistance measurement. Medium Resistance measurements are from 1Ω to $100\text{K}\Omega$. Potentiometers, thermistors, etc., fall in this category. Very high resistance measurements are those that lie in the range $100\text{K}\Omega$ to more than $100\text{M}\Omega$.

7.1.3 State of art of interface circuits

In chemoresistive sensors the presence of volatile compounds change the resistance of the sensing element. Interface circuits for these sensors are relatively simple since they involve measuring the change in resistance. Two types of resistance measurement circuits are commonly used: voltage dividers and Wheatstone bridges.

7.1.3.1 Potential divider circuit

Early work by Shurmer and Gardner (1992) on odor discrimination with an electronic nose made use of the potential divider methodology, shown in Fig. 7.2, for the interfacing of chemoresistors.

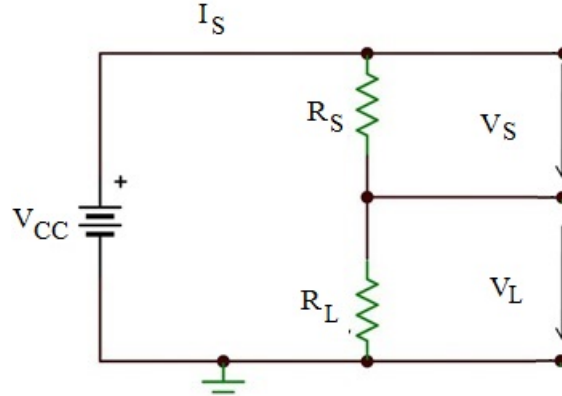


Figure 7.2: Potential divider circuit (Shurmer and Gardner (1992))

The resistive sensor R_S is placed in series with a load resistor R_L and connected to a reference voltage V_{CC} . The current through the sensitive element and load resistance is given by,

$$I_S = \frac{V_{CC}}{R_S + R_L} \quad (7.2)$$

Any changes in the resistance of sensor are measured as voltage across the sensor (V_S) or the load resistor (V_L). For convenience, the voltage across the load resistor will be used since it is a single-ended measurement and the subsequent derivation becomes simpler. The resulting output voltage is given by:

$$V_L = I_S R_L = \frac{V_{CC}}{R_S + R_L} R_L \quad (7.3)$$

Although voltage divider method is recommended by several metal-oxide sensor manufacturers, it has several shortcomings. Firstly, the relationship between the sensor resistance R_S and the output voltage V_L is nonlinear since the current I_S is inversely proportional to the total resistance and also depends on the varying sensor resistance. Secondly, and most importantly, the circuit is only appropriate for measuring large resistance changes, such as those typical of metal oxide sensors. Conducting polymer chemoresistors have sensitivities one order of magnitude lower than the metal ox-

ide sensors Shurmer and Gardner (1992) and hence require the use of more accurate measurement circuits such as Wheatstone bridges.

7.1.3.2 The Wheatstone Bridge

When the resistance changes to be measured are small relative to the baseline resistance of the sensor, the information in the output voltage will consist of small fluctuations superimposed on a large offset voltage. Although the sensitivity can be boosted with a gain stage, the problem remains because of the fact that a large portion of the dynamic range of the Analog to Digital Conversion (ADC) will be wasted in measuring the offset voltage. One solution for measuring small resistance changes is to subtract the offset voltage with a second voltage divider, as shown in Fig. 7.3.

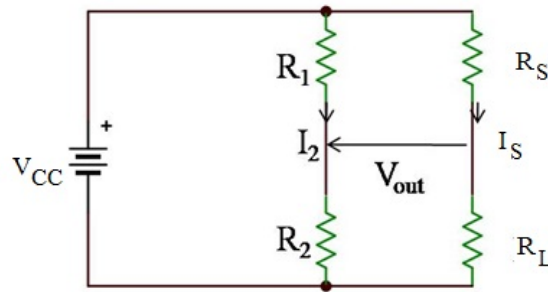


Figure 7.3: Wheatstone circuit (Shurmer and Gardner (1992))

The differential voltage in the bridge is given by :

$$V_{Out} = R_L I_S - R_2 I_2 = R_L \frac{V_{CC}}{R_S + R_L} - R_2 \frac{V_{CC}}{R_1 + R_2} = V_{CC} \left(\frac{R_L}{R_S + R_L} - \frac{R_2}{R_1 + R_2} \right) \quad (7.4)$$

Maximum sensitivity for the Wheatstone bridge is obtained by choosing resistors R_1 , R_2 and R_L equal to the sensor baseline resistance. This measurement approach is known as a deflection method, because the sensor response is measured as a differential voltage when the bridge becomes unbalanced. An alternative approach, known as the null method, consists of adjusting the resistors R_1 and R_2 to cancel the differential voltage V_{OUT} . The sensor resistance is then obtained from the balance condition:

$$V_{Out} = 0 \leftrightarrow \frac{R_1}{R_2} = \frac{R_S}{R_L} \rightarrow R_S = R_L \frac{R_1}{R_2} \quad (7.5)$$

The main advantage of the Wheatstone bridge is that it affords higher amplification gains since the offset voltage has already been removed. The Wheatstone bridge technique has been employed in the past by Cole *et al.* (1999) and Gardner *et al.* (1998) as a front end interfacing circuit for conducting polymer chemoresistors. Arshak *et al.* (2003) observed the output to be nonlinear with large resistance swing. Leung and Wilson (2005) also designed a Wheatstone bridge configuration for polymer chemoresistive sensors, where they used an active and another identical less-sensitive polymer layer as two arms of a Wheatstone bridge. The result is a differential signal between the baseline and sensing films. This signal is first amplified, through a differential amplifier, and then compared with a saw tooth signal to perform Pulse Width Modulator signal conversion (as shown in Fig. 7.4).

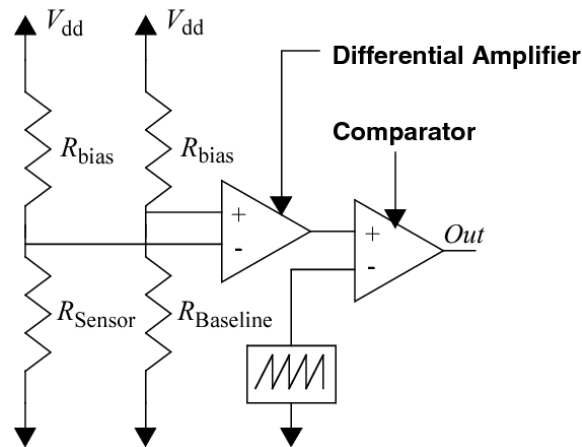


Figure 7.4: Chemiresistance to digital conversion circuit scheme (Leung and Wilson (2005))

Wheatstone Bridge cannot be used for low resistance measurements because the output voltage will be affected by the resistance of wire and leads. For example, if the resistance to be measured is 1Ω and the lead resistance is 0.02Ω , there is already an error of 2% which will increase and gets added in every step of calculation.

For precise measurement of medium resistance, Wheatstone bridge is commonly used.

When the bridge is in balanced condition, no current flows through the galvanometer connected across V_{out} terminals in Fig. 7.3. The change in current will be very low for high resistance measurements. Hence the galvanometer needs to be very sensitive to sense low currents, otherwise the reading will be zero even if there is a current

flowing through the galvanometer owing to an unbalanced bridge.

Several design techniques and selection of components can improve the performance and accuracy of the pico-ammeter. In this regard, IC selection is an important part prior to designing ultra-low current measurement circuits.

7.2 Developed Readout Circuit structure

The schematic of the designed 3-stage op-amp based readout circuit is shown in Fig 7.5. The three stages are namely : constant current source, buffer amplifier and feedback amplifier. The 3 amplifier configuration is a constant current source used to measure the change in resistance when a constant current is pumped and voltage is measured across the resistance under test. The op-amp's (OP07) used have very high input impedance, very low input bias current and very low input capacitance. Since the change of resistance to be measured is too high, the constant current to be fed will be in the order of nano amps.

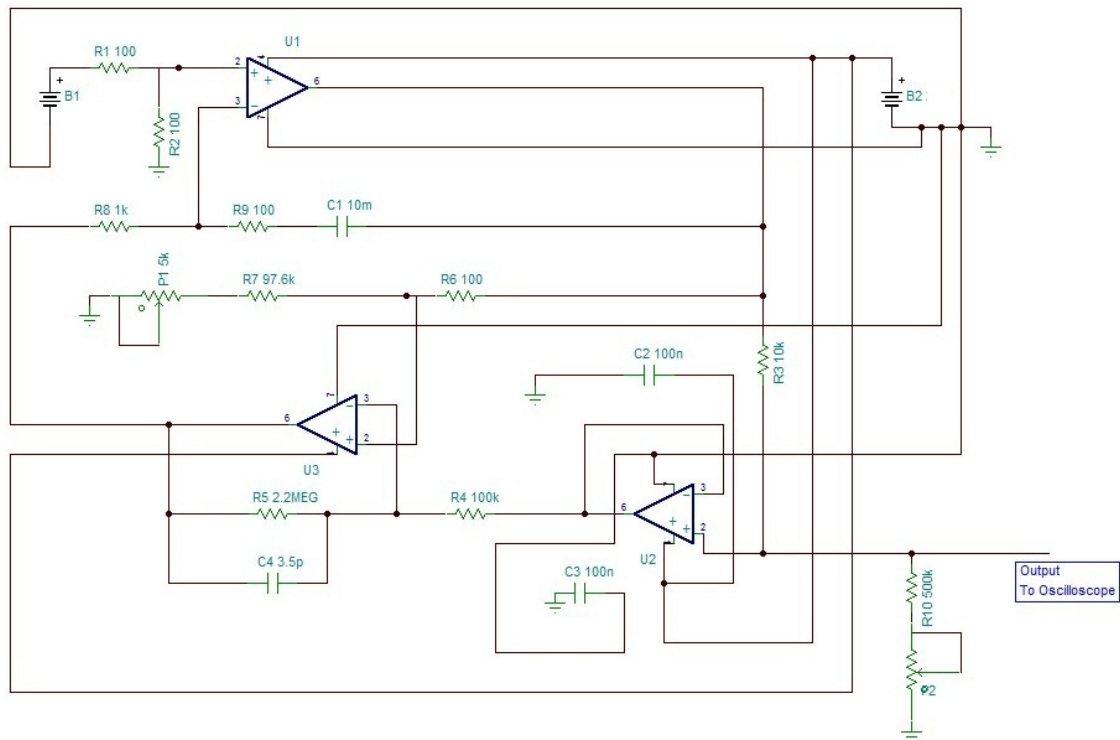


Figure 7.5: Schematic of the designed readout circuit

In the first stage, a ripple free voltage of $\pm 10V$ is fed to the input amplifier U1 which works as non-inverting amplifier. This stage acts as a voltage to current converter which gives a constant current corresponding to the input voltage applied.

The second stage is a *buffer* between the *load* and the *feedback* amplifier. This *buffer* has a very high input resistance which does not disturb the load current but the feedback voltage is transferred to the next stage. The voltage across the load generated due to flow of constant current is measured by amplifier U2. The amplifier U2 is designed such that the feedback has a trimming facility to precisely set constant current and to control it for variations in the load. The output of amplifier U2 is also connected to an amplifier which displays the change in voltage to show the change in resistance.

The feedback amplifier (U3) generates the error voltage developed across the load due to change in resistance. This error Voltage is fed to the first Stage to maintain current constant.

The schematic of the designed readout circuit is simulated using Proteus 8 Professional Simulation Software. As the resistance of sensor element changes, the corresponding output voltage also changes in real-time.

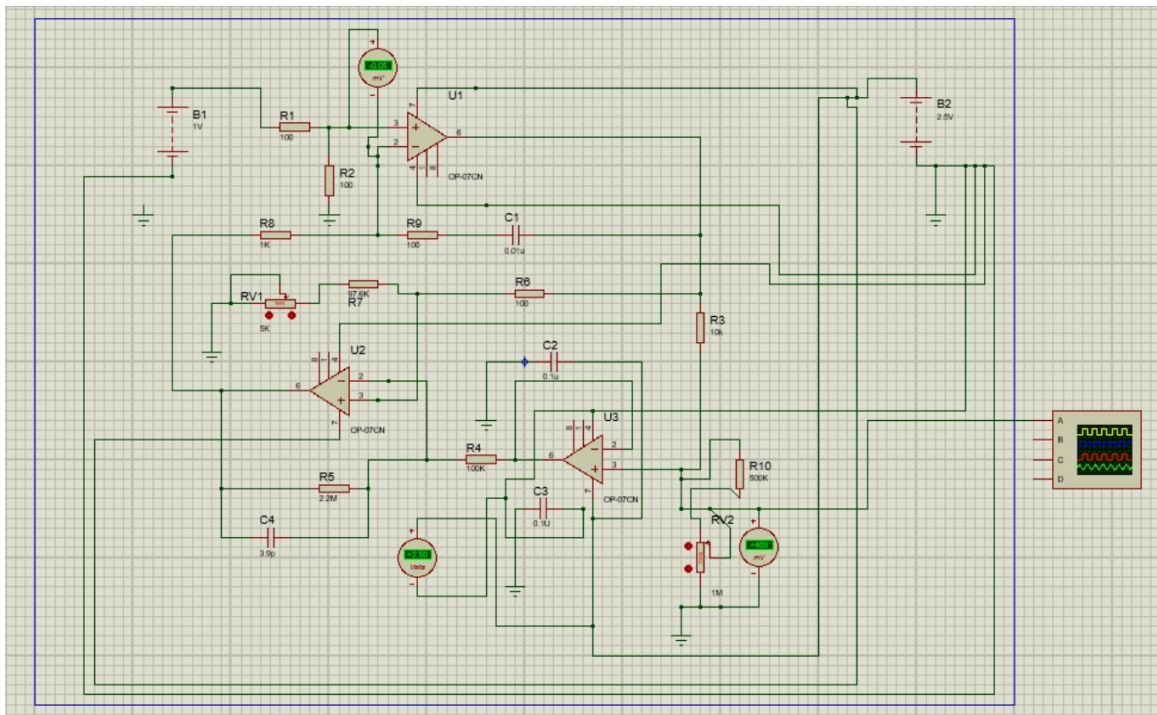


Figure 7.6: Schematic of Gas Sensor readout circuit

Chapter 8

Conclusions and Future Scope

8.1 Conclusions

A prototype of Micro Electro Mechanical Systems (MEMS) based Oxygen sensors for leak detection has been developed since MEMS offer a small, low cost, and low power platform that combined with appropriate metal-oxide sensing films.

CeO₂ thin films of different thicknesses ranging from 90 nm to 340 nm have been deposited at 400°C using RF magnetron sputtering on Al₂O₃ substrate. Characterization techniques such as Ellipsometry, XRD, XPS and AFM have been used to characterize the CeO₂ films for their thickness, structural, compositional/chemical and surface morphological properties. The CeO₂ film with an optimum thickness of 260 nm has shown very high sensitivity (12.6), fast response time (≤ 10 s) and recovery time (15 s) at a low operating temperature of 400°C, which are the best values reported till date in case of undoped CeO₂ thin film based sensors. The response time of CeO₂ based sensor may be reduced further by increasing the conductivity of the CeO₂ films with appropriate dopants.

Novel technique was used for the synthesis CeO₂-HfO₂ mixed oxide thin films using RF sputtering. The Hf atomic concentration was controlled using the size and number of HfO₂ pellets to achieve the best sensing performance. The fabricated/optimized CeO₂-HfO₂ mixed oxide sensor shows excellent sensitivity (~ 15), response time (8 s), and recovery time (10 s) at low operating temperatures $< 400^\circ\text{C}$ reported till today in the literature. This work has the potential to develop scalable oxygen sensors using mixed metal oxides.

Two different geometrical structures namely Perforated Type 1 and Type 2 Plat-

inum microheaters of dimension $500\mu\text{m} \times 500\mu\text{m}$ were designed and analyzed using FEM based software COMSOL. The simulated results show the temperature being distributed uniformly across the entire structure in both the designs. The designed microheaters were fabricated and characterized thermally and electrically by IR Camera and DC probe station respectively. The results showed excellent temperature uniformity throughout the entire heater area and the power consumed to obtain the temperature 400°C is nearly between 1.14 to 1.44 W which was considerably low than reported in the literature. This can be attributed to the novel design technique used by optimizing the area of the heater. The fabricated heaters were integrated into a gas sensor and the device was tested for oxygen gas sensing. The sensing results (response time of 13 seconds and recovery time of 20 seconds) were found to be in good agreement with the results obtained as discussed earlier.

The resistance changes of the gas sensing film due to the change in both the type and concentration of the gas analyte should be measured dynamically. For this purpose, a high efficient readout electronics has been designed.

8.2 Future Scope

This research work has explored and established the sensing behavior of MEMS based CeO_2 thin film based oxygen sensors for leak detection purpose. Use of HfO_2 with CeO_2 has enhanced the sensitivity. In order to improve the sensors performance, further research could be undertaken to improve the sensors performance by doping with other metal oxides such as TiO_2 , ZrO_2 , etc., By expanding the range (lower and higher) of oxygen concentration and operating temperature, a number of other areas of application can be explored.

A more detailed correlation between film porosity and its inherent characteristics such as grain size, crystallite size, grain boundaries and surface roughness and their dependence on processing parameters will throw more light on sensitivity control

Apart from gas sensor applications, microheaters with high temperature uniformity, low power and high thermal stability find a very wide application. So this part of the thesis results provide a motivation to do our future research in integrating the designed microheaters in applications like Shape memory alloy, Heater actuated cantilevers and BioMEMS applications where precise temperature is much a needed one for functioning.

The designed readout circuit can be validated by using “Off the Shelf” components. Similarly a circuit needs to be designed to monitor and maintain the temperature of the microheater. Both the readout circuit and the temperature control unit could be integrated into a single chip with CMOS foundry process which make the gas sensing unit completely integrated and portable. This strategy can also be further extended and deployed in wireless sensor networks.

Bibliography

- Aboud, A. A., H. Al-Kelesh, W. M. El Rouby, A. A. Farghali, A. Hamdein, and M. H. Khedr** (2018). CO₂ responses based on pure and doped CeO₂ nano-pellets. *Journal of materials research and technology*, **7**(1), 14–20.
- Aegerter, M. A., C. O. Avellaneda, A. Pawlicka, and M. Atik** (1997). Electrochromism in materials prepared by the sol-gel process. *Journal of Sol-Gel Science and Technology*, **8**(1-3), 689–696.
- Agashe, C., M. Takwale, B. Marathe, and V. Bhide** (1988). Structural properties of SnO₂: F films deposited by spray pyrolysis. *Solar Energy Materials*, **17**(2), 99–117.
- Aguiar, R., F. Sanchez, C. Ferrater, and M. Varela** (1997). Protective oxide coatings for superconducting YBa₂Cu₃O_{7-x} thin films. *Thin Solid Films*, **306**(1), 74–77.
- Akasaka, S., E. Boku, Y. Amamoto, H. Yuji, and I. Kanno** (2019). Ultrahigh temperature platinum microheater encapsulated by reduced-TiO₂ barrier layer. *Sensors and Actuators A: Physical*, **296**, 286–291.
- Ali, S. Z., F. Udrea, W. I. Milne, and J. W. Gardner** (2008). Tungsten-based SOI microhotplates for smart gas sensors. *Journal of Microelectromechanical Systems*, **17**(6), 1408–1417.
- Amaechi, J. and T. Godstime** (2015). Automotive exhausts emissions and its implications for environmental sustainability. *International of Advanced Academic Research-Engineering*, **1**(2), 1–11.
- AMS** (2020). URL <https://ams.com/products>.

- Anukunprasert, T., C. Saiwan, and E. Traversa** (2005). The development of gas sensor for carbon monoxide monitoring using nanostructure of Nb-TiO₂. *Science and Technology of Advanced Materials*, **6**(3-4), 359–363.
- Anwar, M., S. Kumar, F. Ahmed, N. Arshi, Y. J. Seo, C. G. Lee, and B. H. Koo** (2011). Study of nanocrystalline ceria thin films deposited by e-beam technique. *Current Applied Physics*, **11**(1), S301–S304.
- Arshak, K., G. Lyons, L. Cavanagh, and S. Clifford** (2003). Front-end signal conditioning used for resistance-based sensors in electronic nose systems: a review. *Sensor Review*.
- Aspnes, D., J. Theeten, and F. Hottier** (1979). Investigation of effective-medium models of microscopic surface roughness by spectroscopic ellipsometry. *Physical Review B*, **20**(8), 3292.
- Astie, S., A. Gue, E. Scheid, L. Lescouzeres, and A. Cassagnes** (1998). Optimization of an integrated SnO₂ gas sensor using a FEM simulator. *Sensors and Actuators A: Physical*, **69**(3), 205–211.
- Audebrand, N., J.-P. Auffrédic, and D. Louër** (2000). An X-ray powder diffraction study of the microstructure and growth kinetics of nanoscale crystallites obtained from hydrated cerium oxides. *Chemistry of materials*, **12**(6), 1791–1799.
- Barrett, C. S., B. CS, and M. TB** (1980). Structure of metals. Crystallographic methods, principles and data.
- Barrettino, D., M. Graf, W. H. Song, K.-U. Kirstein, A. Hierlemann, and H. Baltes** (2004). Hotplate-based monolithic CMOS microsystems for gas detection and material characterization for operating temperatures up to 500°C. *IEEE Journal of Solid-State Circuits*, **39**(7), 1202–1207.
- Bashar, S. A.** (1998). Study of indium tin oxide (ITO) for novel optoelectronic devices. *UMIST, Manchester*, 106–109.
- Bechtold, T., J. Hildenbrand, J. Wollenstein, and J. Korvink**, Model order reduction of 3D electro-thermal model for a novel micromachined hotplate gas sensor.

- In 5th International Conference on Thermal and Mechanical Simulation and Experiments in Microelectronics and Microsystems, 2004. EuroSimE 2004. Proceedings of the.* IEEE, 2004.
- Beie, H.-J.** and **A. Gnörich** (1991). Oxygen gas sensors based on CeO₂ thick and thin films. *Sensors and Actuators B: Chemical*, **4**(3-4), 393–399.
- Bene, R., I. Perczel, F. Reti, F. Meyer, M. Fleisher, and H. Meixner** (2000). Chemical reactions in the detection of acetone and NO by a CeO₂ thin film. *Sensors and Actuators B: Chemical*, **71**(1-2), 36–41.
- Bhatt, P.** and **A. G. Arora** (2014). *Design of Microheater for MEMS Based Gas Sensor*. Ph.D. thesis.
- Bhowmick, S., M. Iodice, M. Gioffre, G. Breglio, A. Irace, M. Riccio, G. Romano, S. Grilli, P. Ferraro, L. Mecozzi, et al.** (2017). Investigation of pyroelectric fields generated by lithium niobate crystals through integrated microheaters. *Sensors and Actuators A: Physical*, **261**, 140–150.
- Bielański, A., J. Dereń, and J. Haber** (1957). Electric conductivity and catalytic activity of semiconducting oxide catalysts. *Nature*, **179**(4561), 668–669.
- Biró, F., C. Dücső, Z. Hajnal, F. Riesz, A. E. Pap, and I. Bársony** (2014). Thermo-mechanical design and characterization of low dissipation micro-hotplates operated above 500°C. *Microelectronics Journal*, **45**(12), 1822–1828.
- Bonk, A., A. C. Maier, D. Burnat, U. F. Vogt, and A. Züttel**, Investigations on the Redox Performance of Pure and Doped CeO₂ by Comparing Solid State Reaction and Pechini Synthesis. *In Materials for Energy Infrastructure*. Springer, 2016, 11–20.
- Bosch Sensortec GmbH** (2020). URL <https://www.bosch-sensortec.com/products/environmental-sensors/>.
- Brailsford, A.** and **E. Logothetis** (1998). Selected aspects of gas sensing. *Sensors and Actuators B: Chemical*, **52**(1-2), 195–203.
- Brattain, W. H.** and **J. Bardeen** (1953). Surface properties of germanium. *The Bell System Technical Journal*, **32**(1), 1–41.

- Bruins, M., J. W. Gerritsen, W. W. van de Sande, A. van Belkum, and A. Bos** (2013). Enabling a transferable calibration model for metal-oxide type electronic noses. *Sensors and Actuators B: Chemical*, **188**, 1187–1195.
- Bumajdad, A., J. Eastoe, and A. Mathew** (2009). Cerium oxide nanoparticles prepared in self-assembled systems. *Advances in colloid and interface science*, **147**, 56–66.
- Burresti, A., A. Fort, S. Rocchi, M. S. Santos, N. Ulivieri, and V. Vignoli** (2005). Temperature profile investigation of SnO_2 sensors for CO detection enhancement. *IEEE transactions on instrumentation and measurement*, **54**(1), 79–86.
- CAMECA** (2017). Introduction to EPMA. URL <https://www.cameca.com/products/epma/technique>.
- Capone, S., A. Forleo, L. Francioso, R. Rella, P. Siciliano, J. Spadavecchia, D. Presicce, and A. M. Taurino** (2003). Solid state gas sensors: state of the art and future activities. *Journal of Optoelectronics and Advanced Materials*, **5**(5), 1335–1348.
- Capone, S., G. Leo, R. Rella, P. Siciliano, L. Vasanelli, M. Alvisi, L. Mirenghi, and A. Rizzo** (1998). Physical characterization of hafnium oxide thin films and their application as gas sensing devices. *Journal of Vacuum Science & Technology A: Vacuum, Surfaces, and Films*, **16**(6), 3564–3568.
- Capone, S. and P. Siciliano** (2004). Gas Sensors from Nanostructured Metal Oxides. *Encyclopedia of Nanoscience and Nanotechnology*, **3**(1), 769–804.
- Cardinali, G. C., L. Dori, M. Fiorini, I. Sayago, G. Faglia, C. Perego, G. Sberveglieri, F. Liberali, F. Maloberti, and D. Tonietto** (1997). A Smart Sensor System for Carbon Monoxide Detection. *Smart Sensor Interfaces*, **14**, 113–134.
- Castro, L., R. Suryanarayanan, A. Das, E. Bacca, M. Gomez, W. Lopera, P. Prieto, A. Kreisler, and J. Martin** (1995). Superconducting, surface and interface properties of Ho (123) and Bi (2212) films on sapphire with cerium oxide buffer layers. *Solid state communications*, **95**(12), 829–831.

- Chen, C.-Y.** and **K.-H. Chang** (2012). Temperature independent resistive oxygen sensor prepared using zirconia-doped ceria powders. *Sensors and Actuators B: Chemical*, **162**(1), 68–75.
- Chen, C.-Y., K.-H. Chang, H.-Y. Chiang,** and **S.-J. Shih** (2014). Preparation of a porous ceria coating for a resistive oxygen sensor. *Sensors and Actuators B: Chemical*, **204**, 31–41.
- Choi, H.-J., J. Moon, H.-B. Shim, K.-S. Han, E.-G. Lee,** and **K.-D. Jung** (2006). Preparation of nanocrystalline CeO₂ by the precipitation method and its improved methane oxidation activity. *Journal of the American Ceramic Society*, **89**(1), 343–345.
- Choi, J., Y. Mao,** and **J. Chang** (2011). Development of hafnium based high-k materials—A review. *Materials Science and Engineering: R: Reports*, **72**(6), 97–136.
- Chougule, M.,** Cerium oxide-based nanoparticles thin film: Sensitive and selective for detection of NO₂ gas. *In Proc. 17th Int. Meeting Chem. Sensors (IMCS)*. 2018.
- Cole, M., J. Gardner, A. Lim, P. Scivier,** and **J. Brignell** (1999). Polymeric resistive bridge gas sensor array driven by a standard cell CMOS current drive chip. *Sensors and Actuators B: Chemical*, **58**(1-3), 518–525.
- Comini, E., G. Faglia, G. Sberveglieri, Z. Pan,** and **Z. L. Wang** (2002). Stable and highly sensitive gas sensors based on semiconducting oxide nanobelts. *Applied Physics Letters*, **81**(10), 1869–1871.
- Creemer, J., D. Briand, H. Zandbergen, W. Van der Vlist, C. De Boer, N. F. de Rooij,** and **P. Sarro** (2008). Microhotplates with TiN heaters. *Sensors and Actuators A: Physical*, **148**(2), 416–421.
- Cullity, B. D.,** *Elements of X-ray Diffraction*. Addison-Wesley Publishing, 1956.
- Dahmen, K.-H.** and **M. Carris** (1997). MOCVD of HTS and GMR perovskites by aerosol and liquid delivery MOCVD. *Journal of alloys and compounds*, **251**(1-2), 270–277.

- Denhoff, M., B. Mason, H. Tran, and P. Grant** (1995). Afm study of CeO₂ growth on sapphire as a buffer layer for YBa₂Cu₃O₇. *MRS Online Proceedings Library Archive*, **401**.
- Dey, A.** (2018). Semiconductor metal oxide gas sensors: A review. *Materials Science and Engineering: B*, **229**, 206–217.
- Di Maggio, R., S. Rossi, L. Fedrizzi, and P. Scardi** (1997). ZrO₂-CeO₂ films as protective coatings against dry and wet corrosion of metallic alloys. *Surface and coatings technology*, **89**(3), 292–298.
- Draeger** (2020). URL https://www.draeger.com/en_in/Hospital/Productselector/Accessories-and-Consumables/Sensors.
- Durrani, S. and M. Al-Kuhaili** (2008). Effect of biasing voltages and electrode metals and materials on the sensitivity of electron beam evaporated HfO₂ thin film CO sensor. *Materials Chemistry and Physics*, **109**(1), 56–60.
- Durrani, S., M. Al-Kuhaili, and I. Bakhtiari** (2008). Carbon monoxide gas-sensing properties of electron-beam deposited cerium oxide thin films. *Sensors and Actuators B: Chemical*, **134**(2), 934–939.
- EESEMI** (2002). Comprehensive reference on semiconductor manufacturing. URL <https://eeseemi.com/evaporation.htm>.
- Elmi, I., S. Zampolli, E. Cozzani, M. Passini, G. Cardinali, and M. Severi**, Development of ultra low power consumption hotplates for gas sensing applications. *In SENSORS, 2006 IEEE*. IEEE, 2006.
- Eranna, G., B. Joshi, D. Runthala, and R. Gupta** (2004). Oxide materials for development of integrated gas sensors—a comprehensive review. *Critical Reviews in Solid State and Materials Sciences*, **29**(3-4), 111–188.
- Esch, H., G. Huyberechts, R. Mertens, G. Maes, J. Manca, W. De Ceuninck, and L. De Schepper** (2000). The stability of Pt heater and temperature sensing elements for silicon integrated tin oxide gas sensors. *Sensors and Actuators B: Chemical*, **65**(1-3), 190–192.

- Far, A., B. Guo, F. Flitti, and A. Bermak**, Temperature modulation for tin-oxide gas sensors. In *4th IEEE International Symposium on Electronic Design, Test and Applications (delta 2008)*. IEEE, 2008.
- Figaro** (2018). URL <https://www.figarosensor.com/product/sensor/>.
- Firebaugh, S. L., K. F. Jensen, and M. A. Schmidt** (1998). Investigation of high-temperature degradation of platinum thin films with an in situ resistance measurement apparatus. *Journal of Microelectromechanical systems*, **7**(1), 128–135.
- Fu, Q., A. Weber, and M. Flytzani-Stephanopoulos** (2001). Nanostructured Au–CeO₂ catalysts for low-temperature water–gas shift. *Catalysis Letters*, **77**(1-3), 87–95.
- Fukuda, H., M. Miura, S. Sakuma, and S. Nomura** (1998). Structural and electrical properties of crystalline CeO₂ films formed by metalorganic decomposition. *Japanese journal of applied physics*, **37**(7R), 4158.
- Ganapathi, K. L., N. Bhat, and S. Mohan** (2014). Influence of O₂ flow rate on HfO₂ gate dielectrics for back-gated graphene transistors. *Semiconductor Science and Technology*, **29**(5), 055007.
- Gardner, J., M. Vidic, P. Ingleby, A. Pike, J. Brignell, P. Scivier, P. Bartlett, A. Duke, and J. Elliott** (1998). Response of a poly (pyrrole) resistive micro-bridge to ethanol vapour. *Sensors and Actuators B: Chemical*, **48**(1-3), 289–295.
- Gerblinger, J., K. Hardtl, H. Meixner, and R. Aigner** (1995). High-temperature microsensors. *Sensors, A Comprehensive Survey*, **8**.
- Göpel, W.** (1991). Chemical Sensor Technologies: Empirical Art and Systematic Research. *Sensors: Chemical and Biochemical Sensors*, **2**, 61–118.
- Hassan, T. A.**, Development of nanosensors in nuclear technology. In *AIP Conference Proceedings*, volume 1799. AIP Publishing LLC, 2017.
- Heiland, G.** (1954). About the influence of adsorbed oxygen on the electrical conductivity of zinc oxide crystals. *Z. Phys.*, **138**, 459.
- Holgado, J. P., R. Alvarez, and G. Munuera** (2000). Study of CeO₂ XPS spectra by factor analysis: reduction of CeO₂. *Applied Surface Science*, **161**(3-4), 301–315.

- Hollmann, E., A. Zaitsev, V. Loginov, and Y. Likholetov** (1993). CeO₂ films deposited by DC reactive magnetron sputtering. *Journal of Physics D: Applied Physics*, **26**(3), 504.
- Hu, Z., X. Liu, D. Meng, Y. Guo, Y. Guo, and G. Lu** (2016). Effect of ceria crystal plane on the physicochemical and catalytic properties of Pd/ceria for CO and propane oxidation. *ACS Catalysis*, **6**(4), 2265–2279.
- Hwang, W.-J., K.-S. Shin, J.-H. Roh, D.-S. Lee, and S.-H. Choa** (2011). Development of micro-heaters with optimized temperature compensation design for gas sensors. *Sensors*, **11**(3), 2580–2591.
- Irene, E.** (1993). Applications of spectroscopic ellipsometry to microelectronics. *Thin Solid Films*, **233**(1-2), 96–111.
- Izu, N., T. Itoh, W. Shin, I. Matsubara, and N. Murayama** (2007). The effect of hafnia doping on the resistance of ceria for use in resistive oxygen sensors. *Sensors and Actuators B: Chemical*, **123**(1), 407–412.
- Izu, N., N. Murayama, W. Shin, I. Matsubara, and S. Kanzaki** (2004). Resistive oxygen sensors using cerium oxide thin films prepared by metal organic chemical vapor deposition and sputtering. *Japanese journal of applied physics*, **43**(10R), 6920.
- Izu, N., W. Shin, I. Matsubara, and N. Murayama** (2003a). The effects of the particle size and crystallite size on the response time for resistive oxygen gas sensor using cerium oxide thick film. *Sensors and Actuators B: Chemical*, **94**(2), 222–227.
- Izu, N., W. Shin, I. Matsubara, and N. Murayama** (2005a). Decrease in Resistance of Ceria Oxygen Sensor Induced by 10 mol% Hf and Zr Doping. *MRS Online Proceedings Library Archive*, **888**.
- Izu, N., W. Shin, I. Matsubara, and N. Murayama** (2005b). Resistive oxygen sensor using hafnium-doped cerium oxide. *Electrochemistry*, **73**(7), 478–480.
- Izu, N., W. Shin, and N. Murayama** (2002a). Numerical analysis of response time for resistive oxygen gas sensors. *Sensors and Actuators B: Chemical*, **87**(1), 99–104.

- Izu, N., W. Shin, and N. Murayama** (2003*b*). Fast response of resistive-type oxygen gas sensors based on nano-sized ceria powder. *Sensors and Actuators B: Chemical*, **93**(1-3), 449–453.
- Izu, N., W. Shin, N. Murayama, and S. Kanzaki** (2002*b*). Resistive oxygen gas sensors based on CeO₂ fine powder prepared using mist pyrolysis. *Sensors and Actuators B: Chemical*, **87**(1), 95–98.
- Jaiswal, N., K. Tanwar, R. Suman, D. Kumar, S. Upadhyay, and O. Parkash** (2019). A brief review on ceria based solid electrolytes for solid oxide fuel cells. *Journal of Alloys and Compounds*, **781**, 984–1005.
- Jasinski, P., T. Suzuki, and H. U. Anderson** (2003). Nanocrystalline undoped ceria oxygen sensor. *Sensors and Actuators B: Chemical*, **95**(1-3), 73–77.
- Je, J. and J. Lee** (2014). Design, fabrication, and characterization of liquid metal microheaters. *Journal of Microelectromechanical Systems*, **23**(5), 1156–1163.
- Ji, H., W. Zeng, and Y. Li** (2019). Gas sensing mechanisms of metal oxide semiconductors: a focus review. *Nanoscale*, **11**(47), 22664–22684.
- Joy, S. and J. K. Antony**, Design and simulation of a micro hotplate using COMSOL multiphysics for MEMS based gas sensor. In *2015 Fifth International Conference on Advances in Computing and Communications (ICACC)*. IEEE, 2015.
- Julissa, G.** (1994). An Overview of Magnetron Sputtering. URL <https://www.sputtertargets.net/blog/an-overview-of-magnetron-sputtering.html>.
- Jung, Y. S.** (2004). Spectroscopic ellipsometry studies on the optical constants of indium tin oxide films deposited under various sputtering conditions. *Thin Solid Films*, **467**(1-2), 36–42.
- Kašpar, J., P. Fornasiero, and M. Graziani** (1999). Use of CeO₂ based oxides in the three-way catalysis. *Catalysis Today*, **50**(2), 285–298.
- Kaushik, A., R. Kumar, R. D. Jayant, and M. Nair** (2015). Nanostructured gas sensors for health care: an overview. *Journal of personalized nanomedicine*, **1**(1), 10.

- Klug, H., L. Alexander, and X.-R. D. Procedures** (1962). John Wiley and Sons Inc. *New York*, 491.
- Kumar, H., K. Singh, N. Sood, A. Kumar, and R. Mittal**, Design and simulation of a Micro Hotplate for MEMS based integrated gas sensing system. *In 2014 IEEE Sensors Applications Symposium (SAS)*. IEEE, 2014.
- Kwak, S., Y.-S. Shim, Y. K. Yoo, J.-H. Lee, I. Kim, J. Kim, K. H. Lee, and J. H. Lee** (2018). MEMS-Based gas sensor using PdO-decorated TiO₂ thin film for highly sensitive and selective H₂ detection with low power consumption. *Electronic Materials Letters*, **14**(3), 305–313.
- Laconte, J., C. Dupont, D. Flandre, and J.-P. Raskin** (2004). SOI CMOS compatible low-power microheater optimization for the fabrication of smart gas sensors. *IEEE Sensors Journal*, **4**(5), 670–680.
- Lakshmi Ganapathi, K., N. Bhat, and S. Mohan** (2013). Optimization of HfO₂ films for high transconductance back gated graphene transistors. *Applied Physics Letters*, **103**(7), 073105.
- Lee, S., D. Dyer, and J. Gardner** (2003). Design and optimisation of a high-temperature silicon micro-hotplate for nanoporous palladium pellistors. *Microelectronics Journal*, **34**(2), 115–126.
- Leitenburg, C., A. Trovarelli, and J. Kašpar** (1997). A temperature-programmed and transient kinetic study of CO₂ Activation and methanation over CeO₂ Supported noble metals. *Journal of Catalysis*, **166**(1), 98–107.
- Leung, C. K. and D. M. Wilson**, Integrated interface circuits for chemiresistor arrays. *In 2005 IEEE International Symposium on Circuits and Systems*. IEEE, 2005.
- Li, T., L. Wu, Y. Liu, L. Wang, Y. Wang, and Y. Wang**, Micro-heater on membrane with large uniform-temperature area. *In SENSORS, 2006 IEEE*. IEEE, 2006.
- Li, T., L. Xu, and Y. Wang** (2017). Micro-heater-Based Gas Sensors. *Micro Electro Mechanical Systems. Micro/Nano Technologies*, **2**, 1–37.

- Li, Y., Q. Fu, and M. Flytzani-Stephanopoulos** (2000). Low-temperature water-gas shift reaction over Cu- and Ni- loaded cerium oxide catalysts. *Applied Catalysis B: Environmental*, **27**(3), 179–191.
- Li, Y., C. Vancura, D. Barrettino, M. Graf, C. Hagleitner, A. Kummer, M. Zimmermann, K.-U. Kirstein, and A. Hierlemann** (2007). Monolithic CMOS multi-transducer gas sensor microsystem for organic and inorganic analytes. *Sensors and Actuators B: Chemical*, **126**(2), 431–440.
- Lin, C., W. Xu, Q. Yao, and X. Wang**, Nanotechnology on Toxic Gas Detection and Treatment. *In Novel nanomaterials for biomedical, environmental and energy applications*. Elsevier, 2019a, 275–297.
- Lin, T., X. Lv, Z. Hu, A. Xu, and C. Feng** (2019b). Semiconductor metal oxides as chemoresistive sensors for detecting volatile organic compounds. *Sensors*, **19**(2), 233.
- Linde, G.** (2015). Comprehensive reference on semiconductor manufacturing. URL https://www.linde-gas.fr/en/safety_and_quality/gas_risks/inert_gases/index.html.
- Liu, H., L. Zhang, K. H. H. Li, and O. K. Tan** (2018). Microhotplates for metal oxide semiconductor gas sensor applications—towards the CMOS-MEMS monolithic approach. *Micromachines*, **9**(11), 557.
- Liu, W. and M. Flytzani-Stephanopoulos** (1996). Transition metal-promoted oxidation catalysis by fluorite oxides: A study of CO oxidation over Cu–CeO₂. *The Chemical Engineering Journal and the Biochemical Engineering Journal*, **64**(2), 283–294.
- Liu, Y., Y. Ding, L. Zhang, P.-X. Gao, and Y. Lei** (2012). CeO₂ nanofibers for in situ O₂ and CO sensing in harsh environments. *RSC Advances*, **2**(12), 5193–5198.
- Maeder, T., L. Sagalowicz, and P. Murali** (1998). Stabilized platinum electrodes for ferroelectric film deposition using Ti, Ta and Zr adhesion layers. *Japanese journal of applied physics*, **37**(4R), 2007.
- Majumder, D. and S. Roy** (2018). Development of low-ppm CO sensors using pristine CeO₂ nanospheres with high surface area. *ACS omega*, **3**(4), 4433–4440.

- Malcovati, P., H. Baltès, and F. Maloberti** (1996). Progress in microsensor interfaces. *Sensors Update*, **1**(1), 143–171.
- Malyukin, Y., V. Seminko, P. Maksimchuk, E. Okrushko, O. Sedyh, and Y. Zorenko** (2018). Hydrogen peroxide sensing using Ce^{3+} luminescence of cerium oxide (CeO_{2-x}) nanoparticles. *Optical Materials*, **85**, 303–307.
- Manorama, S. V., N. Izu, W. Shin, I. Matsubara, and N. Murayama** (2003). On the platinum sensitization of nanosized cerium dioxide oxygen sensors. *Sensors and Actuators B: Chemical*, **89**(3), 299–304.
- Martinelli, E., G. Pennazza, C. Falconi, A. D’Amico, and C. DI Nd Atale**, Comparison between two alternative feature extraction methods for chemical sensor array. In *Sensors And Microsystems*. World Scientific, 2004, 334–339.
- Masui, T., Y. Peng, K.-i. Machida, and G.-y. Adachi** (1998). Reduction Behavior of $\text{CeO}_2\text{-ZrO}_2$ Solid Solution Prepared from Cerium Zirconyl Oxalate. *Chemistry of materials*, **10**(12), 4005–4009.
- Mattox, D. M.**, *Handbook of physical vapor deposition (PVD) processing*. William Andrew, 2010.
- McGrath, M. J. and C. N. Scanaill**, Sensing and sensor fundamentals. In *Sensor Technologies*. Springer, 2013, 15–50.
- Mele, L., F. Santagata, E. Iervolino, M. Mihailovic, T. Rossi, A. Tran, H. Schellevis, J. Creemer, and P. Sarro** (2012). A molybdenum MEMS micro-hotplate for high-temperature operation. *Sensors and Actuators A: Physical*, **188**, 173–180.
- Messina, M., F. Franze, N. Speciale, E. Cozzani, and A. Roncaglia**, 3D simulation of conjugate heat transfer of ULP hotplates for a MOX gas sensing device. In *SENSORS, 2007 IEEE*. IEEE, 2007.
- Mihalache, V. and I. Pasuk** (2011). Grain growth, microstructure and surface modification of textured CeO_2 thin films on Ni substrate. *Acta materialia*, **59**(12), 4875–4885.

- Millot, F. and P. De Mierry** (1985). A new method for the study of chemical diffusion in oxides with application to cerium oxide CeO_{2-x} . *Journal of Physics and Chemistry of Solids*, **46**(7), 797–801.
- Moon, S., J.-W. Lee, N.-J. Choi, H.-K. Lee, W. Yang, J. Kim, and Y. Park** (2012). High-response and low-power-consumption CO micro gas sensor based on nano-powders and a micro-heater. *Journal of the Korean Physical Society*, **60**(2), 235–239.
- Morshed, A., S. Liu, R. Leonard, F. Mcintosh, N. El-Masry, and S. Bedair** (1997). Epitaxial CeO_2 on Silicon Substrates and the Potential of Si/ CeO_2 /Si for SOI Structures. *MRS Online Proceedings Library Archive*, **474**.
- Mullins, D. R., P. M. Albrecht, T.-L. Chen, F. C. Calaza, M. D. Biegalski, H. M. Christen, and S. H. Overbury** (2012). Water dissociation on CeO_2 (100) and CeO_2 (111) thin films. *The Journal of Physical Chemistry C*, **116**(36), 19419–19428.
- Nag, A., A. I. Zia, X. Li, S. C. Mukhopadhyay, and J. Kosel** (2015a). Novel sensing approach for LPG leakage detection: Part I—Operating mechanism and preliminary results. *IEEE Sensors Journal*, **16**(4), 996–1003.
- Nag, A., A. I. Zia, X. Li, S. C. Mukhopadhyay, and J. Kosel** (2015b). Novel sensing approach for LPG leakage detection—part II: effects of particle size, composition, and coating layer thickness. *IEEE Sensors Journal*, **16**(4), 1088–1094.
- Nandasiri, M., P. Nachimuthu, T. Varga, V. Shutthanandan, W. Jiang, S. V. Kuchibhatla, S. Thevuthasan, S. Seal, and A. Kayani** (2011). Influence of growth rate on the epitaxial orientation and crystalline quality of CeO_2 thin films grown on Al_2O_3 (0001). *Journal of Applied Physics*, **109**(1), 013525.
- Nazemi, H., A. Joseph, J. Park, and A. Emadi** (2019). Advanced micro-and nano-gas sensor technology: A review. *Sensors*, **19**(6), 1285.
- Netterfield, R. P., W. G. Sainty, P. J. Martin, and S. H. Sie** (1985). Properties of CeO_2 thin films prepared by oxygen-ion-assisted deposition. *Applied optics*, **24**(14), 2267–2272.

- Nissha FIS, Inc.** (2020). URL http://www.fisinc.co.jp/en/products/products_search.html?Cat=Cat1.
- Noor, M. M., G. Sugandi, M. F. Aziz, and B. Y. Majlis**, Effects of material and membrane structure on maximum temperature of microheater for gas sensor applications. In *2014 IEEE International Conference on Semiconductor Electronics (ICSE2014)*. IEEE, 2014.
- Oosthuizen, D., D. Motaung, and H. Swart** (2020). Gas sensors based on CeO₂ nanoparticles prepared by chemical precipitation method and their temperature-dependent selectivity towards H₂S and NO₂ gases. *Applied Surface Science*, **505**, 144356.
- Oxford Vacuum Science Ltd** (2000). URL http://www.oxford-vacuum.com/background/thin_film/sputtering.htm.
- Pan, M., G. Meng, H. Xin, C. Chen, D. Peng, and Y. Lin** (1998). Pure and doped CeO₂ thin films prepared by MOCVD process. *Thin Solid Films*, **324**(1-2), 89–93.
- Patil, D., N. Q. Dung, H. Jung, S. Y. Ahn, D. M. Jang, and D. Kim** (2012). Enzymatic glucose biosensor based on CeO₂ nanorods synthesized by non-isothermal precipitation. *Biosensors and Bioelectronics*, **31**(1), 176–181.
- Patil, P. S.** (1999). Versatility of chemical spray pyrolysis technique. *Materials Chemistry and physics*, **59**(3), 185–198.
- Pike, A. and J. W. Gardner** (1997). Thermal modelling and characterisation of micropower chemoresistive silicon sensors. *Sensors and Actuators B: Chemical*, **45**(1), 19–26.
- Qian, J., Y. Wang, J. Pan, Z. Chen, C. Wang, J. Chen, Z. Wu, et al.** (2020). Non-enzymatic glucose sensor based on ZnO–CeO₂ whiskers. *Materials Chemistry and Physics*, **239**, 122051.
- Qiao, J. and C. Y. Yang** (1995). High-T_c superconductors on buffered silicon: materials properties and device applications. *Materials Science and Engineering: R: Reports*, **14**(4), 157–201.

- Ramshanker, N., K. L. Ganapathi, M. Bhat, and S. Mohan** (2019). RF Sputtered CeO₂ Thin Films-Based Oxygen Sensors. *IEEE Sensors Journal*, **19**(22), 10821–10828.
- Reynolds, R.** (1989). Principles of powder diffraction. *Reviews in Mineralogy*, 20 pp., 1.
- Rudraswamy, S. B. and N. Bhat** (2016). Optimization of RF Sputtered Ag-Doped BaTiO₃-CuO Mixed Oxide Thin Film as Carbon Dioxide Sensor for Environmental Pollution Monitoring Application. *IEEE Sensors Journal*, **16**(13), 5145–5151.
- Scheffe, J. R., R. Jacot, G. R. Patzke, and A. Steinfeld** (2013). Synthesis, characterization, and thermochemical redox performance of Hf⁴⁺, Zr⁴⁺, and Sc³⁺ doped ceria for splitting CO₂. *The Journal of Physical Chemistry C*, **117**(46), 24104–24114.
- Science Education Resource Center, C. C.** (2019). Geochemical Instrumentation and Analysis. URL https://serc.carleton.edu/research_education/geochemsheets/techniques/EPMA.html.
- Seiyama, T., A. Kato, K. Fujiishi, and M. Nagatani** (1962). A new detector for gaseous components using semiconductive thin films. *Analytical Chemistry*, **34**(11), 1502–1503.
- Sensirion** (2020). URL <https://www.sensirion.com/en/environmental-sensors/gas-sensors/>.
- Sergent, N., J.-F. Lamonier, and A. Aboukaïs** (2000). Electron Paramagnetic Resonance in Combination with the Thermal Analysis, X-ray Diffraction, and Raman Spectroscopy to Follow the Structural Properties of Zr_xCe_{1-x}O₂ Solid Systems and Precursors. *Chemistry of materials*, **12**(12), 3830–3835.
- Shin, W., N. Izu, I. Matsubara, and N. Murayama** (2004). Millisecond-order response measurement for fast oxygen gas sensors. *Sensors and Actuators B: Chemical*, **100**(3), 395–400.
- Shurmer, H. V. and J. W. Gardner** (1992). Odour discrimination with an electronic nose. *Sensors and Actuators B: Chemical*, **8**(1), 1–11.

- Singh, I.** and **S. Mohan**, 3D Simulations and electro-thermal analysis of micro-hotplate designs using Coventorware for gas sensor applications. *In Int Conference on smart materials structure and systems, Bangalore, India.* 2005.
- Singh, P.** and **K. Srivatsa** (2016). On the wettability and optical properties of nanocrystalline CeO₂ thin films.
- Solanki, P. R., C. Dhand, A. Kaushik, A. A. Ansari, K. Sood, and B. Malhotra** (2009). Nanostructured cerium oxide film for triglyceride sensor. *Sensors and Actuators B: Chemical*, **141**(2), 551–556.
- Spannhake, J., O. Schulz, A. Helwig, A. Krenkow, G. Müller, and T. Doll** (2006). High-temperature MEMS heater platforms: long-term performance of metal and semiconductor heater materials. *Sensors*, **6**(4), 405–419.
- Stuart, R. V.** (1983). Vacuum Technology, Thin Films, and Sputtering; An Introduction. **39**(5), 123–131.
- Suchea, M., N. Katsarakis, S. Christoulakis, S. Nikolopoulou, and G. Kiriakidis** (2006). Low temperature indium oxide gas sensors. *Sensors and Actuators B: Chemical*, **118**(1-2), 135–141.
- Sudarsanam, P., P. Selvakannan, S. K. Soni, S. K. Bhargava, and B. M. Reddy** (2014). Structural evaluation and catalytic performance of nano-Au supported on nanocrystalline Ce_{0.9}Fe_{0.1}O_{2-δ} solid solution for oxidation of carbon monoxide and benzylamine. *Rsc Advances*, **4**(82), 43460–43469.
- Sujatha, L., V. S. S. Aravind, R. Padamapriya, and B. Preethi**, Design and Analysis of Micro-Heaters using COMSOL Multiphysics For MEMS Based Gas Sensor. *In Excerpt from the Proceedings of the 2012 COMSOL Conference in Bangalore.* 2012.
- Ta, M.-T., D. Briand, Y. Guhel, J. Bernard, J. Pesant, and B. Boudart** (2008). Growth and structural characterization of cerium oxide thin films realized on Si (111) substrates by on-axis rf magnetron sputtering. *Thin Solid Films*, **517**(1), 450–452.
- Tomar, M.** and **F. Garcia** (1981). Spray pyrolysis in solar cells and gas sensors. *Progress in Crystal Growth and Characterization*, **4**(3), 221–248.

- Tompkins, H.** (2006). WVASE32® Software Training Manual, JA Woollam Co. Inc., Lincoln, NE, USA, 210.
- Trinchi, A., Y. Li, W. Wlodarski, S. Kaciulis, L. Pandolfi, S. Viticoli, E. Comini, and G. Sberveglieri** (2003). Investigation of sol-gel prepared CeO₂-TiO₂ thin films for oxygen gas sensing. *Sensors and Actuators B: Chemical*, **95**(1-3), 145–150.
- Trovarelli, A.** and **P. Fornasiero**, *Catalysis by ceria and related materials*, volume 12. World Scientific, 2013.
- Tye, L., N. El-Masry, T. Chikyow, P. McLarty, and S. Bedair** (1994). Electrical characteristics of epitaxial CeO₂ on Si (111). *Applied physics letters*, **65**(24), 3081–3083.
- Udrea, F., J. Gardner, D. Setiadi, J. Covington, T. Dogaru, C. Lu, and W. Milne** (2001). Design and simulations of SOI CMOS micro-hotplate gas sensors. *Sensors and Actuators B: Chemical*, **78**(1-3), 180–190.
- Ujjain, S. K., A. Das, G. Srivastava, P. Ahuja, M. Roy, A. Arya, K. Bhargava, N. Sethy, S. K. Singh, R. K. Sharma, et al.** (2014). Nanoceria based electrochemical sensor for hydrogen peroxide detection. *Biointerphases*, **9**(3), 031011.
- Varghese, S. S., S. H. Varghese, S. Swaminathan, K. K. Singh, and V. Mittal** (2015). Two-dimensional materials for sensing: graphene and beyond. *Electronics*, **4**(3), 651–687.
- Velmathi, G.** (2015). *Integrated Gas Sensor-Studies On Sensing Film Deposition, Microheater Design And Fabrication, Interface Electronics Design And Testing*. Ph.D. thesis.
- Velmathi, G.** (2017). Design of Microheaters with better thermal management for sensor applications. *International Journal of Mechanical Engineering and Technology*, **8**(10), 823–828.
- Velmathi, G., N. Ramshanker, and S. Mohan**, 2D Simulations and Electro-Thermal Analysis of Micro-Heater Designs Using COMSOLTM for Gas Sensor Applications. In *COMSOL Conference I*. 2010.

- Venkatesh, M., B. El Mansouri, J. Wei, A. Bossche, and G. Zhang**, Electro-thermal analysis and design of a combined MEMS impedance and micro hotplate device for gas sensing applications. *In 2016 17th International Conference on Thermal, Mechanical and Multi-Physics Simulation and Experiments in Microelectronics and Microsystems (EuroSimE)*. IEEE, 2016.
- Vossen, J. L. and J. Cuomo**, Glow discharge sputter deposition. *In Thin film processes*. Elsevier, 1978, 11–73.
- Wang, W., B. Zhang, S. Jiang, H. Bai, and S. Zhang** (2019). Use of CeO₂ nanoparticles to enhance UV-shielding of transparent regenerated cellulose films. *Polymers*, **11**(3), 458.
- Wang, Y., F. Wei, S. Yue, Z. Yang, and J. Du** (2008). Epitaxial growth of HfO₂ doped CeO₂ thin films on Si (001) substrates for high- κ application. *Applied Physics Letters*, **92**(1), 012915.
- Warren, B.** (1990). X-Ray Diffraction, Dover Publications, Inc., New York.
- Watts, J. F. and J. Wolstenholme** (2003). An introduction to surface analysis by XPS and AES.
- Wiesendanger, R. and W. Roland**, *Scanning probe microscopy and spectroscopy: methods and applications*. Cambridge university press, 1994.
- Woollam, J., B. Johs, C. Herzinger, J. Hilfiker, R. Synowicki, and C. Bungay** (1999). Critical Reviews of Optical Science and Technology.
- Yabe, S. and T. Sato** (2003). Cerium oxide for sunscreen cosmetics. *Journal of Solid State Chemistry*, **171**(1-2), 7–11.
- Yoon, D. S., Y.-S. Lee, Y. Lee, H. J. Cho, S. W. Sung, K. W. Oh, J. Cha, and G. Lim** (2002). Precise temperature control and rapid thermal cycling in a micromachined DNA polymerase chain reaction chip. *Journal of Micromechanics and Microengineering*, **12**(6), 813.
- Younis, A., D. Chu, Y. V. Kaneti, and S. Li** (2016). Tuning the surface oxygen concentration of {111} surrounded ceria nanocrystals for enhanced photocatalytic activities. *Nanoscale*, **8**(1), 378–387.

- Yuan, W.** and **G. Shi** (2013). Graphene-based gas sensors. *Journal of Materials Chemistry A*, **1**(35), 10078–10091.
- Zhang, Y., S. Andersson,** and **M. Muhammed** (1995). Nanophase catalytic oxides: I. Synthesis of doped cerium oxides as oxygen storage promoters. *Applied Catalysis B: Environmental*, **6**(4), 325–337.
- Zhang, Y., Y. Yu,** and **H. He** (2016). Oxygen vacancies on nanosized ceria govern the NO_x storage capacity of NSR catalysts. *Catalysis Science & Technology*, **6**(11), 3950–3962.
- Zhao, X., Y. Du, W. Ye, D. Lu, X. Xia,** and **C. Wang** (2013). Sensitive determination of thymol based on CeO_2 nanoparticle–decorated graphene hybrid film. *New Journal of Chemistry*, **37**(12), 4045–4051.
- Zhu, Y., N. Jain, M. K. Hudait, D. Maurya, R. Varghese,** and **S. Priya** (2014). X-ray photoelectron spectroscopy analysis and band offset determination of CeO_2 deposited on epitaxial (100),(110), and (111) Ge. *Journal of Vacuum Science & Technology B, Nanotechnology and Microelectronics: Materials, Processing, Measurement, and Phenomena*, **32**(1), 011217.

Publications based on the thesis

Refereed International Journals

1. N. Ramshanker, Kolla Lakshmi Ganapathi, M. S. Bhat, S. Mohan (2019), "RF Sputtered CeO₂ Thin Films-Based Oxygen Sensors", *IEEE Sensors Journal*, Vol.19, No.22, pp 10821-10828.
2. N. Ramshanker, Kolla Lakshmi Ganapathi, N. Varun, M. S. Bhat, S. Mohan, "Development of CeO₂-HfO₂ mixed oxide thin films for high performance oxygen sensors", (Submitted to IEEE Sensors Journal).
3. N. Ramshanker, Kolla Lakshmi Ganapathi, M. S. Bhat, S. Mohan, "Design and Development of Microheaters with High Temperature Uniformity for Gas Sensors", (Manuscript under preparation).

Contributing Chapter

1. N. Ramshanker, Kolla Lakshmi Ganapathi, M. S. Bhat, S. Mohan (2020), "Fabrication and Characterization of CeO₂ thin-film based oxygen sensors", *Printed and Flexible Sensor Technology*, (Submitted to IOP Publishing, UK.)

International Conference Proceedings:

1. N. Ramshanker, M. S. Bhat and S. Mohan, "Deposition and Characterization of CeO₂ films by RF Sputtering Technique for Oxygen Sensing Applications", International Conference of Young Researchers on Advanced Materials (IUMRS-ICYRAM 2016), December 11-15, 2016.
2. N. Ramshanker, Kolla Lakshmi Ganapathi, M. S. Bhat and S. Mohan, "RF Sputtered CeO₂ films for Oxygen Sensing", Eighth ISSS International Conference on Smart Materials, Structures & Systems (ISSS 2017), July 05-07, 2017.

3. N. Ramshanker, Kolla Lakshmi Ganapathi, M. S. Bhat and S. Mohan, “Development of Titanium Doped Cerium Oxide Thin films for Oxygen Sensors”, Bangalore Nano 2017, December 07-08, 2017.
4. N. Ramshanker, Kolla Lakshmi Ganapathi, N. Varun, M. S. Bhat and S. Mohan, “Performance Enhancement of CeO₂ Thin Film Based Oxygen Sensors via TiO₂ Doping”, 5th International Conference on Emerging Electronics (IEEE-ICEE 2020), November 26-28, 2020.
5. N. Ramshanker, Kolla Lakshmi Ganapathi, M. S. Bhat and S. Mohan, “Development of a thin film based oxygen sensor for defence applications”, National Symposium on Instrumentation (NSI-42), December 28-29, 2020 (***Best Paper Award***).

Student Details

Name : RAMSHANKER N
Date of Birth : 13-08-1977
Address : No. 7/7, 7th Cross, I Main,
GovindarajNagar, Bangalore - 560 040
Contact : +91 9845403352
Email : ramshanker.kavi@gmail.com
Qualification : Bachelor of Engineering (2008)
Electrical & Electronics Engineering
B.M.S College of Engineering, Bangalore
Visvesvaraya Technological University

: Master of Technology (M.Tech) (2012)
VLSI Design and Embedded Systems
UTL Technologies Ltd, Bangalore
Visvesvaraya Technological University

: Doctor of Philosophy (Ph.D.) (2020)
National Institute of Technology Karnataka (NITK)
Surathkal, Mangalore, Karnataka